NUMERICAL MODELING OF LOCALIZED DAMAGE IN PLAIN AND REINFORCED CONCRETE STRUCTURES

By Sina Moallemi, B.Eng., M.Sc.

A Thesis Submitted to the School of Graduate Studies in Partial Fulfilment of the Requirement for the Degree Doctor of Philosophy in Civil Engineering

McMaster University DOCTOR OF PHILOSOPHY (2017) Hamilton, Ontario (Civil Engineering)

TITLE: Numerical Modeling of Localized Damage in Plain and Reinforced Concrete Structures AUTHOR: Sina Moallemi, B. Eng., M.Sc. (Sharif University of Technology) SUPERVISOR: Professor S. Pietruszczak NUMBER OF PAGES: xii, 119.

Abstract

The primary objective of this research is to develop and verify a methodology for modeling three-dimensional discrete crack growth in concrete and reinforced concrete structures. Two main sources of damage, considered in this work, include the mechanical loading and the chemical interaction. The behavior of concrete is brittle in tension and becomes ductile behavior under compressive loading. At the same time, the chemical interaction triggers a progressive degradation of strength parameters. The main focus in this research is on numerical analysis of localized damage that is associated with formation of macrocracks. The specific form of chemical interaction examined here involves the alkali-silica reaction (ASR).

The approach used in this work for describing the propagation of macrocraks is based on the volume averaging technique. This scheme represents a simplified form of strong discontinuity approach (SDA). It incorporates the notion of a '*characteristic length*', which is defined as the ratio of area of the crack surface to the considered referential volume. It is demonstrated, based on an extensive numerical study, that this approach gives mesh-independent results which are consistent with the experimental evidence. The accuracy of the solutions is virtually the same as that based on SDA and/or the Extended Finite Element Method (XFEM), while the computational effort is significantly smaller. In order to describe the behavior of the fractured zone, a traction-velocity discontinuity relation is formulated that is representative of different modes of damage propagation, including crack opening in tensile regime as well as shear band formation under compression. For tracing the discontinuity within domain, *crack smoothening algorithm* is employed to overcome any numerical instabilities that may occur close to ultimate load of the structure.

The general methodology, as outlined above, has been enhanced by incorporating the chemo-plasticity framework to describe the damage propagation in concrete affected by chemical interaction, i.e. continuing ASR. The latter is associated with progressive expansion of the silica gel that is coupled with degradation of strength properties. An implicit scheme has been developed,

incorporating the return mapping algorithm, for the integration of the governing constitutive relations. The framework has been implemented in Abaqus software to examine the crack propagation pattern in structural elements subjected to continuing ASR.

Another major topic addressed in this thesis is the '*size effect*' phenomenon. The existing experimental studies, conducted primarily on various concrete structures, clearly show that the ultimate strength is strongly affected by the size of the structure. This phenomenon stems primarily from the effect of localized damage that accompanies the structural failure. The quantitative response depends on the geometry of the structure, type of loading and the material properties. The size effect has been investigated here for a number of notched and un-notched concrete beams, of different geometries, subjected to three-point bending. Both mechanical loading and the chemical interaction have been considered.

The next topic considered in this study deals with analysis of localized fracture in 3D reinforced concrete structures. Here, a mesoscale approach is employed whereby the material is perceived as a composite medium comprising two constituents, i.e. concrete matrix and steel reinforcement. The response at the macroscale is obtained via a homogenization procedure that incorporates again the volume averaging. The latter incorporates a set of static and kinematic constraints that are representative of the response prior to the onset of fracture. After the formation of macrocracks, a traction-separation law within the fractured zone is modified by incorporating the Timoshenko beam theory in order to assess the stiffness characteristics in the presence of reinforcement. A number of numerical examples are given that examine the crack pattern formation and the associated fracture mechanism in concrete beams at different intensity of reinforcement.

The final chapter of this thesis provides an illustrative example of the application of the proposed methodology to the analysis of a large scale structure. The focus here is on the assessment of structural damage in a hydraulic structure subjected to ASR continuing over of period of a few decades. The results, in term of the predicted extent of damage as well as the displacement history at some specific locations, are compared with in-situ monitoring.

Acknowledgements

Firstly, I would like to express my sincere gratitude to my advisor Prof. Pietruszczak for the continuous support of my PhD study and my carrier, for his patience, motivation, and immense knowledge. His priceless guidance helped me a lot at every stage of the research and writing of this thesis. I could not have imagined having a better advisor and mentor in my life.

Besides my advisor, I would like to thank the members of my supervisory committee: Prof. Chidiac and Prof. Konstantinidis, not only for their insightful comments and encouragement, but also for suggestions to widen my research from various perspectives.

My sincere thanks also goes my old friends Ehsan and Alireza, for their tremendous help in my graduate study and my life in Canada. I also want to thank my officemates (Ehsan, Aida, Ashkan, Marco, Jingshan, William, Yuaqin and Xing) for discussions, for the sleepless nights we were working together and for all the fun we have had in the last four years.

Co-Authorship:

Based on the regulation of "Sandwich" thesis, details of cooperation between authors for each paper are presented here.

Chapters 2 and 4:

S. Moallemi has extended the embedded discontinuity approach to modeling of 3D crack propagation in concrete structures affected by ASR (Chapter 2). A similar methodology was then employed to describe the mechanical behavior of reinforced concrete (Chapter 4). At all stages of work, the key aspects of the formulation were discussed with Dr. Pietruszczak. S. Moallemi has also developed and implemented a crack smoothening algorithm which increases the accuracy of the predicted crack trajectories. The framework was then incorporated by him in an FEM code and a series of numerical examples, suggested by Dr. Pietruszczak, were solved. Both chapters were drafted by S. Moallemi and revised and finalized by Dr. Pietruszczak.

Chapter 3:

The main topic, i.e. the implementation of volume averaging technique to examine the size-effect in concrete structures under a broad range of loading conditions, was suggested by Dr. Mroz. The details of the formulation have been developed jointly by all co-authors. The numerical implementation of the framework in the FEM code, as well as all numerical simulations, were conducted by S. Moallemi. A draft of this chapter was prepared by the student, revised by Dr. Pietruszczak and Dr. Mroz and finalized by Dr. Pietruszczak.

Table of contents

List of Figures

List of Tables

1 Introduction

In this chapter, a summary of research and a brief review of the employed methodologies are presented. As implied by the topic of this thesis, the main focus in this work is on numerical modeling of crack growth in three-dimensional concrete structures. This thesis is presented in article-based format which includes three journal papers in separate chapters as the main contributions in this study. The list of publications is as follows:

1. S. Moallemi, S. Pietruszczak, *Numerical analysis of propagation of macrocracks in 3D concrete structures affected by ASR*. ACI Materials Journal (2016); submitted.

2. S. Moallemi, S. Pietruszczak, Z. Mróz, Z, *Deterministic size effect in concrete structures with account for chemo-mechanical loading*. Computers and Structures (2017); **182**: 74-86.

3. S. Moallemi, S. Pietruszczak, *Analysis of localized fracture in 3D reinforced concrete structures using volume averaging technique*. Finite Element in Analysis and Design (2017); **125**: 41-52.

At the beginning of each chapter, an additional page related to the main contribution in that work is also provided. In addition to the aforementioned journal articles, a brief description of an industrially-oriented work that deals with the topic of 'Numerical modeling of damage propagation in a large scale structure' is given in the last chapter of this thesis.

In what follows, the motivation and goals of the thesis are outlined first. Subsequently, a brief history of different methodologies for modeling discontinuities in solids is provided. At the end of

the chapter, the techniques for modeling the crack growth, as well as accounting for the presence of reinforcements, are briefly discussed.

1.1 Motivation

One of the most important issues in the context of design of concrete structures is an understanding of the process of formation and propagation of damage. The experimental evidence indicates that concrete, as a material, shows a brittle response in the tension regime and becomes ductile under compression, with strength progressively increasing with the increase in confining pressure. Over the last few decades, various constitutive models, based on different mathematical frameworks that include damage and/or fracture mechanics, plasticity, etc., have been proposed to describe the response of concrete (cf. [1-3]).

The numerical analysis of actual boundary-value problems involving concrete structures is typically conducted within the framework of Finite Element Method (FEM) [4-5]. For modeling of fracture in concrete several studies have been conducted dealing with the onset of crack propagation in tensile region [6-7] and the evolution of damage in compression domain [8-9].

There are several conceptual difficulties, however, in terms of an adequate analysis associated with strain localization. In particular, the problem involves an unstable (strain-softening) response that cannot be strictly perceived as a material property and a continuum framework should incorporate the notion of a ‘characteristic dimension’ which has a clear quantitative definition. The importance of development of a reliable methodology for simulation of damage propagation is quite evident in case of large scale structures such as bridges, power plants and dams, where the failure can affect both the human lives and the environment.

The damage in concrete structures can be triggered not only by mechanical load, but also through the degradation of properties resulting from continuing alkali silica reaction (ASR). The reaction involves aggregate and cement and leads to formation of an expansive silica. The process can be influenced by the humidity and the type of aggregate [10]. According to experimental evidence,

the silica gel expands by absorbing water, which leads the expansion of concrete mass. The latter induces damage in its microstructure [11] and leads to a significant reduction of concrete strength. The kinetics of the reaction depends on time, which needs to be considered in the mathematical framework. Therefore, the classical plasticity approach, which is rate independent, cannot be employed here. The first general continuum approach, involving the framework of chemo-plasticity, was developed in ref. [12]. Later, several derivative concepts were proposed that included both the macroscale models as well as micromechanical descriptions of ASR-induced deformation (cf.[13-14]). The formulation employed here follows the earlier approach (i.e. that reported by Pietruszczak [12]), which is enhanced by incorporating the framework for discrete modeling of 3D crack propagation.

In what follows, a brief review of different methodologies for describing the process of crack growth in geomaterials is provided first, followed by an outline of the scope of research conducted in this thesis.

1.2 Background

The damage growth in concrete structures has been studied for a number of decades now. The FEM-based simulations of fracture date back to 1960's. In the early approaches, the discontinuities were taken into account by incorporating node separation along the crack path [15]. In this scheme the cracks were assumed to form along the edges of the elements, which resulted in mesh-dependency of the solution. In order to address this problem, an enhanced approach was developed that incorporated a mesh adaptivity [7,8]. In analogy to the original approach, the crack was assumed to form along the edge of each element, however the geometry of the FE mesh was continuously adapted during the simulation to trace the crack growth in a more realistic way. Although the obtained results were reasonably accurate, the computational effort associated with this methodology was very high, as it involved multiple nodal data transformation due to updating

the mesh and repeated discretization of the domain. This, motivated researchers to develop alternative methodologies for crack propagation.

In the mid of 1980's and 1990's a smeared shear-band approach was introduced. The concept was first developed within the context of an averaging scheme for a constitutive relation involving a localized deformation mode (Pietruszczak and Mroz [16]). Later, this approach was employed within the FEM discretization by introducing the discontinuity as a band-width crack in the element. It was assumed that the displacement varies linearly within the band, however the displacement gradient remains discontinuous [17-18]. This scheme was later modified [19] by incorporating the Heaviside step function to model a strong discontinuity, whereby the displacement field in the elementary volume remains discontinuous. The strong discontinuity approach (SDA) has been widely used, within the plasticity framework, for modeling progressive damage and formation of shear band [20,21]. Note that in the context of FEM, the implementation of SDA requires an additional degree of freedom to describe discontinuity jump across the cracked element, which allows to simulate crack growth without any re-meshing.

In late 1990's Belytschko and co-workers modified the strong discontinuity approach by developing the so-called Extended Finite Element Method (XFEM). In this scheme, the discontinuity is modeled by modifying the shape functions and adding additional degrees of freedom based on the concept of portion of unity [22]. Depending on the type of discontinuity, the additional shape functions can be modified to capture both week and strong discontinuity within the domain [23,24]. Note that the weak discontinuity refers to the continuous displacement field and a discontinuity in its gradient over the fractured zone. One of the main issues in XFEM is the need for modifying the standard finite element integration. In the revised scheme, the cracked element should be subdivided into smaller domains (sub-triangles) to provide Gauss points on both sides of the discontinuity, otherwise the predicted jump along the fractured zone would not be reliable.

Even though the use of XFEM is associated with a high computational cost, this approach has been used in numerous applications in solid mechanics as well as in multi-phase materials. In early works, Belytschko and Black [23], and later Moës et.al [24], modeled the traction-free crack

growth in solids. They incorporated additional degrees of freedom for the crack tip elements in order to define the stress intensity factors employed in determining the direction of crack propagation. The application to cohesive crack growth was first introduced by Wells and Sluys [25]. In their work, an exponential function was used to relate the traction along discontinuity to the crack opening. This scheme has been later enhanced by Moës and Belytschko [26] by enriching the nodes at the crack-tip to provide a more realistic prediction of stress field around the tip. XFEM framework has also been used in modeling frictional contacts to avoid the penetration of crack surfaces [27]. Other significant applications involve modeling of the multiple crack growth as well as intersecting cracks. Daux et al. [28] modified the enrichment and enhanced shaped functions based on the superposition concept to capture the branching cracks. Later, Deb and Das [29] used this concept in simulation of intersecting faults in jointed rock mass. The XFEM methodology has also been employed to model discontinuities in two phase materials. Réthoré et al. [30] incorporated the mass balance equation to simulate the fluid flow in the stationary cracks in fully saturated domain. In the simulation, the fluid flow has been considered as a weak discontinuity whereby the water pressure is identical on both sides of the crack, however the leak-off remains discontinuous. This approach was later extended to progressive crack propagation in semi and fully saturated porous media for modeling of hydraulic fracturing [31].

Although the use of XFEM is widely accepted among the researchers, the methodology itself is not efficient for simulating practical engineering problems that involve large-scale structures. This stems from the need to employ additional degrees of freedom for cracked elements as well as special integration techniques. In order to overcome this limitation, the current research incorporates the standard FEM methodology combined with the *volume averaging technique* for the description of fractured zone. As mentioned before, in early 1980's Pietruszczak and Mróz [16] developed a homogenization procedure in which the strain softening response was described by incorporating an inhomogeneous deformation mode associated with localization into a shear band. In this approach, the material within the shear band was assumed to undergo plastic deformation, while the intact material, in the region adjacent to the interface, was considered to experience unloading (i.e. elastic behavior). The macroscopic deformation was then evaluated as

volumetric average of contribution from both constituents. This approach has subsequently been extended and applied in the context of analysis of various geotechnical problems, including the response of water infiltrated soils [32, 33]. The FE analysis incorporated this approach in a 'smeared' sense. The solution was computationally efficient and mesh-independent; however, it often suffered from the loss of convergence when the ultimate load for the structure was attained. In order to resolve this issue, Haghighat and Pietruszczak [34] have recently reformulated the problem by incorporating a discrete monitoring of the crack trajectory using the level-set method. In the present work, the latter technique has been extended to three-dimensional analysis of plain/reinforced concrete structures. The proposed modification makes the volume averaging technique an attractive candidate to replace XFEM, as the computational effort associated with this methodology is significantly reduced in view of the use of standard shape functions and the standard numerical integration scheme.

An important issue which is associated with the description of damage is that of specifying a criterion for the onset of localization. The most commonly used technique for the initiation of localized deformation in compressive regime is the bifurcation analysis [35]. In tensile zone, several different approaches have been employed that can be categorized as local and global algorithms [36]. The primary methodologies used in quasi brittle materials include the averaged stress criterion, linear elastic fracture mechanics, global tracking algorithm and minimum of total energy. The first two, represent local algorithms and the last two are categorized as the global schemes. A comparison of these methods can be found in ref [36]. The simplest local scheme which is commonly employed is the criterion stipulating that the onset of cracking occurs when the maximum principal stress reaches the critical value, i.e. the tensile strength of the material [23-25].

The use of local algorithms for predicting the crack orientation can lead to significant errors in cases when the ultimate load of the structure is approached. In order to remedy the problem, the crack smoothening procedure has been developed, whereby the normal direction of the crack could be modified based on the orientation of crack surfaces in the adjacent elements. This scheme has been explained in details in ref [37] and it is implemented in this research.

1.3 General scope

In this section a brief overview of the material covered in each chapter is provided. As mentioned earlier, the individual chapters of this thesis are associated with journal articles that address the main research topics.

In the chapter 2, the mathematical formulation for modeling localized damage in concrete structures suffering from continuing ASR is provided. The approach incorporates the framework of chemo-elasticity. The kinetics of the reaction is briefly discussed and an enhanced implicit integration scheme is developed. The formulation is completed by employing a cohesive law that describes the traction-separation behavior in the fractured zone for both loading and unloading conditions. In this work the crack is assumed to initiate when the Rankine's criterion is satisfied, while its direction is normal to that of the maximum principal stress. During the propagation process, when the external load approaches its ultimate value, the crack orientation is modified based on the 3D crack smoothening algorithm. The framework has been verified by a series of numerical examples dealing with plain and reinforced concrete structures subjected to various loading configurations, including both mechanical load and the chemical interaction. The results have been compared with the available experimental data.

In chapter 3, the previous formulation is enhanced by considering the elasto-plastic behavior of concrete and developing an implicit scheme within the chemo-plasticity framework. A complete set of governing constitutive relations is derived for both stress and strain-controlled conditions. The structure of these relations is such that they employ a superposition of two terms, the first representing an instantaneous mechanical response, which is rate-independent, and the second related to time-dependent effects of chemical interaction. The constitutive model for concrete is based on the work by Pietruszczak et.al. [2], whereby the evolution of yield/loading surface depends on accumulated plastic distortion. The crack growth strategy in tensile zone is assumed to be similar to that outlined in chapter 2. In the compressive regime, however, the bifurcation analysis is employed to determine the direction of macrocrack. It is shown that the inception of

strain localization due to ASR alone is possible with its rate controlled by the kinetics of chemical reaction. On the other hand, the instantaneous mode occurs when the bifurcation condition, associated with singularity of the acoustic tensor, is satisfied. A general FE formulation has been outlined, governing the chemo-mechanical process, and an implicit backward Euler integration scheme has been developed.

The presented methodology has been used to investigate the size effect phenomenon. The latter is associated with variation of nominal strength as a function of the size in geometrically similar structures. The study of size effect has been initiated in the early 1920's by performing several experiments on quasi-brittle materials [38] and developing a semi-empirical relation that predicts the ultimate strength of the structure based on the given characteristic dimension. Two different approaches have been employed, viz deterministic and stochastic theories. In the former one, the material strength is assumed to be uniform and the size effect is attributed to formation of fractured process zone. In the second approach, the randomness of material strength is accounted for leading to the so-called stochastic size effect. In general, it has been observed that increasing the size can significantly reduce the strength of the structure. At the same time, a more ductile behavior can be observed when scaling the structural size to a smaller dimension.

Over the last few decades an extensive research on the size effect had been conducted by Bazant and his co-workers and the main results are presented in the monograph [38]. The investigations deal with two types of concrete structures, i.e. with and without an initial notch. It has been shown that the brittleness of structures which contain an initial discontinuity progressively increases for larger sizes. On the other hand, the ultimate strength of structures without notch converges to a solution associated with linear elastic fracture mechanics. One of the main problems in relation to the proposed size effect laws is the incorporation of a number of empirical parameters which, for some cases, cannot be uniquely defined. Therefore, a more constructive way to investigate the size effect is the numerical analysis which incorporates an adequate procedure for describing the propagation of localized damage. In this work, the proposed volume averaging technique is employed. This scheme is verified for both tensile and compressive failure modes and the results are compared with the predictions based on size effect laws as well as the experimental data.

Moreover, the investigation of size effect phenomenon is extended to chemo-mechanical loading. It is demonstrated that a spontaneous failure may occur due to chemical interaction by changing the structural dimension under a sustained load.

In chapter 4, the mathematical framework is further enhanced, by invoking the mixture theory [39], to deal with progressive failure in reinforced concrete structures. A sets of static and kinematic constrains are incorporated to determine the stress/strain rate in each constituent based on the total imposed loading increment. The constitutive model is developed for the reinforced region both prior and after of formation of localized zone. For the latter case, the cohesive law in the fractured zone is formulated by considering the reinforcements as Timoshenko beams embedded in the intact material. The framework has been combined with 3D crack smoothening algorithm and used to simulate a number of experimental tests conducted on reinforced concrete structures.

In chapter 5, an illustrative example is provided which deals with the application of the approach outlined above to analysis of large scale structures. The example given is focused on the assessment of structural damage in a hydraulic structure, made of reinforced concrete, subjected to 100 years of continuing chemical reaction (ASR). The results pertain to the power house as well as the spillway, and the variation of displacements has been compared with the in-situ measurements.

It should be emphasized that the mathematical formulation presented here has been implemented in user material subroutine (UMAT) of the commercial software Abaqus. This includes the governing constitutive relations as well as the crack propagation strategies incorporating 3D smoothening algorithm.

Finally, note that given the format of this thesis, which includes three separate journal papers, there is a certain overlap in terms of describing the details of the formulation. This cannot be avoided in a sandwich type of presentation.

1.4 References

1. S.S. Hsieh, E.C. Ting, W.F. Chen, A plastic-fracture model for concrete, *International Journal of Solids and Structures*. **18** (1982) 181-197.
2. S. Pietruszczak, J. Jiang, F.A. Mirza, An elastoplastic constitutive model for concrete, *International Journal of Solids and Structures*. **24** (1988) 705-722.
3. J. Lubliner, J. Oliver, S. Oller, E. Onate, A plastic-damage model for concrete, *International Journal of Solids and Structures*. **25** (1989) 299-326.
4. O.C. Zienkiewicz, R.L. Taylor, The Finite Element Method, *McGraw-Hill*. 1977.
5. T.J. Hughes, The finite element method: linear static and dynamic finite element analysis, *Mineola, NY : Dover Publications*. 2000.
6. A. Hillerborg, M. Modéer, P.E. Petersson, Analysis of crack formation and crack growth in concrete by means of fracture mechanics and finite elements, *Cement and Concrete Research.* **6** (1976) 773-781.
7. P. Devloo, A three-dimensional adaptive finite element strategy, *Computers and Structures*. **38** (1991) 121-130.
8. T. Belytschko, M. Tabbara, H-Adaptive finite element methods for dynamic problems, with emphasis on localization. *International Journal for Numerical Methods in Engineering.* **36** (1993) 4245-4265.
9. O.C. Zienkiewicz, M.S. Huang, M. Pastor, Localization problems in plasticity using finite element with adaptive remeshing. *International Journal for Numerical and Analytical Methods in Geomechnics.* **19** (1995) 127-148.
10. S. Diamond, N. Thaulow, A study of expansion due to alkali-silica reaction as conditioned by the grain size of the reactive aggregate. *Cement and Concrete Research*. **4** (1974) 591-607.
11. S. Diamond, A review of alkali-silica reaction and expansion mechanisms. *Cement and Concrete Research*. **5** (1975) 329-346.
12. S. Pietruszczak, On the mechanical behavior of concrete subjected to alkali-aggregate reaction. *Computers and Structures*. **58** (1996) 1093-1097.
13. B. Capra, J. P. Bournael, Modeling of induced mechanical effects of alkali-aggregate reactions. *Cement and Concrete Research.* **28** (1998) 251-260.
14. Z. P. Bazant, A. Steffens, Mathematical model for kinetics of alkali-silica reaction in concrete. *Cement and Concrete Research*. **30** (2000) 419-428.

15. D. Ngo, A. Scordelis, Finite element analysis of reinforced concrete beams. *ACI Journal Proceedings*. **64** (1967) 152-163.

16. S. Pietruszczak, Z. Mroz. Finite element analysis of deformation of strain-softening materials. *International Journal for Numerical Methods in Engineering*. **17** (1981) 327-334.

17. R. de Borst, L. Sluys, H. Muhlhaus, J. Pamin. Fundamental issues in finite element analysis of localization of deformation. *Engineering Computations*. **10** (1993) 99-121.

18. J. Oliver. Modeling strong discontinuities in solid mechanics via strain softening constitutive equations. Part 2: *Numerical simulation. International Journal for Numerical methods in Engineering*. **39** (1996) 3601-3623.

19. J. Oliver. M. Cervera, O. Manzoli. Strong discontinuities and continuum plasticity models: the strong discontinuity approach. *International Journal of Plasticity*. **15** (1999) 319-351.

20. J. Simo, J. Oliver, F. Armero. An analysis of strong discontinuities induced by strain-softening in rate-independent inelastic solids. *Computational Mechanics*. **12** (1993) 277-296.

21. F. Armero, K. Garikipati. Recent advances in analysis and numerical simulation of strain localization in inelastic solids. *Computational Plasticity*. (1995) 547-561.

22. J. M. Melenk, I. Babuska, The partition of unity finite element method: Basic theory and applications. *Computer Methods in Applied Mechanics and Engineering*. **139** (1996) 289-314.

23. T. Belytschko. T. Black. Elastic crack growth in finite elements with minimal remeshing. *International Journal for Numerical Methods in Engineering*. **45** (1999) 601-620.

24. N. Moes. J. Dolbow. T. Belytschko. A finite element method for crack growth without remeshing. *International Journal for Numerical Methods in Engineering*. **46** (1999) 131-150.

25. G. N. Wells. L. J. Sluys. A new method for modeling cohesive cracks using finite elements. *International Journal for Numerical Methods in Engineering*. **50** (2001) 2667-2682.

26. N. Moes, T. Belytschko. Extended finite element method for cohesive crack growth. *Engineering Fracture Mechanics*. **69** (2002) 813-833.

27. J. Dolbow, N. Moes, T. Belytschko. An extended finite element method for modeling crack growth with frictional contact. *Computer Methods in Applied Mechanics and Engineering*. **190** (2001) 6825-6846.

28. C. Daux, N. Moes, J. Dolbow, N. Sukumar, T. Belytschko. Arbitrary branched intersecting cracks with the extended finite element method. *International Journal for Numerical Methods in Engineering*. **48** (2000) 1741-1760.

29. D. Deb, K. Das. Extended finite element method for the analysis of discontinuities in rock masses. *Geotechnical and Geological Engineering*. **28** (2010) 643-659.

30. J. Rethore, R. de Borst, M. Abellan. A two-scale approach for fluid flow in fractured porous media. *International Journal for Numerical Methods in Engineering*. **71** (2007) 780-800.

31. T. Mohammadnejad, A.R. Khoei. An extended finite element method for hydraulic fracture propagation in deformable porous media with the cohesive crack model. *Finite Elements in Analysis and Design*. **73** (2013) 77-95.

32. S. Pietruszczak. On the undrained response of granular soil involving localized deformation. *Journal of Engineering Mechanics*. **114** (1995) 1292-1298.

33. S. Pietruszczak. On homogeneous and localized deformation in water-infiltrated soils. *International Journal of Damage Mechanics*. **8** (1999) 233-253.

34. E. Haghighat, S. Pietruszczak. On modeling of discrete propagation of localized damage in cohesive-frictional materials. *International Journal for Numerical and Analytical Methods in Geomechanics*. **39** (2015) 1774-1790.

35. J.R. Rice, J.W. Rudnicki. A note on some features of the theory of localization of deformation. *International Journal of Solids and Structure*. **16** (1980) 597-605.

36. P. Dumstroff, G. Meschke. Crack propagation criteria in the framework of X-FEM-based structural analyses. *International Journal for Numerical and Analytical Methods in Geomechanics*. **31** (2007) 239-259.

37. T.C. Gasser, G.A. Holzapfel. 3D crack propagation in unreinforced concrete. A two-step algorithm for tracking 3D crack paths. *Computer Methods in Applied mechanics and Engineering*. **195** (2006) 5198-5219.

38. Z.P. Bazant, J. Planas. Fracture and size effect in concrete and other quasi-brittle materials. CRC Press, 1997.

39. S. Pietruszczak, A. Winnicki. Constitutive model for concrete with embedded sets of reinforcement. *Journal of Engineering Mechanics*. **129** (2003) 725-738.

2 Numerical analysis of propagation of macrocracks in 3D concrete structures affected by ASR

2.1 Contribution

In the article provided below, a mathematical description of three dimensional crack growth in concrete structures subjected to mechanical and/or chemical loading is presented. The focus is on concrete structures suffering from continuing alkali-silica reaction. The expansion of silica gel and the associated degradation of strength/deformation properties are monitored by a scalar parameter which describes the progress of the chemical interaction. In order to determine the stress rate at the end of each increment an enhanced implicit integration scheme has been implemented.

The main contribution in this work is the description of discrete crack propagation in concrete structures affected by alkali-silica-reaction. In the research conducted so far, the damage has been monitored using simplified ‘smeared’ approaches that suffer from numerical instabilities and, often, the sensitivity to FE discretization. Here, a rigorous approach is employed which incorporates volume averaging and attributes the strain softening to the mechanical characteristics within the fractured zone. In addition, the crack smoothening algorithm is developed and implemented within the code to increase the accuracy of predicting the crack paths. A series of examples is provided to verify the predictive abilities of this framework and the results are compared with available experimental evidence.

Numerical analysis of propagation of macrocracks in 3D concrete structures affected by ASR

S. Moallemi and S. Pietruszczak

Department of Civil Engineering, McMaster University, Hamilton, Ontario, Canada

ABSTRACT

In this study an implicit algorithm for modeling of propagation of macrocracks in 3D concrete structures suffering from alkali-silica reaction has been developed and implemented. The formulation of the problem prior to the onset of localized deformation is based on a chemo-elasticity approach. The localized deformation mode, involving the formation of macrocracks, is described using a simplified form of the strong discontinuity approach (SDA) that employs a volume averaging technique enhanced by a numerical procedure for tracing the propagation path in 3D space. The latter incorporates a non-local smoothening algorithm. The formulation is illustrated by a number of numerical examples that examine the crack propagation pattern in both plain and reinforced concrete under different loading scenarios.

Key Words: 3D crack propagation; volume averaging; alkali-silica reaction; reinforced concrete

2.2 Introduction

One of the most important factors which can affect the durability of concrete structures is the alkali-silica-reaction (ASR). In recent decades several experimental and numerical studies have

been conducted to understand this chemical process and to reduce the vulnerability of important structures such as dams and power plants. Although the chemistry behind the reaction is not completely understood, it has been generally accepted that in the presence of water the alkaline components of cement may react with silica present in the aggregate and produce a silica gel [1]. The experimental work has shown that the kinetics of this chemical process is a function of relative humidity, temperature, type of aggregates as well as the stress state [2-5]. As the silica gel is formed and absorbs water, it can expand throughout the concrete mass and induce damage within its microstructure. First, the swelling gel fills the pores in the concrete skeleton and subsequently the pressure is exerted on constituents which leads to formation of microcracks and the reduction of concrete strength.

The research on development of continuum approaches describing the chemo-mechanical interaction started in the mid 1990's [6, 7]. Later, several derivative concepts were proposed that included both the continuum models (e.g. [8, 9]) as well as micromechanical descriptions of ASR-induced deformation (cf. [10]). It needs to be pointed out that there have only been a few isolated attempts to perform large-scale simulations that involved the actual engineering structures. Most of these attempts (e.g. [9, 11]) dealt primarily with the assessment of the influence of concrete expansion on the structural integrity, without accounting for the reaction-dependent evolution of material properties and a rather simplistic description of the onset and propagation of localized damage, particularly in compression regime.

Modeling of the progressive failure within the finite element framework has received a significant attention over the last few decades. A large number of studies have been conducted dealing with the onset and propagation of cracks in tensile regime [12, 13] as well as the formation of shear bands in compressive zones [14, 15]. The use of the standard finite element methodology has some limitations for modeling discontinuities. In order to overcome these limitations, the so-called strong discontinuity approach (SDA) was developed [16, 17] in which the mesh sensitivity is reduced by embedding the displacement discontinues within the element. In this approach, a discontinuity function is added to the consistent part of the displacement field by employing new degrees of freedom in enhanced element [18]. Another scheme that incorporates the embedded discontinuity approach is known as eXtended Finite Element Method (XFEM). The latter involves

the nodes enrichment within the enhanced element and employs the concept of partition of unity to update the related shape functions [19-21].

In this study, a simplified form of strong discontinuity approach based on the concept of averaging over a volume adjacent to the macrocrack is examined. The procedure was developed in the early 1980's [22] and later modified in ref. [23]. Here, an enhanced approach based on the recent work reported by Haghighat and Pietruszczak [24] is employed that allows for a discrete representation of the crack propagation. The original methodology outlined in ref. [24] is extended here to 3D problems and the problem is reformulated to address the damage induced by continuing ASR. In the next section, an implicit formulation for chemo-mechanical interaction in concrete is developed. Later on, in section 3, the constitutive relation in the presence of discontinuity is discussed. In section 4, the procedure for tracing the path of crack propagation in three dimensional domain is explained and a smoothening algorithm is outlined. Finally, in the last section several numerical examples of damage propagation in plain and reinforced concrete structures subjected to various loading configurations, including chemical interaction and/or mechanical load, are presented.

2.3 Research significance

The integrity of civil structures (e.g., dams, bridges, structures in hydraulic/nuclear power generation facilities, etc.) is essential for maintaining their continuing operation. As these structures age, a progressive damage takes place due to environmental influences as well as continuing chemical interaction. The fundamental aspects addressed in this research deal with modelling of the mechanical effects of alkali-aggregate reaction (ASR) and the associated process of the onset and propagation of localized failure.

The importance of ensuring the safety of strategic civil structures cannot be overemphasized. Compromising it poses significant risks to the public, to the environment as well as to the economy. Therefore, the primary motivation of this work is an understanding of the nature of the damage process and its suitable mathematical description. The latter is crucial for forecasting and adequate mitigation of the long-term effects of aging-related degradation.

2.4 Mathematical description of chemo-mechanical interaction in concrete

There are two main aspects involved in simulation of ASR in concrete, which are considered in a phenomenological framework: (i) the kinetics of the reaction and (ii) the degradation of mechanical properties of concrete. The former, i.e. the kinetics of the reaction, may be defined by introducing a scalar parameter ζ which is an explicit function of time and its evolution is affected by humidity, temperature and the confining pressure. In this study, humidity and temperature are considered constant, and an exponential relation (cf. ref. [25]) is used to describe the kinetics of reaction, viz.

$$\zeta = 1 - \exp\left(-A_1 t\right) \tag{2-1}$$

where A_1 is a material constant which controls the rate of the reaction. As it can be seen, ζ is defined within the interval $[0,1)$ whereas the reaction time varies within $[0,\infty)$.

Degradation of concrete begins as soon as the macrocracks caused by the expansion of silica gels, start to appear. This affects both the deformation and strength properties. Restricting ourselves to the class of problems that involve failure in the *tensile* regime, the evolution laws for the modulus of elasticity and tensile strength may be expressed in the following form

$$E = E_0\left(1 - G_E\,\zeta\right) \qquad f_t = f_{t0}\left(1 - G_f\,\zeta\right) \tag{2-2}$$

where, E_0 and f_{t0} are the initial values before the onset of the reaction and G_E and G_f are material constants that control the rate of degradation and can be identified from relevant experiments. Within the current framework, the chemical strain $\boldsymbol{\varepsilon}_{\mathbf{ASR}}$ is defined as a function of the kinetics of reaction and the confining pressure, i.e.

$$\boldsymbol{\varepsilon}_{\mathbf{ASR}} = \frac{1}{3}\left[\mathrm{B}(\boldsymbol{\sigma})\;\zeta\;\varepsilon_\infty\right]\mathbf{I}\,, \qquad \mathrm{B}(\boldsymbol{\sigma}) = \begin{cases} \exp\left(-\dfrac{A_2\,tr\left(\boldsymbol{\sigma}\right)}{f_c}\right) & tr\left(\boldsymbol{\sigma}\right) < 0 \\ 1.0 & tr\left(\boldsymbol{\sigma}\right) > 0 \end{cases} \tag{2-3}$$

in which ε_∞ is the maximum volumetric free expansion for a given alkali content, A_2 is a material constants, f_c denotes the compressive strength of concrete and $\mathbf{I}$ is the identity tensor. Note that $B(\boldsymbol{\sigma})$ describes the effect of confinement, which reduces the total ASR-related expansion, as reported in the literature [26, 27].

The constitutive relation may now be formulated within the framework of chemo-elasticity. In this case,

$$\boldsymbol{\sigma} = \mathbb{D}^{e} : \boldsymbol{\varepsilon}_{\mathbf{e}} = \mathbb{D}^{e} : (\boldsymbol{\varepsilon} - \boldsymbol{\varepsilon}_{\mathbf{ASR}}) \tag{2-4}$$

where $\mathbb{D}^{e}$ is the elastic stiffness, and $\boldsymbol{\varepsilon}$ and $\boldsymbol{\varepsilon}_{\mathbf{e}}$ are total and elastic strain, respectively. By differentiating of eq. (2-4) with respect to time and also taking into account the variation of material properties during the continuing reaction, one can write

$$\dot{\boldsymbol{\sigma}} = \mathbb{D}^{e} : (\dot{\boldsymbol{\varepsilon}} - \dot{\boldsymbol{\varepsilon}}_{\mathbf{ASR}}) + \dot{\mathbb{D}}^{e} : \left[\mathbb{D}^{e}\right]^{-1} : \boldsymbol{\sigma} \tag{2-5}$$

where, the rate of change of elastic stiffness and the ASR-induced strain rate can be defined as

$$\dot{\mathbb{D}}^{e} = \frac{\partial \mathbb{D}^{e}}{\partial E}\frac{\partial E}{\partial \zeta}\frac{\partial \zeta}{\partial t}, \qquad \dot{\boldsymbol{\varepsilon}}_{\mathbf{ASR}} = \frac{1}{3}\varepsilon_\infty \left[\zeta \frac{\partial B(\boldsymbol{\sigma})}{\partial \boldsymbol{\sigma}} : \dot{\boldsymbol{\sigma}} + B(\boldsymbol{\sigma})\dot{\zeta}\right]\mathbf{I} \tag{2-6}$$

By substituting the above relation into (2-5) the stress rate can be expressed as

$$\begin{aligned} \dot{\boldsymbol{\sigma}} &= \left[\mathbb{T}\right]^{-1} : \left\{\mathbb{D}^{e} : (\dot{\boldsymbol{\varepsilon}} - \dot{\boldsymbol{\varepsilon}}_{\mathbf{c}}) + \dot{\mathbb{D}}^{e} : \left[\mathbb{D}^{e}\right]^{-1} : \boldsymbol{\sigma}\right\} \\ \mathbb{T} &= \left[\mathbb{I} + \frac{1}{3}\zeta\, \varepsilon_\infty\, \mathbb{D}^{e} : \left(\partial_{\boldsymbol{\sigma}} B \otimes \mathbf{I}\right)\right], \quad \dot{\boldsymbol{\varepsilon}}_{\mathbf{c}} = \left(\frac{1}{3}\varepsilon_\infty B(\boldsymbol{\sigma})\dot{\zeta}\right)\mathbf{I} \end{aligned} \tag{2-7}$$

In the numerical integration process, two different schemes can be employed, i.e. either explicit or implicit. In the explicit scheme, the stress state at time t_{n+1} can be determined directly by using the values of internal parameters at the previous time step t_n; whereas in implicit scheme, the unknowns at time t_{n+1} can be found through an iterative process by satisfying constrains at the

current time [28] . Based on eq.(2-7), the stress increment at each time step Δt can be approximated by the backward Euler scheme. Thus,

$$\boldsymbol{\sigma}_{t+\Delta t} = \boldsymbol{\sigma}_t + \dot{\boldsymbol{\sigma}}_{t+\Delta t}\,\Delta t = \boldsymbol{\sigma}_t + \left[\mathbb{T}\right]^{-1} : \left\{ \mathbb{D}^{\mathrm{e}} : \left(\dot{\boldsymbol{\varepsilon}} - \dot{\boldsymbol{\varepsilon}}_{\mathbf{c}}\right)\Delta t + \dot{\mathbb{D}}^{\mathrm{e}} : \left[\mathbb{D}^{\mathrm{e}}\right]^{-1} : \boldsymbol{\sigma}_{t+\Delta t}\,\Delta t \right\} \tag{2-8}$$

By solving for $\boldsymbol{\sigma}_{t+\Delta t}$ we have

$$\boldsymbol{\sigma}_{t+\Delta t} = \mathbb{Q}^{-1} : \left[\boldsymbol{\sigma}_t + \mathbb{D}^{e} : \mathbb{T}^{-1} : \left(\dot{\boldsymbol{\varepsilon}} - \dot{\boldsymbol{\varepsilon}}_{\mathbf{c}}\right)\Delta t\right], \qquad \mathbb{Q} = \mathbb{I} + \mathbb{T}^{-1} : \mathbb{D}^{e} : \left[\dot{\mathbb{D}}^{e}\right]^{-1}\Delta t \tag{2-9}$$

where $\mathbb{I}$ is the fourth order identity tensor and $\boldsymbol{\sigma}_t$ is the stress state at the beginning of increment.

In order to define the tangential stiffness operator, eq. (2-7) may be written as

$$\Delta\boldsymbol{\sigma}_{t+\Delta t} = \dot{\boldsymbol{\sigma}}_{t+\Delta t}\,\Delta t = \mathbb{T}^{-1} : \mathbb{D}^{\mathrm{e}} : (\Delta\boldsymbol{\varepsilon} - \Delta\boldsymbol{\varepsilon}_{\mathbf{c}}) + \mathbb{T}^{-1} : \dot{\mathbb{D}}^{\mathrm{e}} : \left[\mathbb{D}^{\mathrm{e}}\right]^{-1} : \left(\boldsymbol{\sigma}_t + \Delta\boldsymbol{\sigma}_{t+\Delta t}\right) \tag{2-10}$$

which, after some algebraic manipulations, leads to

$$\Delta\boldsymbol{\sigma}_{t+\Delta t} = \mathbb{Q}^{-1} : \mathbb{T}^{-1} : \mathbb{D}^{\mathrm{e}} : \left(\Delta\boldsymbol{\varepsilon} - \Delta\boldsymbol{\varepsilon}_{\mathbf{c}} - \Delta t\left[\dot{\mathbb{D}}^{e}\right]^{-1} : \boldsymbol{\sigma}_t\right) = \mathbb{D}_{\mathbb{T}} : \left(\Delta\boldsymbol{\varepsilon} - \Delta\boldsymbol{\varepsilon}^{*}\right) \tag{2-11}$$

where $\mathbb{D}_{\mathbb{T}}$ is the tangential operator and $\Delta\boldsymbol{\varepsilon}^{*}$ is the total strain generated by the chemical reaction.

2.5 Modeling of discontinuous deformation

In this section a mathematical description for a cracked domain subjected to chemical reaction is presented by incorporating a volume averaging scheme. The criterion for the crack initiation and the traction-separation law are discussed and an implicit formulation for updating the crack characteristics is developed.

2.5.1 Description of macrocrack propagation by a volume averaging technique

Consider a domain contained within the volume Ω in which Γ_d denotes discontinuity surface which splits this domain into Ω^+ and Ω^- (Fig 2-1). The unit vector normal to crack is denoted by $\mathbf{n}$ and points to Ω^+.

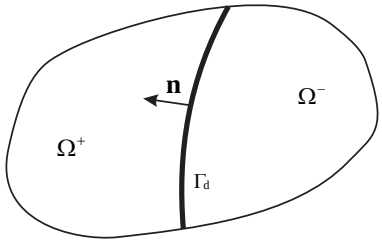

Fig 2-1- definition of representative elementary volume

Within this domain, the displacement field, $\mathbf{u}(\mathbf{x},t)$ can be expressed as a combination of two continuous fields $\bar{\mathbf{u}}(\mathbf{x},t)$ and $\mathbf{u}\ (\mathbf{x},t)$ with the discontinuous jump function, $H(\mathbf{x})$ as [16]

$$\mathbf{u}(\mathbf{x},t)=\bar{\mathbf{u}}(\mathbf{x},t)+H(\mathbf{x})\ \mathbf{u}\ (\mathbf{x},t) \tag{2-12}$$

where, $H(\mathbf{x})$ is the Heaviside function which is equal to zero for all points in Ω^- and is equal to unity in the remaining part of the domain

$$H(\mathbf{x})=\begin{cases}1 & \mathbf{x}\in\Omega^+\\ 0 & \mathbf{x}\in\Omega^-\end{cases} \tag{2-13}$$

The terms defined in (2-12) are depicted in Fig 2-2 to illustrate the displacement function in the context of a one-dimensional problem.

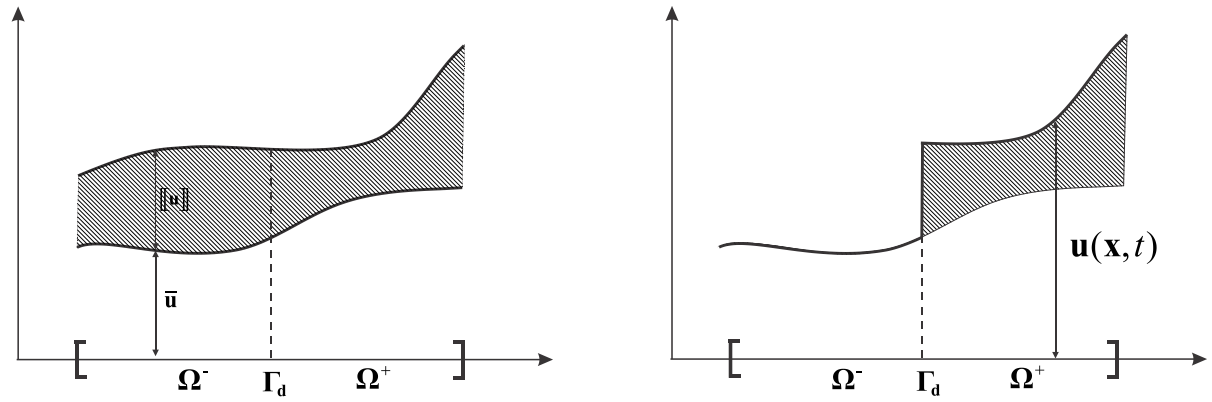

Fig 2-2-decomposition of displacement field for 1-D case

Here, the dashed line indicates the position of discontinuity. The strain tensor is calculated from the gradient of the displacement field (2-12)

$$\boldsymbol{\varepsilon} = \nabla^s \mathbf{u}(\mathbf{x},t) = \nabla^s \bar{\mathbf{u}}(\mathbf{x},t) + \nabla^s \ \mathbf{u}\ (\mathbf{x},t).H(\mathbf{x}) + \ \mathbf{u}\ (\mathbf{x},t) \otimes \nabla^s H(\mathbf{x}) \tag{2-14}$$

where the superscript s denotes the symmetric part of the gradient operator. Now, by averaging (2-14) over the considered volume yields [24]

$$\frac{1}{\Delta\Omega}\int_\Omega \boldsymbol{\varepsilon}\, \mathrm{d}\Omega = \frac{1}{\Delta\Omega}\left\{\int_\Omega \nabla^s \bar{\mathbf{u}}(\mathbf{x},t)\, \mathrm{d}\Omega + \int_\Omega \nabla^s \ \mathbf{u}\ (\mathbf{x},t).H(\mathbf{x})\, \mathrm{d}\Omega + \int_\Omega \ \mathbf{u}\ (\mathbf{x},t) \otimes \nabla^s H(\mathbf{x})\, \mathrm{d}\Omega \right\} \tag{2-15}$$

Referring to [16], the gradient of the Heaviside step function is defined by delta Dirac function as $\nabla H(x) = \delta_{\Gamma_\mathrm{d}} \mathbf{n}$, so that eq.(2-15) can be simplified to

$$\frac{1}{\Delta\Omega}\int_\Omega \boldsymbol{\varepsilon}\, \mathrm{d}\Omega = \frac{1}{\Delta\Omega}\left\{\int_\Omega \nabla^s \bar{\mathbf{u}}(\mathbf{x},t)\, \mathrm{d}\Omega + \int_\Omega \nabla^s \ \mathbf{u}\ (\mathbf{x},t).H(\mathbf{x})\, \mathrm{d}\Omega + \int_{\Gamma_\mathrm{d}} \left(\boldsymbol{w}(\mathbf{x},t) \otimes \mathbf{n}\right)^s \mathrm{d}\Gamma_\mathrm{d} \right\} \tag{2-16}$$

where $\boldsymbol{w}(\mathbf{x},t)$ indicates the displacement discontinuity. Thus, in terms of the volume average, the strain rate within the considered domain can be approximated by

$$\dot{\boldsymbol{\varepsilon}} = \nabla^s \dot{\bar{\mathbf{u}}}(\mathbf{x},t) + \left(\frac{\Delta\Omega^+}{\Delta\Omega}\right)\nabla^s \ \dot{\mathbf{u}}\ (\mathbf{x},t) + \left(\frac{\Delta\Gamma_\mathrm{d}}{\Delta\Omega}\right)\left(\dot{\boldsymbol{w}}(\mathbf{x},t) \otimes \mathbf{n}\right)^s \tag{2-17}$$

Given the expression above, the total strain rate can be interpreted as a superposition of two parts, i.e. the strain rate in the intact material, $\dot{\tilde{\boldsymbol{\varepsilon}}}$, and the strain rate in cracked zone, $\dot{\hat{\boldsymbol{\varepsilon}}}$, i.e.

$$\dot{\boldsymbol{\varepsilon}}=\dot{\tilde{\boldsymbol{\varepsilon}}}+\dot{\hat{\boldsymbol{\varepsilon}}}\ ;\ \textit{where}\quad \begin{aligned}\dot{\tilde{\boldsymbol{\varepsilon}}}&=\nabla^{s}\left(\dot{\tilde{\mathbf{u}}}(\mathbf{x},t)+\left(\frac{\Delta\Omega^{+}}{\Delta\Omega}\right)\ \dot{\mathbf{u}}\ \ (\mathbf{x},t)\right)\\ \dot{\hat{\boldsymbol{\varepsilon}}}&=\chi\left(\dot{\boldsymbol{w}}(\mathbf{x},t)\otimes\mathbf{n}\right)^{s}\end{aligned} \tag{2-18}$$

where χ denotes the ratio of the area of the crack over the referential volume. In order to satisfy the equilibrium condition, the traction along the crack surfaces should be continuous. Thus,

$$\mathbf{n}.\dot{\boldsymbol{\sigma}}=\dot{\mathbf{t}}=\mathbf{K}\,\dot{\boldsymbol{w}} \tag{2-19}$$

where, $\mathbf{t}$ is the traction vector and $\mathbf{K}$ is the stiffness of the fractured zone in the global coordinate system. Substituting eq. (2-19) into the constitutive relation for intact material (2-11), we have

$$\mathbf{n}.\mathbb{D}_{\mathrm{T}}:\left(\dot{\tilde{\boldsymbol{\varepsilon}}}-\dot{\boldsymbol{\varepsilon}}^{*}\right)=\mathbf{n}.\mathbb{D}_{\mathrm{T}}:\left(\dot{\boldsymbol{\varepsilon}}-\dot{\hat{\boldsymbol{\varepsilon}}}-\dot{\boldsymbol{\varepsilon}}^{*}\right)=\mathbf{n}.\mathbb{D}_{\mathrm{T}}:\left(\dot{\boldsymbol{\varepsilon}}-\dot{\boldsymbol{\varepsilon}}^{*}\right)-\chi\,\mathbf{n}.\mathbb{D}_{\mathrm{T}}.\mathbf{n}\ \dot{\boldsymbol{w}}=\mathbf{K}\,\dot{\boldsymbol{w}} \tag{2-20}$$

Consequently, by solving for $\dot{\boldsymbol{w}}$ in eq. (2-20), the velocity discontinuity can be defined as

$$\dot{\boldsymbol{w}}=\left(\mathbf{S}\otimes\mathbf{n}\right):\left[\mathbb{D}_{\mathrm{T}}:\left(\dot{\boldsymbol{\varepsilon}}-\dot{\boldsymbol{\varepsilon}}^{*}\right)\right];\quad \textit{where}\quad \mathbf{S}=\left[\mathbf{K}+\chi\,\mathbf{n}.\mathbb{D}_{\mathrm{T}}.\mathbf{n}\right]^{-1} \tag{2-21}$$

Finally, substituting eq. (2-21) into the constitutive relation for intact material, the global relation between the total stress and strain rates can be obtained. The latter takes the form

$$\dot{\boldsymbol{\sigma}}=\mathbb{D}_{\mathrm{T}}:\left(\dot{\boldsymbol{\varepsilon}}-\dot{\boldsymbol{\varepsilon}}^{*}\right)-\chi\mathbb{D}_{\mathrm{T}}:\left(\mathbf{n}\otimes\dot{\boldsymbol{w}}\right)=\mathbb{D}_{\mathrm{T}}:\left[\mathbb{I}-\chi\left(\mathbf{n}\otimes\mathbf{S}\otimes\mathbf{n}\right):\mathbb{D}_{\mathrm{T}}\right]:\left(\dot{\boldsymbol{\varepsilon}}-\dot{\boldsymbol{\varepsilon}}^{*}\right)=\bar{\mathbb{D}}_{\mathrm{T}}:\left(\dot{\boldsymbol{\varepsilon}}-\dot{\boldsymbol{\varepsilon}}^{*}\right) \tag{2-22}$$

where $\bar{\mathbb{D}}_{\mathrm{T}}$ is the fourth order tangential operator.

2.5.2 Constitutive relation for the macrocrack

In this section the constitutive law for the fractured zone is discussed which relates the traction rate to the velocity discontinuity. Over the last few decades, different types of cohesive relations have been proposed to define the characteristics of crack in different propagation modes. In order to obtain a symmetric stiffness operator for tensile cracks, the concepts of equivalent displacement,

w_{eq}, and equivalent traction, t_{eq}, is used here as defined in refs. [29, 30]. The constitutive law is taken in the form

$$t_{eq} = \hat{K}\, w_{eq}, \quad w_{eq} = \sqrt{w_n^2 + \beta^2 \left(w_{s1}^2 + w_{s2}^2 \right)} \tag{2-23}$$

where $\hat{K}$ is defined as

$$\hat{K} = K_0 \frac{d_0}{d} \exp\left(-\frac{f_t}{G_f}(d - d_0) \right) \tag{2-24}$$

In the equations above, the scalar parameter β controls the effect of shear sliding on the equivalent traction, while w_n and w_s denote displacement jumps in the normal and tangential direction, respectively, in the local coordinate system attached to the crack. Furthermore, K_0 is the initial stiffness, d_0 denotes the equivalent displacement at which the attenuation of stiffness starts, d is the maximum equivalent displacement during the loading history, f_t represents the tensile strength and G_f is the fracture energy. It is noted that for $\beta = 0$ the stiffness operator $\hat{K}$ has the same form as that suggested by Wells and Sluys [31]. In order to obtain an explicit form of the constitutive relation in terms of normal and tangential tractions, the concept of total equivalent work is implemented, viz.

$$t_{eq}\, \dot{w}_{eq} = t_n\, \dot{w}_n + t_{s1}\, \dot{w}_{s1} + t_{s2}\, \dot{w}_{s2} \tag{2-25}$$

By evaluating the rate of w_{eq} in eq. (2-23) and using relation (2-25), we have

$$t_{eq} \left(\frac{w_n}{w_{eq}} \dot{w}_n + \beta^2 \frac{w_{s1}}{w_{eq}} \dot{w}_{s1} + \beta^2 \frac{w_{s2}}{w_{eq}} \dot{w}_{s2} \right) = t_n\, \dot{w}_n + t_{s1}\, \dot{w}_{s1} + t_{s2}\, \dot{w}_{s2} \tag{2-26}$$

By comparing the two sides of eq. (2-26) and using (2-23) one can write

$$t_n = \hat{K}\, w_n, \quad t_{s1} = \beta^2 \hat{K}\, w_{s1}, \quad t_{s2} = \beta^2\, \hat{K}\, w_{s2} \tag{2-27}$$

In order to define now the second order tensor $\mathbf{K}$, viz. eq. (2-19), the rate form of eq. (2-27) should be employed, i.e.

$$\dot{t}_n = \dot{\hat{K}}\, w_n + \hat{K}\, \dot{w}_n ; \quad \dot{t}_{s1} = \beta^2 \left(\dot{\hat{K}}\, w_{s1} + \hat{K}\, \dot{w}_{s1} \right); \quad \dot{t}_{s2} = \beta^2 \left(\dot{\hat{K}}\, w_{s2} + \hat{K}\, \dot{w}_{s2} \right) \tag{2-28}$$

It should be noted that the case of $\dot{d} > 0$ corresponds to an active loading process, whereby a continuing damage takes place, whereas $\dot{d} = 0$ defines unloading. In the former case, using relations (2-24) and (2-28), and noting that $d = w_{eq}$, leads to a following expression for the stiffness tensor $\mathbf{K}$

$$\mathbf{K} = \hat{K} \left(\frac{G_f + w_{eq} f_t}{w_{eq}^2 G_f} \right) \begin{bmatrix} \dfrac{w_{eq}^2 G_f}{G_f + w_{eq} f_t} - w_n^2 & -\beta^2 w_n w_{s1} & -\beta^2 w_n w_{s2} \\ -\beta^2 w_n w_{s1} & \dfrac{\beta^2 w_{eq}^2 G_f}{G_f + w_{eq} f_t} - \beta^4 w_{s1}^2 & -\beta^4 w_{s1} w_{s2} \\ -\beta^2 w_n w_{s2} & -\beta^4 w_{s1} w_{s2} & \dfrac{\beta^2 w_{eq}^2 G_f}{G_f + w_{eq} f_t} - \beta^4 w_{s2}^2 \end{bmatrix} \tag{2-29}$$

Following the same procedure for the case of unloading, one obtains

$$\mathbf{K} = \hat{K} \begin{bmatrix} 1 & 0 & 0 \\ 0 & \beta^2 & 0 \\ 0 & 0 & \beta^2 \end{bmatrix} \tag{2-30}$$

2.5.3 Implicit integration for updating the crack characteristics

For an active loading process, the mechanical response of the macrocrack can be traced by using an implicit integration scheme, similar to that outlined in ref. [24]. In this case, the following residuals at increment *n* and iteration *k* are defined

$$\begin{aligned} \boldsymbol{R}_1^k &= \boldsymbol{n}.\dot{\boldsymbol{\sigma}}_n^k - \mathbf{K}\, \dot{\boldsymbol{w}}_n^k = \boldsymbol{0} \\ \boldsymbol{R}_2^k &= \dot{\boldsymbol{\sigma}}_n^k - \mathbb{D}_{\mathrm{T}} : \left(\dot{\boldsymbol{\varepsilon}} - \dot{\boldsymbol{\varepsilon}}^* \right) + \chi\, \mathbb{D}_{\mathrm{T}} : \left(\boldsymbol{n} \otimes \dot{\boldsymbol{w}}_n^k \right) = \boldsymbol{0} \end{aligned} \tag{2-31}$$

Employing Newton-Raphson algorithm, these can be approximated as

$$\begin{aligned} \boldsymbol{R}_1^{k+1} &\approx \boldsymbol{R}_1^k + \frac{\partial \boldsymbol{R}_1^k}{\partial \boldsymbol{\sigma}} : \boldsymbol{\delta\sigma}^k + \frac{\partial \boldsymbol{R}_1^k}{\partial \boldsymbol{w}} \boldsymbol{\delta w}^k = \mathbf{0} \\ \boldsymbol{R}_2^{k+1} &\approx \boldsymbol{R}_2^k + \frac{\partial \boldsymbol{R}_2^k}{\partial \boldsymbol{\sigma}} : \boldsymbol{\delta\sigma}^k + \frac{\partial \boldsymbol{R}_2^k}{\partial \boldsymbol{w}} \boldsymbol{\delta w}^k = \mathbf{0} \end{aligned} \tag{2-32}$$

Substituting eqs. (2-31) into (2-32) yields

$$\begin{aligned} \boldsymbol{\delta w}^k &= \left[\mathbf{K} + \chi \boldsymbol{n}.\, \mathbb{D}_{\mathrm{T}}.\boldsymbol{n}\right]^{-1} \left(\boldsymbol{R}_1^k - \boldsymbol{n}.\boldsymbol{R}_2^k\right) \\ \boldsymbol{\delta\sigma}^k &= -\chi\, \mathbb{D}_{\mathrm{T}} : \left(\boldsymbol{n} \otimes \boldsymbol{\delta w}^k\right) - \boldsymbol{R}_2^{\boldsymbol{k}} \end{aligned} \tag{2-33}$$

This procedure is continued until the residuals given in eq. (2-31) vanish. Note that at the end of each iteration the updated values of stress and crack opening are given by

$$\begin{aligned} \boldsymbol{\sigma}_n^k &= \boldsymbol{\sigma}_n + \Delta\boldsymbol{\sigma}_n^k \;; \quad \Delta\boldsymbol{\sigma}_n^k = \Delta\boldsymbol{\sigma}_n^{k-1} + \boldsymbol{\delta\sigma}_n^k \\ \boldsymbol{w}_n^k &= \boldsymbol{w}_n + \Delta\boldsymbol{w}_n^k \;; \quad \Delta\boldsymbol{w}_n^k = \Delta\boldsymbol{w}_n^{k-1} + \boldsymbol{\delta w}_n^k \end{aligned} \tag{2-34}$$

2.6 Three dimensional crack propagation strategy

Referring to Jäger et al. [32], there are three different approaches for tracing the crack path in 3D problems, i.e. level set, global tracking and local tracking. Owing to high computational cost of the first two schemes, the local tracking approach is employed in this study. In what follows, the main strategy is presented first for 2D case and then extended to 3D applications. Referring to Fig 2-3, each crack is composed of a number of line segments which pass through elements and cut the sides at two points. The location of these points is stored in order to trace the crack and also to define the characteristic length parameter, χ , eq. (2-18). At the end of each load increment, two steps are required to update the crack configuration; the first one involves checking the failure criterion for the elements next to the crack tip, and the second deals with identifying elements which satisfy failure condition to establish a new crack within the domain. In the former case, the cut side of the crack tip element is searched to find the new candidate crack element with the joint side. If the failure condition is satisfied, the crack will propagate from the cut point (former crack tip) in the direction perpendicular to maximum tensile stress (for tensile fracture) to form a new crack tip.

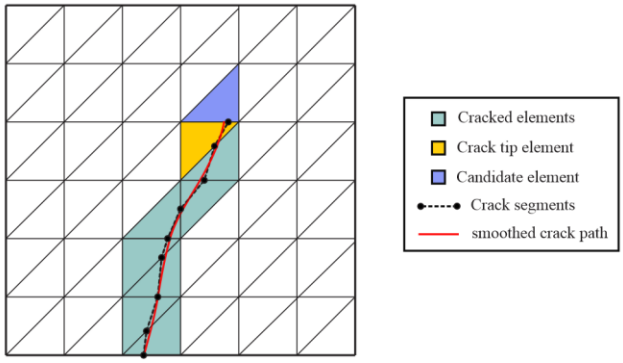

Fig 2-3- Crack propagation algorithm in 2D problem

This methodology has been extensively used, as reflected in the existing literature [31,33, 34]. In analogy to 2D case, a similar procedure can be implemented for three dimensional problems, whereby the triangular elements are replaced by a tetrahedral mesh and the crack segment is replaced by the crack surface. Fig 2-4 depicts cracked elements containing a failure plane. As the crack propagates, new tip-facets are identified and the neighbor elements become candidate elements for the next crack tip. As pointed out in ref. [35], using local tracking algorithm without modification cannot give reliable results, thereby a smoothing algorithm is employed here to overcome the difficulties related to 3D crack propagation. Here a brief review of this procedure is given.

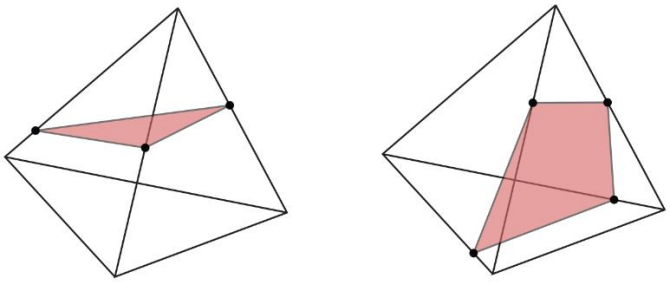

Fig 2-4-Crack surface in tetrahedral elements

The geometric scheme is shown in Fig 2-5 where the bold lines define the crack edge and the thin lines are associated with cut surface in cracked elements. As the failure criterion is met in the crack front element, direction of propagation is calculated and compared with that in the adjacent element. In some cases the obtained crack segment may not be consistent with the crack surface,

hence the smoothening is imposed to modify the crack propagation direction. It is noted that crack surface embedded in the new crack tip elements initiates from the point obtained as an average of cut facets in neighbor elements (point *P*). To adjust the normal direction, all points within the radius *R* of the current crack tip, which formed other crack surfaces, are picked to define a new surface to approximate normal vector at any point of interest.

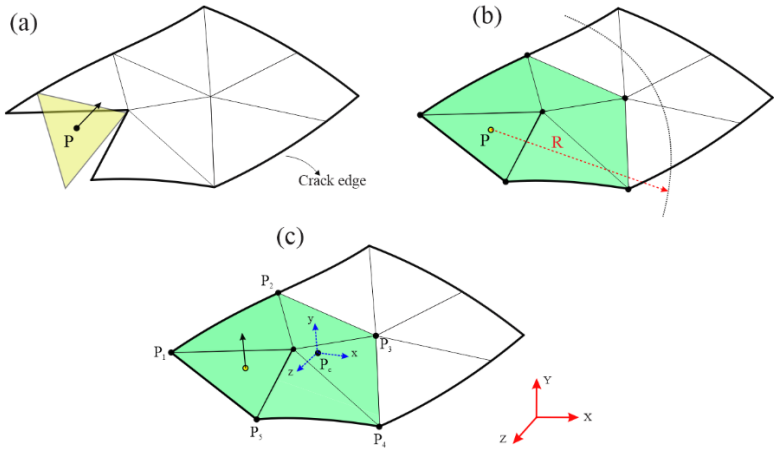

Fig 2-5-(a) Crack surface with an inappropriate normal direction in candidate crack; (c) Smoothening of crack surface

In the first step, the centroid of the new surface, referred to as P_c, is obtained. To define the equation of the crack surface, the local coordinate system is introduced and placed at the centroid point. As discussed in ref. [35], to obtain the local axis, the following covariance tensor is defined

$$\mathbf{T} = \sum_{i=1:\,n_p} \left(P_i - P_c\right) \otimes \left(P_i - P_c\right) \tag{2-35}$$

where P_i is the location of cut points in the cracked surface and n_p defines number of these points. The eigenvectors of this tensor define the local coordinate system located at P_c. To achieve more accuracy, the second order approximation is considered for the surface, i.e.

$$z = a_0 + a_1 x + a_2 y + a_3 x^2 + a_4 y^2 + a_5 xy \tag{2-36}$$

and the coefficients of approximation a_i, are determined by minimizing the difference between z and z_i, where the latter is the value of the function in equation (2-36) at point P_i. Therefore, the problem can be formulated as a least square problem

$$\text{minimize } \Psi = \sum_{i=1:n_R} \left(z - z_i\right)^2 \quad \textit{solve for } a_i \tag{2-37}$$

Once the solution is obtained, the direction of the normal at point *P* can be determined by calculating the gradient of (2-36), Note that this direction is defined in the local coordinate system and it should be transformed to the global frame of reference.

2.7 Numerical examples

In this section several numerical examples are provided to demonstrate the robustness of the constitutive models presented in Sections 2-3, together with the proposed scheme for tracing the crack propagation. The constitutive laws have been implemented into Abaqus user subroutine UMAT.

2.7.1 L-Shape concrete panel

In the first example the crack trajectory is investigated in an L-shaped plain concrete panel. The geometry and the FE discretization are shown in Fig 2-6. The bottom of the L-shaped specimen is fixed and the vertical displacement is applied incrementally to the left edge of the panel.

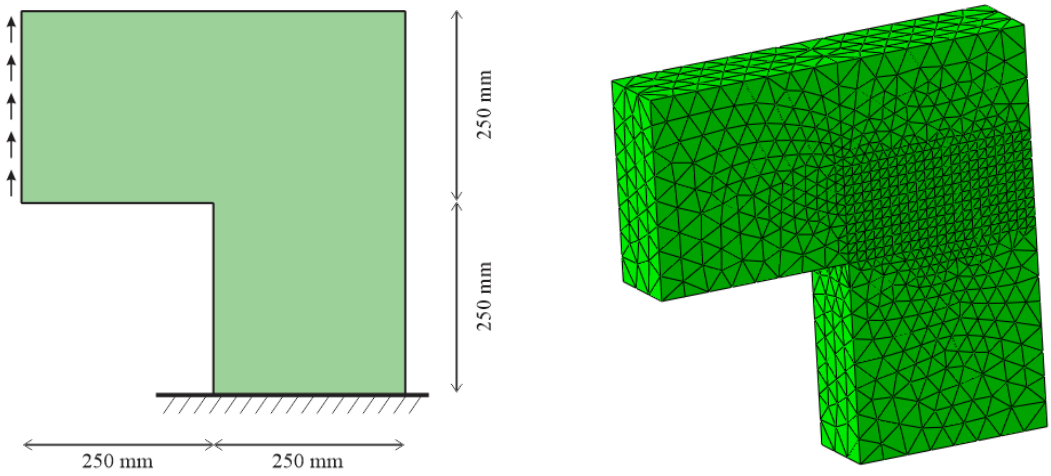

Fig 2-6 (Left) Geometry and boundary condition of problem; (Right) Finite element discretization (note 1 m = 39.37 in)

This example simulates an experimental set up of Winkler [36] and was previously employed as a benchmark for examining the accuracy of different numerical approaches for modeling of the crack propagation [29, 32]. The material is considered here as elastic-brittle and the assumed properties are (Note that 1MPa = 145 psi and 1N/mm = 5.71 lb/in)

$$E = 25.85\ (GPa), \quad \nu = 0.18, \quad f_t = 2.7\ (MPa), \quad G_f = 0.1\ (N/mm)$$

The thickness of the panel is *100mm* (*3.94 in*) and the value of β given in equation (2-23) is set to *1.5* in order to consider the effects of tangential displacement in cohesive law. Three dimensional linear tetrahedral elements are used to discretize the structure, as depicted in Fig 2-6. The loading is imposed incrementally and as the principal stress reaches f_t, the crack initiates and progressively grows as the load increases. By applying the strategy described in the previous section, a smooth crack path is obtained, as shown in Fig 2-7 which is similar to the results presented in [29]. In addition, the load displacement curve for the panel is compared here with the experimental data given in ref. [36]; clearly the results of simulations incorporating the proposed methodology are quite accurate.

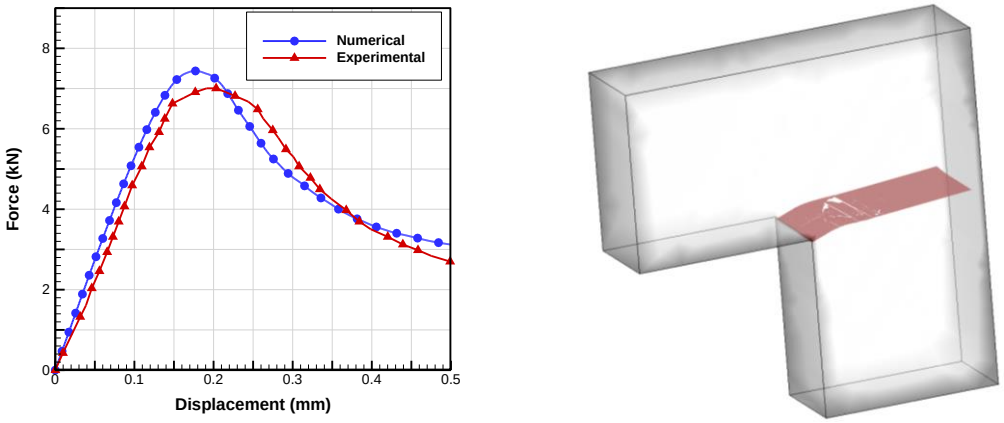

Fig 2-7 (Left) load-displacement curve; (Right) crack path (note 1kN = 224.8 lb)

2.7.2 Crack propagation in reinforced concrete beam

The next example studied here involves a reinforced concrete beam subjected to a three-point bending. This problem was studied experimentally by Bresler and Scordelis [37] using different ratios of reinforcements. The reinforcement is considered here in a discrete way using the standard Abaqus library. Fig 2-8 shows the geometry of the problem. Four longitudinal high strength steel bars#9 (#29 in metric unit) are placed within the concrete in two layers and the vertical load is applied incrementally to the top surface of the beam.

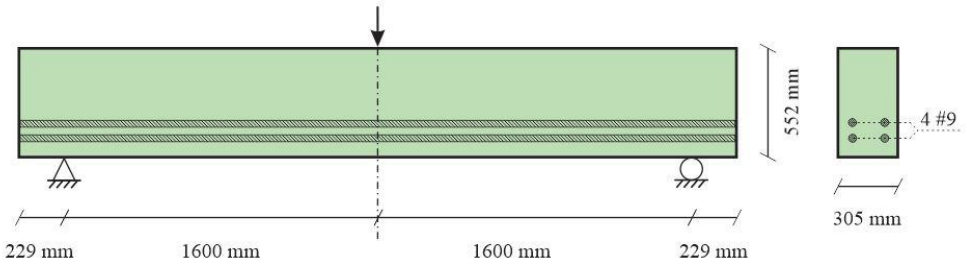

Fig 2-8- Geometry of simply supported reinforced concrete beam (note 1 m = 39.37 in)

The finite element discretization is provided in Fig 2-9 and the material properties of steel and concrete are given below.

Steel: $E_s = 200\,GPa, \quad \nu = 0.2, \quad f_y = 555\,MPa$

Concrete: $E_c = 23.8\,GPa, \quad \nu = 0.18, \quad f_t = 1.82\,MPa, \quad G = 0.1\,N/mm, \quad \beta = 0.1$

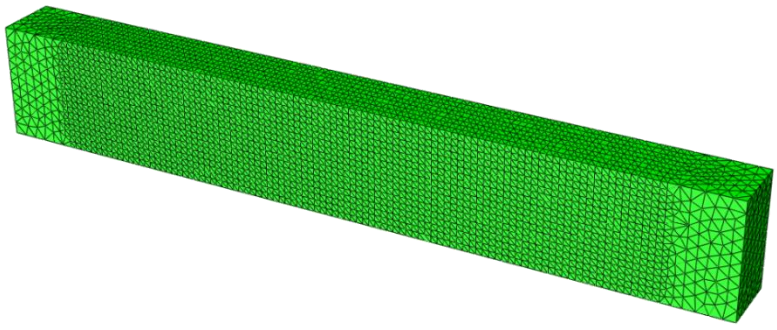

Fig 2-9- FE discretization by tetrahedron elements

As the load increases, the cracks initiate first at the mid-span of the beam as soon as the maximum principal stress reaches the strength of concrete. Due to the presence of reinforcement in the tensile region of the beam, the cracks cannot propagate further since the steel bars resist the crack opening. Consequently, other flexural cracks form at the bottom and propagate upwards as shown in Fig 2-10.

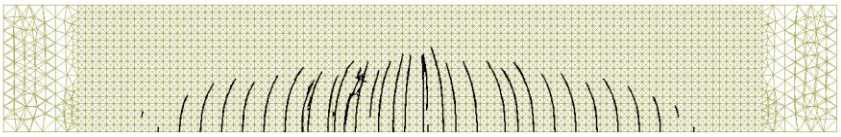

Fig 2-10- Crack path in beam after 2mm (0.08 in) deflection

In Fig 2-11, the load-displacement response for the beam is compared with the experimental data given in [37]. It is clear that the numerical results are fairly consistent here with the experimental evidence. Note that within the considered range of external load, the steel bars didn't reach the yield point, so that the mechanical characteristic remains stable.

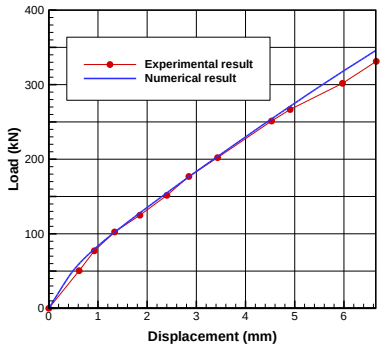

Fig 2-11- Load displacement curve for reinforced concrete beam (note 1kN = 224.8 lb)

2.7.3 ASR in reinforced concrete beam

In the last example dealing with the tensile fracture, the response of reinforced concrete beam subjected to ASR is examined. The experimental work has been conducted here by Swamy and Al-Asali [38] who investigated the chemical interaction for different percentage of fly ash in

concrete mixture. They tested three different sets of beams with different kinds of reactive aggregates. The beam was simply supported and its total length was *800 mm* (*31.5 in*). The geometry of the problem and position of longitudinal and shear reinforcement are given in Fig 2-12.

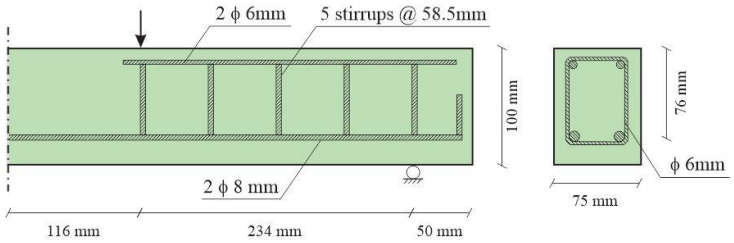

Fig 2-12- Geometry of problem (note 1 m = 39.37 in)

For this study one of the beams, referred to as "B3" in ref. [38], has been selected and the obtained results compared with the experiments. Material properties for concrete and reinforcement are summarized in the Table 2-1.

Table 2-1- Material properties of concrete and steel

Concrete modulus of elasticity	$E_c=30\ GPa$	Steel modulus of elasticity	$E_s=200\ GPa$
Concrete Poisson ratio	$\nu=0.18$	Steel Poisson ratio	$\nu=0.2$
Tensile strength of concrete	$f_t=1.8\ MPa$	Steel yield stress	$f_y=560\ MPa$
Concrete ASR constant	$A_1=20\ days$	Maximum free expansion	$\varepsilon_\infty=1\%$

(1 kPa = 0.14 psi)

The beam was placed in an environment of controlled humidity and temperature for two years. The deformation was measured in both the reinforcement and concrete at the set of selected points, as shown in Fig 2-13.

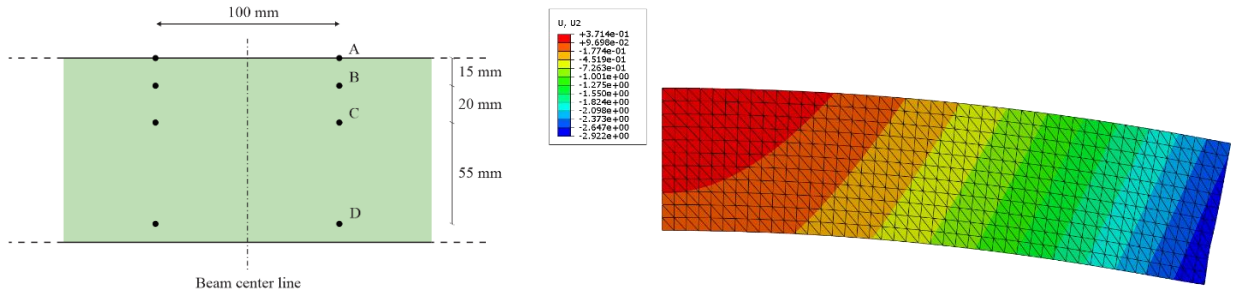

Fig 2-13- (left) Selected points for measuring strain in concrete; (right) Deformed concrete beam after 2 years of ASR

In the first stage of the test, i.e. in the two years' time interval, no external load was applied. Since the longitudinal reinforcement in the tensile region was more intense than that in the compressive zone, the beam has initially experienced an upward movement. In addition, as the compressive stress was increasing in the bottom layer, less chemical expansion occurred in the longitudinal direction, which lead to an increase in the curvature of beam. The final deformation after two years of progressive ASR is plotted in Fig 2-13. The numerical simulations give similar results to laboratory tests as the total hogging of beam is reported to be about 3 mm (0.12 in).

In Fig 2-14, the evolution of strain in the longitudinal tensile steel bar is plotted versus time. As it can be seen, during the first 100 days of continuing reaction the reinforcement elongates and then the expansion stops due to the generation of compressive stress in the bottom layer of the beam. The second plot in Fig 2-14 shows the variation of strain within the concrete during the first two years of the reaction. Again, the numerical results are quite consistent with the experimental data for all point at which the measurements were taken.

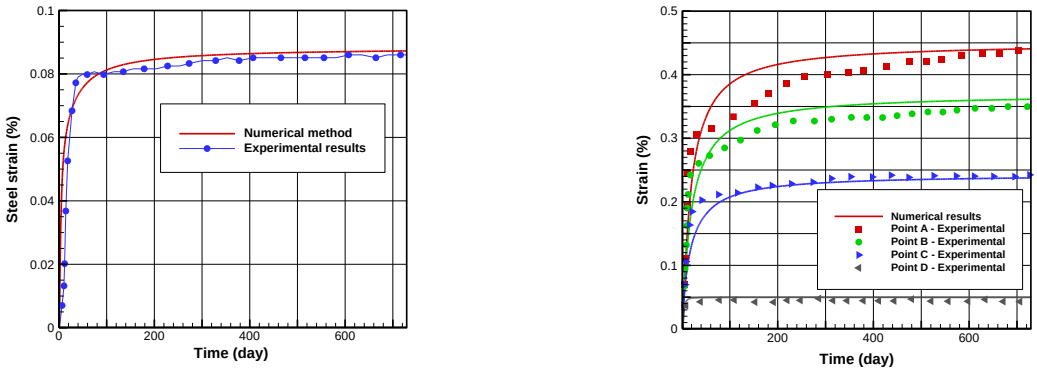

Fig 2-14- Strain variation in steel (left) and concrete (right) by time

The next stage of the experiment involved four-point bending of a beam affected by ASR as well as a beam without any reactive aggregate. The corresponding load-displacement curves are plotted in Fig 2-15. The results indicate that, although the reaction leads to a progressive degradation of concrete, the mechanical characteristics are not significantly affected, which is primarily due to the presence of reinforcement. The numerical predictions are fairly accurate in this respect as well. Finally, the predicted crack pattern is shown in Fig 2-15 and Fig 2-16. The most intense damage is in the tensile zone in the area adjacent to the reinforcement.

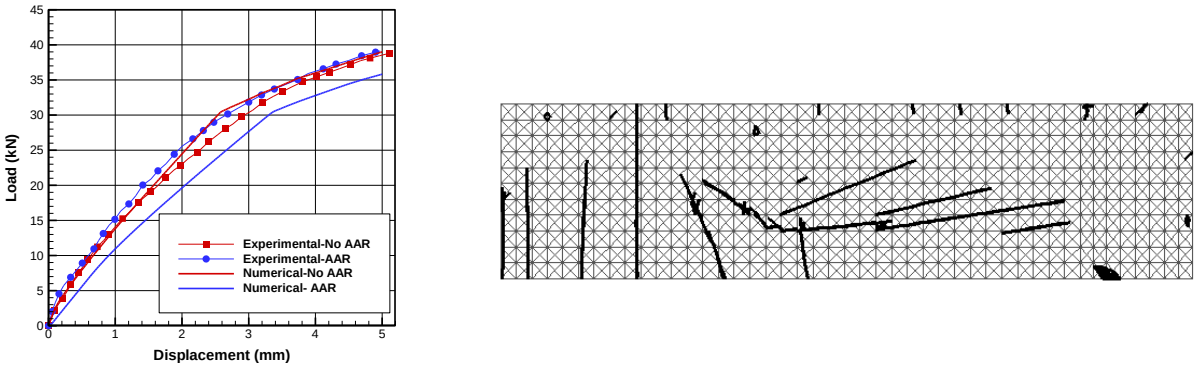

Fig 2-15- (left) Load vs displacement curve; (right) crack pattern after loading in 2D (note 1kN = 224.8 lb and 1 m = 39.37 in)

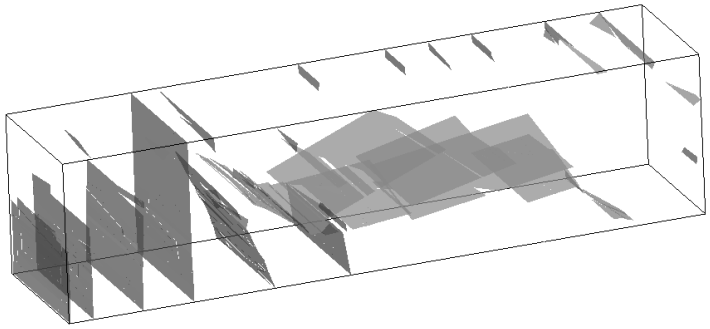

Fig 2-16- Crack pattern in 3D

2.8 Final remarks

In this work, the chemo-mechanical formulation for describing the damage propagation in concrete affected by ASR has been presented. Within this framework two key effects of the chemical interaction, i.e. expansion of silica gel and degradation of strength/stiffness properties of concrete,

were taken into account and an implicit algorithm has been presented for integration of the chemo-elastic constitutive relation.

The evolution of damage has been described using the concept of volume averaging, which discriminates between properties of the intact material and those of the interface and incorporates the characteristic length. The Rankine's criterion was used to define the onset of cracking. For tracing the crack path a general three dimensional algorithm has been developed by employing tetrahedral elements and assuming that the crack is represented by a planar discontinuity surface formed within each element. For macroscopic description of cohesive cracks, the traction-separation law was formulated using a decaying exponential function which attenuated traction on crack faces during an active loading process.

Three different numerical examples have been provided to illustrate the proposed methodology. The first two involved an L-shaped plain concrete panel and a reinforced concrete beam subjected to mechanical loads. For both these cases, the load-displacement characteristics and the fracture pattern were compared with the experimental data. The last example dealt with examining the effects of ASR in a reinforced concrete beam. Again, the results were compared with the experimental evidence and clearly demonstrated the predictive abilities of the outlined framework.

2.9 References

1. Bazant ZP, Zi G, Meyer C, "Fracture mechanics of ASR in concretes with waste glass particles of different sizes," *J Eng Mech-ASCE*, V. 126, No. 3, Mar. 2000, pp. 226-232.
2. Pan J, Feng Y, Wang J, Sun Q, Zhang C, Owen D, "Modeling of alkali-silica reaction in concrete: a review," *Frontiers of Structural and Civil Engineering*, V. 6, No. 1. 2012, pp. 1-18.
3. Berra M, Faggiani G, Mangialardi T, Paolini AE, "Influence of stress restraint on the expansive behaviour of concrete affected by alkali-silica reaction," *Cement and Concrete Research*, V. 40, No. 9, Sep. 2010, pp. 1403-1409.
4. Diamond S, Thaulow N, "A study of expansion due to alkali—silica reaction as conditioned by the grain size of the reactive aggregate," *Cement and Concrete Research*, V. 4, No. 4. 1974, pp. 591-607.
5. Multon S, Cyr M, Sellier A, Leklou N, Petit L, "Coupled effects of aggregate size and alkali content on ASR expansion," *Cement and Concrete Research*, V. 38, No. 3, Mar. 2008, pp. 350-359.

6. Pietruszczak S, "On the mechanical behaviour of concrete subjected to alkali-aggregate reaction," *Computers & Structures*, V. 58, No. 6, Mar 17. 1996, pp. 1093-1097.

7. Capra B, Bournazel J-P, "Modeling of induced mechanical effects of alkali-aggregate reactions," *Cement and Concrete Research*, V. 28, No. 2. 1998, pp. 251-260.

8. Ulm FJ, Coussy O, Li KF, Larive C, "Thermo-chemo-mechanics of ASR expansion in concrete structures," *J Eng Mech-ASCE*, V. 126, No. 3, Mar. 2000, pp. 233-242.

9. Saouma V, Perotti L, "Constitutive model for alkali-aggregate reactions," *ACI Materials Journal*, V. 103, No. 3, May-Jun. 2006, pp. 194-202.

10. Bazant ZP, Steffens A, "Mathematical model for kinetics of alkali–silica reaction in concrete," *Cement and Concrete Research*, V. 30, No. 3. 2000, pp. 419-428.

11. Sellier A, Bourdarot E, Multon S, Cyr M, Grimal E, "Combination of Structural Monitoring and Laboratory Tests for Assessment of Alkali-Aggregate Reaction Swelling: Application to Gate Structure Dam," *ACI Materials Journal*, V. 106, No. 3, May-Jun. 2009, pp. 281-290.

12. Hillerborg A, Modéer M, Petersson P-E, "Analysis of crack formation and crack growth in concrete by means of fracture mechanics and finite elements," *Cement and concrete research*, V. 6, No. 6. 1976, pp. 773-781.

13. Devloo P, "A three-dimensional adaptive finite element strategy," *Computers & Structures*, V. 38, No. 2. 1991, pp. 121-130.

14. Belytschko T, Tabbara M, "H-Adaptive Finite-Element Methods for Dynamic Problems, with Emphasis on Localization," *International Journal for Numerical Methods in Engineering*, V. 36, No. 24, Dec 30. 1993, pp. 4245-4265.

15. Zienkiewicz OC, Huang MS, Pastor M, "Localization Problems in Plasticity Using Finite-Elements with Adaptive Remeshing," *International Journal for Numerical and Analytical Methods in Geomechanics*, V. 19, No. 2, Feb. 1995, pp. 127-148.

16. Oliver J, "Modelling strong discontinuities in solid mechanics via strain softening constitutive equations. Part 1: Fundamentals," *International Journal for Numerical Methods in Engineering*, V. 39, No. 21. 1996, pp. 3575-3600.

17. Simo JC, Oliver J, Armero F, "An analysis of strong discontinuities induced by strain-softening in rate-independent inelastic solids," *Computational Mechanics*, V. 12, No. 5. 1993, pp. 277-296.

18. Sancho JM, Planas J, Cendon DA, Reyes E, Galvez JC, "An embedded crack model for finite element analysis of concrete fracture," *Engineering Fracture Mechanics*, V. 74, No. 1-2, Jan. 2007, pp. 75-86.

19. Moës N, Dolbow J, Belytschko T, "A finite element method for crack growth without remeshing," *International Journal for Numerical Methods in Engineering*, V. 46, No. 1, Sep 10. 1999, pp. 131-150.

20. Moës N, Belytschko T, "Extended finite element method for cohesive crack growth," *Engineering fracture mechanics*, V. 69, No. 7. 2002, pp. 813-833.

21. Sukumar N, Moes N, Moran B, Belytschko T, "Extended finite element method for three-dimensional crack modelling," *International Journal for Numerical Methods in Engineering*, V. 48, No. 11, Aug 20. 2000, pp. 1549-1570.

22. Pietruszczak S, Mroz Z, "Finite-Element Analysis of Deformation of Strain-Softening Materials," *International Journal for Numerical Methods in Engineering*, V. 17, No. 3. 1981, pp. 327-334.

23. Pietruszczak S, "On homogeneous and localized deformation in water-infiltrated soils," *International Journal of Damage Mechanics*, V. 8, No. 3. 1999, pp. 233-253.

24. Haghighat E, Pietruszczak S, "On modeling of discrete propagation of localized damage in cohesive-frictional materials," *International Journal for Numerical and Analytical Methods in Geomechanics*, V. 39, No. 16. 2015, pp. 1774-1790.

25. Pietruszczak S, Ushaksaraei R, Gocevski V, "Modelling of the effects of alkali-aggregate reaction in reinforced concrete structures," *Computers and Concrete*, V. 12, No. 5. 2013, pp. 627-650.

26. Larive C, "Apports combinés de l'expérimentation et de la modélisation á la comprehension de l'alcali reaction et de ses effets mécaniques.," Labratorie Central des Ponts et Chaousses (LCPC), Paris, France, 1998.

27. Léger P, Cote P, Tinawi R, "Finite element analysis of concrete swelling due to alkali-aggregate reactions in dams," *Computers & structures*, V. 60, No. 4. 1996, pp. 601-611.

28. Zhang HW, Zhou L, "Implicit integration of a chemo-plastic constitutive model for partially saturated soils," International Journal for Numerical and Analytical Methods in Geomechanics, V. 32, No. 14, Oct 10. 2008, pp. 1715-1735.

29. Dumstorff P, Meschke G, "Crack propagation criteria in the framework of X-FEM-based structural analyses," *International Journal for Numerical and Analytical Methods in Geomechanics*, V. 31, No. 2. 2007, pp. 239-259.

30. Mariani S, Perego U, "Extended finite element method for quasi-brittle fracture," *International Journal for Numerical Methods in Engineering*, V. 58, No. 1. 2003, pp. 103-126.

31. Wells GN, Sluys LJ, "A new method for modelling cohesive cracks using finite elements," *International Journal for Numerical Methods in Engineering*, V. 50, No. 12, Apr 30. 2001, pp. 2667-2682.

32. Jäger P, Steinmann P, Kuhl E, "Modeling three-dimensional crack propagation—A comparison of crack path tracking strategies," *International Journal for Numerical Methods in Engineering*, V. 76, No. 9. 2008, pp. 1328-1352.

33. Manzoli OL, Shing PB, "A general technique to embed non-uniform discontinuities into standard solid finite elements," *Computers & Structures*, V. 84, No. 10-11, Apr. 2006, pp. 742-757.

34. Linder C, Armero F, "Finite elements with embedded strong discontinuities for the modeling of failure in solids," *International Journal for Numerical Methods in Engineering*, V. 72, No. 12, Dec 17. 2007, pp. 1391-1433.

35. Gasser TC, Holzapfel GA, "3d crack propagation in unreinforced concrete.: A two-step algorithm for tracking 3d crack paths," *Computer Methods in Applied Mechanics and Engineering*, V. 195, No. 37. 2006, pp. 5198-5219.

36. Winkler B, Hofstetter G, Niederwanger G, "Experimental verification of a constitutive model for concrete cracking," Proceedings of the Institution of Mechanical Engineers, Part I: *Journal of Materials Design and Applications*, V. 215, No. 2. 2001, pp. 75-86.

37. Bresler B, Scordelis AC, "Shear strength of reinforced concrete beams," *ACI Journal Proceedings*, V. 60, No. 1. 1963.

38. Swamy RN, Al-Asali M, "Control of alkali-silica reaction in reinforced concrete beams," *ACI Materials Journal*, V. 87, No. 1. 1990.

3 Deterministic size effect in concrete structures with account for chemo-mechanical loading

3.1 Contribution

In this article the size effect phenomenon in concrete structures is investigated by employing the volume averaging methodology in three-dimensional domain. The mathematical formulation of chemo-plasticity framework is presented in detail and it is incorporated in an implicit scheme to update the stress state and tangential stiffness. The structure of the derived constitutive relations is such that they employ a superposition of two terms, the first representing an instantaneous mechanical response, which is rate-independent, and the second related to time-dependent effects of chemical interaction. The onset of localization is examined in both tension and compression regime. It is shown that the inception of strain localization due to ASR alone is possible with its rate controlled by the kinetics of chemical reaction. On the other hand, the instantaneous mode occurs when the bifurcation condition, associated with singularity of the acoustic tensor, is satisfied. A number of numerical simulations have been carried out. The first set deals with a deterministic assessment of the size effect in a series of three-point bending tests as well as compression tests. For continuing ASR, it is shown that, by increasing the size of the structure, a loss of stability may occur under a sustained load. The analysis clearly demonstrates that the size effect is primarily the result of localized damage that accompanies the structural failure. Therefore, an adequate description of this process, which employs physically identifiable parameters and a uniquely defied ‘characteristic dimension’, is of a significant importance.

Deterministic size effect in concrete structures with account for chemo-mechanical loading

S. Moallemi[1], S. Pietruszczak[1], Z. Mróz [2]

[1]*Department of Civil Engineering, McMaster University, Hamilton, Ontario, Canada*

[2]*Institute of Fundamental Technological Research, Polish Academy of Sciences, Warsaw, Poland*

3.2 Abstract

The work presented here is focused on examining the size effect in concrete structures subjected to different loading conditions, which include a chemo-mechanical interaction. The study involves extensive three dimensional finite element simulations, which incorporate a constitutive law with embedded discontinuity for tracing the propagation of damage pattern. The analysis deals with various mechanical scenarios that incorporate both a cohesive and frictional damage mechanism, as well as the effects of degradation of concrete triggered by continuing alkali-silica reaction (ASR). In the latter case, a chemo-plasticity framework is employed. The first set of simulations provides a deterministic assessment of the size effect in a series of three-point bending tests as well as compression tests. For continuing ASR, it is demonstrated that, by increasing the size of the structure, a spontaneous failure may occur under a sustained load. The numerical examples given here clearly show that the size effect is associated with propagation of localized damage whose rate is controlled by a suitably defined 'characteristic length'.

Keywords: size effect; alkali-silica reaction; 3D crack propagation; embedded discontinuity model; bifurcation analysis.

3.3 Introduction

The term ‘size effect’ refers to variation of the nominal strength with size in geometrically similar structures. In general, for the quasi-brittle materials, such as concrete and/or rocks, it has been shown that the ultimate strength of a structure is significantly reduced by increasing its size [1]. In addition, in small structures the response is more ductile than in larger ones. The brittleness is not only affected by the size, but also the actual geometry of the structure, the presence of pre-existing fractures (e.g., notches) and the fracture energy that controls the stress redistribution.

The size effect has been documented experimentally as early as 1921 in the work of Griffith [2] which dealt with assessment of nominal strength of glass fibers. Soon after, the statistical theories began to emerge, which attributed the size effect to the randomness of material strength within the considered domain [3-5]. This approach was dominant until mid-1970s when the deterministic frameworks started to appear. It was then demonstrated that the major cause of the size effect is the stable propagation of damage. A historical overview of different theories is provided, for example, by Bazant and Planas in their monograph.[6]. Most of the research has been conducted in relation to quasi-brittle materials, in particular on concrete subjected to tensile damage. Two types of structures were examined, i.e. with and without a pre-existing fracture, such as an initial notch [6]. Several noteworthy studies in this respect have been conducted by Bazant and his co-workers who developed a general energetic-statistical size effect theory for concrete structures [5-8]. The size effect phenomenon is not limited to tensile regime. Cusatis and Bazant [9], for example, investigated the behavior of concrete columns with and without notch under compression; however, in this case the variation of nominal strength with the size of the structure was not very significant. In addition, a number of experimental studies have been performed on the evaluation of size effect in reinforced concrete structures [10, 11].

One of the important loading scenarios that has not been considered so far in the assessment of size effect, is the degradation of concrete triggered by chemo-mechanical interaction. An example here is the alkali-silica reaction (ASR). This reaction occurs in concrete structures which are exposed to high humidity environment, such as dams, piers and bridges. The thermodynamic aspects dealing with the chemical sequence and the rate of kinetics of ASR have been discussed, for example, in refs.[12, 13]. At the same time, the effects of chemo-mechanical interaction have

also been extensively studied, both experimentally [14] and numerically at a meso as well as macroscale [13,15-17]. The primary objective of this work is to examine the size effect in a broad range of loading conditions that also include damage due to continuing ASR. It is clearly demonstrated that the size effect is associated with formation of discrete macrocrcaks and that the mathematical description of propagation process requires the notion of a 'characteristic length'. It is noted that this parameter was employed in the past research, but its definition remains rather ambiguous. In different works, it was loosely interpreted as the 'size of material inhomogeneities' or that of 'the fracture process zone'; i.e. no precise quantitative meaning was assigned. Here, following earlier work reported in refs. [18-20], the propagation of damage is described in terms of an embedded discontinuity approach, which incorporates volume averaging in order to generate representative homogenized stiffness moduli. In this approach the characteristic dimension is explicitly defined as the ratio of the area of macrocrack to the selected reference volume, the latter identified with that of a finite element containing the discontinuity. Thus, for a fixed FE mesh, if the size of the structure increases, the 'characteristic length' within the elements containing discontinuity changes, which in turn affects the rate of damage propagation and, thus, the nominal strength of the structure.

The outline of this paper is as follows. In the next section, a brief overview of the notion of deterministic size effects is provided. Later, the mathematical formulation of the problem is outlined. This includes the description of both homogeneous and localized deformation, the latter associated with the presence of discrete macrocracks. In the follow up section, the results of numerical simulations are presented. Those comprise a deterministic assessment of the size effect in a series of three-point bending tests as well as compression tests. For continuing ASR, it is demonstrated that, by increasing the size of the structure, a spontaneous failure can occur under a sustained load below the nominal failure value.

3.4 Size effect in concrete

The existing analytical expressions which quantify the deterministic size effect have been developed for quasi-brittle materials [21, 22]. They deal with geometrically similar structures, with

or without large pre-existing fractures/notches, and provide an assessment of nominal strength as a function of the characteristic size of the structure. The most commonly used formulae are those developed by Bazant and co-workers (cf. ref. [6]) based on their extensive research on this topic. In general, the nominal strength is said to be bound for small sizes by the plasticity limit, whereas for large sizes by the approximation based on linear elastic fracture mechanics. The proposed analytical expressions take the form

$$\sigma_N = \begin{cases} f_r^{\infty}\left(1 + r\dfrac{D_b}{D + l_p}\right)^{1/r} & \text{Type 1 (un-notched structure)} \\ \dfrac{B\, f_t}{\sqrt{1 + \dfrac{D}{D_b}}} & \text{Type 2 (notched structure)} \end{cases} \tag{3-1}$$

Here, σ_N is the nominal strength, D is the characteristic dimension of the structure, while f_r^{∞} represents the strength corresponding to elastic-brittle material for the case when $D \to \infty$. The remaining constants are largely semi-empirical. The parameters r and l_p control the curvature of the plot and the transition to perfectly plastic response (for $D \to 0$), respectively, while D_b is said to be a 'characteristic length' associated with the thickness of the fracture zone. In the second equation, f_t denotes the tensile strength and B is, again, a geometry-dependent empirical parameter. A schematic representation of these two size effect laws in an affined logarithmic space is depicted in Fig 3-1.

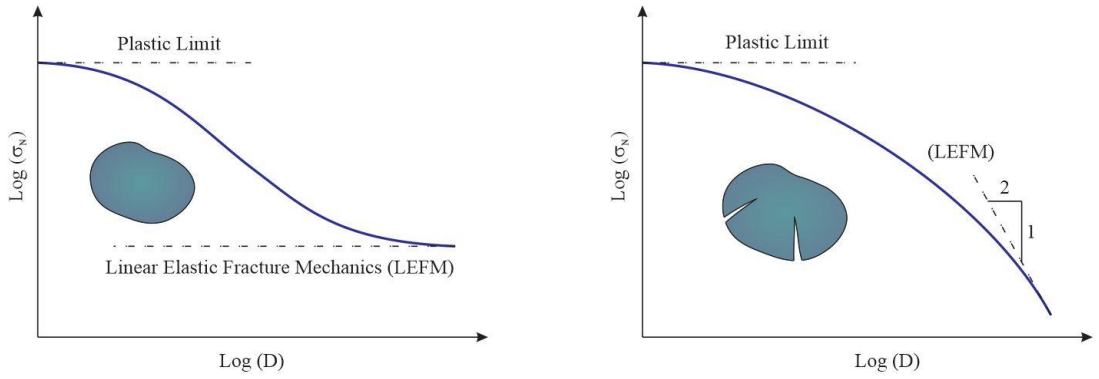

Fig 3-1- Size effect law for (a) un-notched structure and (b) structure with initial crack(s)

It appears that the practical applicability of the existing analytical approximations, such as eq.(3-1), is rather limited. Firstly, several of the parameters employed are semi-empirical and there is no systematic procedure for their identification. Even the notion of the 'characteristic length' has a certain degree of ambiguity as it is not precisely defined. Furthermore, the nominal strength of a structure is affected by its geometry, boundary conditions and the strength/deformation properties of the material. Thus, even for simple geometrically similar structures, the last two features may quite significantly impact the strength. Besides, the assessment of maximum nominal strength, which is identified with plastic limit, is questionable, as evidenced by examples provided later in this paper. Also, for very small sizes (i.e. $D \to 0$), the use of a continuum formulation is rather obscure as the concept of REV is no longer applicable. Therefore, it does not seem feasible to establish a unique analytical 'size effect formula' with reliable predictive abilities. To compound the problem, the extrapolation from the existing formulae to more complex geometries than those employed in their development and/or to structures with no geometric similarities is even more problematic.

Given the comments above, it seems that the most reliable approach is an adequate experimental and/or numerical assessment. In fact, the design of complex engineering structures (dams, bridges, powerhouses, etc.) usually requires a numerical analysis. In this case, the notion of size effect is naturally addressed within the analysis itself (i.e., the problem employs the actual geometry and boundary conditions), provided that an adequate procedure for describing the damage propagation is employed. In what follows, the mathematical framework implemented in this work is briefly outlined. Later, the results of numerical simulations are presented addressing a broad range of loading conditions and their impact on ultimate strength in relation to the size of the structure.

3.5 Mathematical formulation

3.5.1 Constitutive relations governing homogeneous deformation in the presence of ASR

The description of chemo-mechanical interaction incorporates a scalar parameter ζ which is a measure of the continuing reaction [17]. In general, the kinetics of the reaction depends on the

available alkali content, the humidity (the onset occurs when it exceeds 80%) as well as the temperature. The evolution law may be assumed in a linear form

$$\dot{\zeta} = \gamma(\bar{\zeta} - \zeta) \quad \Rightarrow \quad \zeta = \bar{\zeta}(1 - e^{-\gamma\langle t - t_0\rangle}) \tag{3-2}$$

where $\bar{\zeta}$ can be interpreted as a value of the state variable ζ associated with the chemical equilibrium and γ is a material constant describing rate of the reaction (the latter depends also, among others, on the reactive particle size). In the integrated form of eq.(3-2), the constant t_0 is the initiation time, while <…> are Macauley brackets. Note that the linear form of the kinetic law has a simple interpretation, i.e. the reaction rate $\dot{\zeta}$ is controlled by the amount of chemical components which can still react, the latter being proportional to $(\bar{\zeta} - \zeta)$. The parameter $\bar{\zeta}$ depends, in general, on the temperature and relative humidity, it may also be affected by the confining pressure. Note that the value of $\bar{\zeta}$ is defined within the range $\bar{\zeta} \subseteq [0,1)$ so that $\zeta \subseteq [0, \bar{\zeta})$. An extensive discussion on the kinetics of ASR is provided, for example, in refs. [13, 23]. The primary mechanical effects of the reaction involve a progressive volumetric expansion and a continuing degradation of strength/deformation properties of the material. For a given alkali content, the expansion in the stress-free state may be defined as

$$\boldsymbol{\varepsilon}^c = \frac{1}{3} \in (t)\mathbf{I}, \qquad \in (t) = \zeta\, \varepsilon_\infty \tag{3-3}$$

where ε_∞ is the maximum free expansion in the course of ASR and $\mathbf{I}$ is the identity tensor.

The specification of the constitutive relation follows now the general framework of chemo-plasticity. In the elasto-plastic regime, the formulation for plain concrete is similar to that employed in ref. [24]. The approach invokes a non-associated flow rule and the yield surface is expressed in a functional form

$$f = \bar{\sigma} - \eta(\bar{\varepsilon})\, g(\theta)\, \bar{\sigma}_c = 0; \qquad \bar{\sigma}_c = \frac{-c_1 + \sqrt{(c_1^2 + 4c_2\,(c_3 + I/f_{co}))}}{2c_2} \quad f_{co} \tag{3-4}$$

In the equations above, I is the first stress invariant, $\bar{\sigma}=(J_2)^{1/2}$, $\theta=\frac{1}{3}\sin^{-1}(3\sqrt{3}\,J_3/2\bar{\sigma}^3)$, where (J_2, J_3) are the basic invariants of the stress deviator and θ is the Lode angle. Moreover, f_{co} is the uniaxial compressive strength prior to the onset of ASR, c's are strength parameters that depend on ζ, $\eta\subset\langle 0,1)$ represents a hardening function and the internal variable $\bar{\varepsilon}$ is a hardening parameter that is identified with accumulated plastic distortion. The plastic potential surface is taken in the form

$$Q=\bar{\sigma}+\mu_c g(\theta)\bar{I}\ln(\bar{I}/\bar{I}_0)=0 \tag{3-5}$$

where $\bar{I}=c_3 f_{co}+I$, $\bar{I}_0$ is defined from the condition Q=0, and μ_c represents the value of $\mu=\bar{\sigma}/g(\theta)\bar{I}$ for which a transition from plastic compaction to dilatancy occurs. Note that $Q=Q(\boldsymbol{\sigma},\zeta)$, which is the result of the dependence of parameters c on ζ.

The continuing alkali reaction triggers a progressive degradation of mechanical properties. The primary material parameters affected by the reaction are the Young's modulus (E), and the strengths parameters c, eq.(4). The degradation laws are defined by invoking simple approximations

$$c_1=c_{10}(1-G_1\zeta);\quad c_2=c_{20}(1-G_2\zeta);\quad c_3=c_{30}(1-G_3\zeta);\quad E=E_0(1-G_4\zeta) \tag{3-6}$$

in which G's are material constants. The subscript '0' refers here to properties prior to the onset of the reaction, while the final values, for $\zeta\to 1$, correspond to the case when the reaction is complete.

In order to derive the constitutive relation, consider first the response in the *elastic* range. In the presence of continuing reaction, the total strain may be expressed as the sum of elastic and chemical components, eq.(3-3), so that

$$\boldsymbol{\varepsilon}=\boldsymbol{\varepsilon}^e+\boldsymbol{\varepsilon}^c=\mathbb{C}^e:\boldsymbol{\sigma}+\frac{1}{3}\zeta\,\varepsilon_\infty\,\mathbf{I} \tag{3-7}$$

where $\mathbb{C}^e$ is the elastic compliance tensor. The extension of the above relation to the *elastoplastic* range can be obtained by invoking the additivity of elastic and plastic strain rates. Noting the dependence of elastic properties on ζ, one has

$$\dot{\boldsymbol{\varepsilon}} = \dot{\boldsymbol{\varepsilon}}^e + \dot{\boldsymbol{\varepsilon}}^p + \dot{\boldsymbol{\varepsilon}}^c = \mathbb{C}^e : \dot{\boldsymbol{\sigma}} + \dot{\boldsymbol{\varepsilon}}^p + \mathbf{b}\dot{\zeta} \; ; \quad \mathbf{b} = \left[\frac{1}{3}\varepsilon_\infty \mathbf{I} + \partial_\zeta \mathbb{C}^e : \boldsymbol{\sigma} \right]; \quad \dot{\boldsymbol{\varepsilon}}^p = \dot{\lambda}\frac{\partial Q}{\partial \boldsymbol{\sigma}} \tag{3-8}$$

The inverse relation, which is required for numerical implementation, can be obtained by multiplying both sides of eq.(3-8) by $\mathbb{D}^{\mathrm{e}} = \left[\mathbb{C}^e \right]^{-1}$, so that for an active loading process there is

$$\dot{\boldsymbol{\sigma}} = \mathbb{D}^{\mathrm{e}} : (\dot{\boldsymbol{\varepsilon}} - \dot{\boldsymbol{\varepsilon}}^p - \mathbf{b}\dot{\zeta}) \tag{3-9}$$

In order to specify the plastic strain rates, the standard plasticity procedure is now followed. Writing the consistency condition as

$$\dot{f}(\boldsymbol{\sigma}, \bar{\varepsilon}, \zeta) = \frac{\partial f}{\partial \boldsymbol{\sigma}} : \dot{\boldsymbol{\sigma}} + \frac{\partial f}{\partial \bar{\varepsilon}}\dot{\bar{\varepsilon}} + \frac{\partial f}{\partial \zeta}\dot{\zeta} = 0 \tag{3-10}$$

and noting that $\dot{\bar{\varepsilon}} = \left[dev(\dot{\boldsymbol{\varepsilon}}^p) : dev(\dot{\boldsymbol{\varepsilon}}^p) \right]^{1/2}$, where *dev* refers to deviatoric part of the operator, the plastic multiplier can be defined as

$$\dot{\lambda} = \frac{1}{H}\left\{ \frac{\partial f}{\partial \boldsymbol{\sigma}} : \mathbb{D}^{\mathrm{e}} : \dot{\boldsymbol{\varepsilon}} - \left(\frac{\partial f}{\partial \boldsymbol{\sigma}} : \mathbb{D}^{\mathrm{e}} : \mathbf{b} - \frac{\partial f}{\partial \zeta} \right)\dot{\zeta} \right\} = \frac{1}{H_p}\left(\frac{\partial f}{\partial \boldsymbol{\sigma}} \cdot \dot{\boldsymbol{\sigma}} + \frac{\partial f}{\partial \zeta}\dot{\zeta} \right) \tag{3-11}$$

where

$$H = H_e + H_p \; ; \qquad H_e = \frac{\partial f}{\partial \boldsymbol{\sigma}} : \mathbb{D}^{\mathrm{e}} : \frac{\partial Q}{\partial \boldsymbol{\sigma}} \; ; \qquad H_p = -\frac{\partial f}{\partial \bar{\varepsilon}}\left[dev\left(\frac{\partial Q}{\partial \boldsymbol{\sigma}} \right) : dev\left(\frac{\partial Q}{\partial \boldsymbol{\sigma}} \right) \right]^{1/2} \tag{3-12}$$

During the plastic deformation process, the Kuhn-Tucker loading-unloading conditions can be stated as $\dot{\lambda} \geq 0, \, f \leq 0, \dot{\lambda} f = 0$. Note that within the considered deviatoric hardening framework, the homogeneous deformation is associated with $H_p \geq 0$, while $\partial f / \partial \zeta \geq 0$ corresponds to a softening chemical action. Thus, an active loading process should satisfy the inequality

$$\frac{\partial f}{\partial \boldsymbol{\sigma}} \cdot \dot{\boldsymbol{\sigma}} + \frac{\partial f}{\partial \zeta} \dot{\zeta} \geq 0 \qquad or \qquad -\left|\frac{\partial f}{\partial \boldsymbol{\sigma}}\right| |\dot{\boldsymbol{\sigma}}| \cos\alpha \geq -\frac{\partial f}{\partial \zeta} \dot{\zeta} \tag{3-13}$$

where α is the angle between the vectors $\dot{\boldsymbol{\sigma}}$ and $-\frac{\partial f}{\partial \boldsymbol{\sigma}}$. Hence, if the stress rate vector is directed towards the interior of the yield surface, an active elastoplastic process can occur provided $\dot{\boldsymbol{\sigma}}$ lies in the exterior of the conical domain whose size depends on the ratio $\dot{\zeta} / |\dot{\boldsymbol{\sigma}}|$, i.e.

$$\alpha \geq \cos^{-1} \frac{\partial f / \partial \zeta}{|\partial f / \partial \boldsymbol{\sigma}|} \frac{\dot{\zeta}}{|\dot{\boldsymbol{\sigma}}|} \tag{3-14}$$

Apparently, when $\dot{\zeta} / |\dot{\boldsymbol{\sigma}}| \to 0$, the classical loading condition $\alpha \geq \pi / 2$ is recovered. In general, however, the loading-unloading criterion is affected by both the rate of ASR (or any other transient process) and the induced stress rate. Similar conclusion can be reached for a strain controlled deformation process.

Substituting now eq. (3-11) into (3-9) one can obtain, after some algebraic transformations, the following general form of the constitutive relation

$$\dot{\boldsymbol{\sigma}} = \mathbb{D}_{\mathrm{T}} : \dot{\boldsymbol{\varepsilon}} - \mathbf{D}_{\mathbf{c}} \dot{\zeta} \tag{3-15}$$

where $\mathbb{D}_{\mathrm{T}}$ and $\mathbf{D}_{\mathbf{c}}$ are the tangential stiffness operators related to mechanical and chemical components, respectively:

$$\mathbb{D}_{\mathrm{T}} = \mathbb{D}^{\mathrm{e}} - \frac{1}{H}\left[\mathbb{D}^{\mathrm{e}} : \left(\frac{\partial Q}{\partial \boldsymbol{\sigma}} \otimes \frac{\partial f}{\partial \boldsymbol{\sigma}}\right) : \mathbb{D}^{\mathrm{e}}\right]; \qquad \mathbf{D}_{\mathbf{c}} = \mathbb{D}_{\mathrm{T}} : \left(\mathbf{b} + \frac{1}{H}\frac{\partial f}{\partial \zeta}\frac{\partial Q}{\partial \boldsymbol{\sigma}}\right) \tag{3-16}$$

In order to update the stress state an implicit backward Euler integration scheme is employed, according to which the stress increment at each time step Δt is defined by $\Delta\boldsymbol{\sigma} = \dot{\boldsymbol{\sigma}}_{t+\Delta t} \Delta t$. Substituting the second equation in (3-8) into eq. (3-9) and expressing the result in incremental form, one obtains

$$\boldsymbol{\sigma}_{t+\Delta t} = \mathbb{Q}^{-1} : \left[\boldsymbol{\sigma}_t + \mathbb{D}^e : \left(\Delta\boldsymbol{\varepsilon} - \Delta\boldsymbol{\varepsilon}^p\right) - \left(\frac{1}{3}\varepsilon_\infty \mathbb{D}^e : \mathbf{I}\right)\Delta\zeta\right], \qquad \mathbb{Q} = \mathbb{I} + \mathbb{D}^e : \partial_\zeta \mathbb{C}^e \Delta\zeta \tag{3-17}$$

where $\mathbb{I}$ is the fourth order identity tensor and $\boldsymbol{\sigma}_t$ is the stress state at the beginning of the increment. For an active loading process, the consistency condition given by eq. (3-10) should be satisfied. Here, the return mapping algorithm incorporating the elastic predictor–plastic corrector strategy is employed. The iterative scheme starts with evaluation of the trial stress increment that is based on the elastic approximation, i.e.

$$\Delta\boldsymbol{\sigma}^{\text{trial}} = \mathbb{Q}^{-1} : \left[\boldsymbol{\sigma}_t + \mathbb{D}^e : (\Delta\boldsymbol{\varepsilon}) - \left(\frac{1}{3}\varepsilon_\infty \mathbb{D}^e : \mathbf{I} \right) \Delta\zeta \right] - \boldsymbol{\sigma}_t \tag{3-18}$$

To obtain the plastic strain increment, the Taylor expansion is employed to enforce the consistency condition at time $t+\Delta t$, viz.

$$f^k + \frac{\partial f}{\partial \boldsymbol{\sigma}^k} : \boldsymbol{\delta\sigma}^k + \frac{\partial f}{\partial \bar{\varepsilon}^k}\delta\bar{\varepsilon}^k = 0 \tag{3-19}$$

where, $\delta\boldsymbol{\sigma}^k$ and $\delta\bar{\varepsilon}^k$ are the corrections for stress and hardening parameter at iteration k which are associated with plastic deformation. Invoking the definition of $\dot{\bar{\varepsilon}}$, one can write

$$f^k - \delta\lambda^k \frac{\partial f}{\partial \boldsymbol{\sigma}^k} : \mathbb{Q}^{-1} : \mathbb{D}^e : \frac{\partial Q}{\partial \boldsymbol{\sigma}^k} + \delta\lambda^k \frac{\partial f}{\partial \bar{\varepsilon}^k} \left\{ \text{dev}\left(\frac{\partial Q}{\partial \boldsymbol{\sigma}^k} \right) : \text{dev}\left(\frac{\partial Q}{\partial \boldsymbol{\sigma}^k} \right) \right\}^{1/2} = 0 \tag{3-20}$$

Solving this scalar equation, the variation of plastic multiplier $\delta\lambda^k$ can be determined as

$$\delta\lambda^k = \frac{f^k}{\dfrac{\partial f}{\partial \boldsymbol{\sigma}} : \mathbb{Q}^{-1} : \mathbb{D}^e : \dfrac{\partial Q}{\partial \boldsymbol{\sigma}} + H_p} \tag{3-21}$$

where H_p is defined in (3-12). At the end of the correction stage, the stress state and the plastic multiplier are updated, i.e.

$$\Delta\boldsymbol{\sigma}^{k+1} = \Delta\boldsymbol{\sigma}^k + \boldsymbol{\delta\sigma}^k ; \quad \Delta\lambda^{k+1} = \Delta\lambda^k + \delta\lambda^k \tag{3-22}$$

The iterations continue for subsequent correction steps until $f \to 0$.

3.5.2 Description of localized deformation

The constitutive law incorporating the yield function (3-4) describes, in general, a homogenous deformation mode, i.e. it remains valid as long as there is no localized damage. In the tensile regime, the onset of localization is assumed to be governed by the maximum tensile stress criterion. Thus, the macrocrack forms when $\sigma_1 = f_t$, where f_t is the tensile strength, and the direction of the crack is said to be orthogonal to that of the major principal stress. In the compression regime, the transition to localized deformation is assessed based on the bifurcation criterion of Rice and Rudnicki [25]. Thus, the onset of frictional damage occurs when the acoustic tensor satisfies the following condition

$$\det(\mathbf{Q}) = 0 \ , \ \mathbf{Q} = \mathbf{n} \cdot \mathbb{D}_{\mathrm{T}} \cdot \mathbf{n} \tag{3-23}$$

where $\mathbb{D}_{\mathrm{T}}$ is defined in eq. (3-16) and $\mathbf{n}$ denotes the orientation of the localized fracture.

It should be noted that in case of a chemical interaction, the constitutive relation (3-15) can also result in the onset of localized deformation mode starting from a material imperfection. Assume that the localized mode involves generation of a velocity discontinuity $\dot{\boldsymbol{w}}$, such that $\nabla \dot{\mathbf{u}} = \dot{\boldsymbol{w}} \otimes \mathbf{n}$, along a surface with unit normal $\mathbf{n}$. For such a mode, the rate of reaction inside the localization band vanishes. The equilibrium condition requires now that $\mathbf{n} \cdot \dot{\boldsymbol{\sigma}}$ remains continuous across the discontinuity surface. For the constitutive relation (3-15), the homogeneous stress rate outside the band $\dot{\boldsymbol{\sigma}}^0$ and that inside the band can be expresses in the form

$$\dot{\boldsymbol{\sigma}}^0 = \mathbb{D}_{\mathrm{T}}^0 : \dot{\boldsymbol{\varepsilon}}^0 - \mathbf{D}_{\mathbf{c}} \dot{\zeta}; \quad \dot{\boldsymbol{\sigma}} = \mathbb{D}_{\mathrm{T}} : \dot{\boldsymbol{\varepsilon}} \quad \Rightarrow \quad \dot{\boldsymbol{\sigma}} - \dot{\boldsymbol{\sigma}}^0 = \mathbb{D}_{\mathrm{T}} : \dot{\boldsymbol{\varepsilon}} - \mathbb{D}_{\mathrm{T}}^0 : \dot{\boldsymbol{\varepsilon}}^0 + \mathbf{D}_{\mathbf{c}} \dot{\zeta} \tag{3-24}$$

Recognizing that at the inception of localization $\mathbb{D}_{\mathrm{T}} = \mathbb{D}_{\mathrm{T}}^0$ and also $\dot{\boldsymbol{\varepsilon}} - \boldsymbol{\varepsilon}^0 = \left(\dot{\boldsymbol{w}} \otimes \mathbf{n} + \mathbf{n} \otimes \dot{\boldsymbol{w}} \right) / 2$, one can write

$$\mathbf{n} \cdot \left(\dot{\boldsymbol{\sigma}} - \dot{\boldsymbol{\sigma}}^0 \right) = 0 \ \Rightarrow \ \mathbf{Q} \dot{\boldsymbol{w}} + \mathbf{n} \cdot \mathbf{D}_{\mathbf{c}} \dot{\zeta} = 0 \quad or \quad \dot{\boldsymbol{w}} = -\left(\mathbf{Q}^{-1} \cdot \mathbf{n} \cdot \mathbf{D}_{\mathbf{c}} \right) \dot{\zeta} \tag{3-25}$$

Thus, the inception of strain localization is possible with its rate controlled by the kinetics of chemical reaction. On the other hand, the instantaneous mode occurs when the bifurcation condition (3-23) is satisfied.

The propagation of damage is described by invoking the mathematical framework outlined below. Suppose that a crack, or a set cracks, form within the domain subjected to external loading under an ongoing chemical-interaction, Fig 3-2(a). For modeling the discontinuous deformation, the embedded discontinuity approach, which incorporates volume averaging, is employed here after ref. [19,20]. Within this approach, the considered reference volume $\Delta\Omega$ comprises a discontinuity which divides the domain into two distinct parts $\Delta\Omega^+$ and $\Delta\Omega^-$, as shown in Fig 3-2(b). The former, i.e $\Delta\Omega^+$, is in the positive direction of the normal $\mathbf{n}$ to the fractured zone.

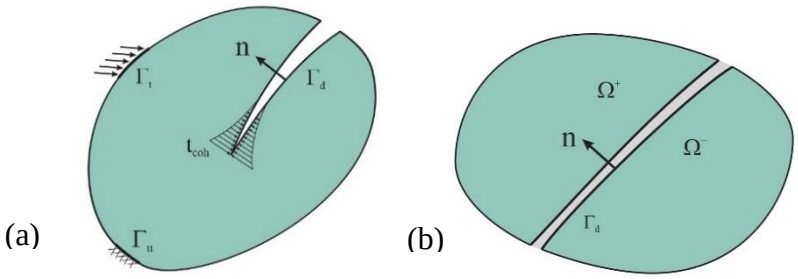

Fig 3-2- (a) Fractured domain under loading; (b) Discontinuity within the reference volume $\Delta\Omega$

To describe the displacement field within this domain, Heaviside step function, *H(x)*, is employed [26], i.e.

$$\mathbf{u}(\mathbf{x},t) = \bar{\mathbf{u}}(\mathbf{x},t) + H(\mathbf{x})\ \hat{\mathbf{u}}(\mathbf{x},t) \tag{3-26}$$

where $\bar{\mathbf{u}}$ and $\hat{\mathbf{u}}$ are two continuous functions. The strain rate is now defined as a symmetric part $(.)^s$ of the velocity gradient, corresponding to (3-26), i.e.

$$\dot{\boldsymbol{\varepsilon}} = \nabla^s \dot{\mathbf{u}}(\mathbf{x},t) = \nabla^s \dot{\bar{\mathbf{u}}}(\mathbf{x},t) + \nabla^s \dot{\hat{\mathbf{u}}}(\mathbf{x},t)\ H(\mathbf{x}) + \dot{\hat{\mathbf{u}}}(\mathbf{x},t) \otimes \nabla^s H(\mathbf{x}) \tag{3-27}$$

Taking the average of eq.(3-27) over the referential volume $\Delta\Omega$ and noting that $\nabla H(x) = \delta_{\Gamma_d}\mathbf{n}$, where δ is the Dirac delta function, one obtains [20]

$$\frac{1}{\Delta\Omega}\int_{\Delta\Omega} \dot{\boldsymbol{\varepsilon}}\, \mathrm{d}\Omega = \frac{1}{\Delta\Omega}\left\{ \int_{\Delta\Omega} \nabla^s \dot{\bar{\mathbf{u}}}(\mathbf{x},t)\, \mathrm{d}\Omega + \int_{\Delta\Omega} \nabla^s \dot{\hat{\mathbf{u}}}(\mathbf{x},t)\ H(\mathbf{x})\, \mathrm{d}\Omega + \int_{\Delta\Gamma_d} \left(\dot{\boldsymbol{w}}(\mathbf{x},t) \otimes \mathbf{n}\right)^s \mathrm{d}\Gamma_d \right\} \tag{3-28}$$

where $\dot{\boldsymbol{w}}$ represents again the velocity discontinuity along the interface. Thus, in terms of volume averages, the macroscopic strain rate can be expressed as

$$\dot{\boldsymbol{\varepsilon}} = \nabla^s \dot{\bar{\mathbf{u}}}(\mathbf{x},t) + \left(\frac{\Delta\Omega^+}{\Delta\Omega}\right)\nabla^s \dot{\hat{\mathbf{u}}}(\mathbf{x},t) + \left(\frac{\Delta\Gamma_d}{\Delta\Omega}\right)\left(\dot{\boldsymbol{w}}(\mathbf{x},t)\otimes\mathbf{n}\right)^s \tag{3-29}$$

The term on the right-hand side can be interpreted as a sum of the strain rate in the intact material ($\dot{\bar{\boldsymbol{\varepsilon}}}$) and the deformation due to discontinuous motion along the interface ($\dot{\hat{\boldsymbol{\varepsilon}}}$), i.e.

$$\dot{\boldsymbol{\varepsilon}} = \underbrace{\nabla^s\left(\dot{\bar{\mathbf{u}}}(\mathbf{x},t) + \vartheta\,\dot{\hat{\mathbf{u}}}(\mathbf{x},t)\right)}_{\dot{\bar{\boldsymbol{\varepsilon}}}} + \underbrace{\chi\left(\dot{\boldsymbol{w}}(\mathbf{x},t)\otimes\mathbf{n}\right)^s}_{\dot{\hat{\boldsymbol{\varepsilon}}}} \;\; ; \quad \chi = \Delta\Gamma_d/\Delta\Omega \tag{3-30}$$

Here, ϑ denotes the ratio $\Delta\Omega^+/\Delta\Omega$ and χ is the *characteristic length* parameter which is defined as the ratio of the area of fracture zone and the considered reference volume. The velocity discontinuity along the interface can be determined by imposing the condition of continuity of traction, i.e.

$$\mathbf{n}\cdot\dot{\boldsymbol{\sigma}} = \dot{\boldsymbol{t}} = \mathbf{K}\,\dot{\boldsymbol{w}} \tag{3-31}$$

were, $\boldsymbol{t}$ is the traction vector and $\mathbf{K}$ defines the stiffness operator of the fractured zone. Substituting now relation (3-15) in eq.(3-31) and solving for the velocity discontinuity, one obtains

$$\dot{\boldsymbol{w}} = \left(\mathbf{S}\otimes\mathbf{n}\right) : \left[\mathbb{D}_T : \dot{\boldsymbol{\varepsilon}} - \mathbf{D}_c\,\dot{\zeta}\right]; \quad \textit{where} \quad \mathbf{S} = \left[\mathbf{K} + \chi\left(\mathbf{n}\cdot\mathbb{D}_T\cdot\mathbf{n}\right)\right]^{-1} \tag{3-32}$$

The global constitutive relation can be derived by substituting the expression above in representation (3-30). This, after some algebraic transformations, leads to

$$\dot{\boldsymbol{\sigma}} = \bar{\mathbb{D}}_T : \dot{\boldsymbol{\varepsilon}} - \bar{\mathbf{D}}_c\,\dot{\zeta}\;; \qquad \bar{\mathbb{D}}_T = \mathbb{L} : \mathbb{D}_T \quad \textit{and} \quad \bar{\mathbf{D}}_c = \mathbb{L} : \mathbf{D}_c \tag{3-33}$$

where $\bar{\mathbb{D}}_T$ and $\bar{\mathbf{D}}_c$ are the stiffness operators for the domain that contains a strong discontinuity and $\mathbb{L}$ represents the *localization tensor* defined as

$$\mathbb{L} = \mathbb{I} - \chi\,\mathbb{D}_T : \left(\mathbf{n}\otimes\mathbf{S}\otimes\mathbf{n}\right) \tag{3-34}$$

Note again that the relation (3-34), and thus the constitutive equation (3-33), explicitly incorporate the characteristic length parameter χ. This parameter, which is defined as $\chi = \Delta\Gamma_d/\Delta\Omega$, can be expressed in an equivalent form as the ratio of the volume fraction of the damaged zone μ to its

thickness h. Indeed, since $\mu = h\ \Delta\Gamma_d / \Delta\Omega$, there is $\chi = \mu / h$. This particular definition stems directly from describing the embedded discontinuity response in terms of the rate of traction vs velocity discontinuity relationship (cf. [19]). It should be noted that in the earlier paper [18], as well as in the recent article by Nguyen et al.[27], the response in the localization zone was defined explicitly by a rate form of stress-strain relation, which resulted in identifying the characteristic length parameter with μ. In general, both approaches, i.e. that incorporating $\chi = \mu / h$ and μ, generate solutions insensitive to the finite element mesh size; the former one however, which is employed in this study, seems physically more appealing as the interface testing involves directly the measurements of displacement discontinuities.

In order to complete the formulation, a constitutive relation for the fractured zone is required that relates the rate of traction to the velocity discontinuity. Here, the characteristics of interface in the *tensile* regime have been defined by generalizing the approach outlined in ref. [28]. The latter employs an equivalent traction, t_{eq}, together with a conjugate measure of displacement discontinuity, w_{eq}. The initiation of damage may be described by invoking the concept of a damage locus that is represented by an elliptic curve

$$F_d = t_{eq} - f_t = 0; \quad t_{eq} = \sqrt{t_n^2 + \left(\frac{t_s}{\beta}\right)^2}\ ; \quad t_s = \left(t_{s1}^2 + t_{s2}^2\right)^{1/2}; \quad \beta = \frac{c}{f_t} \tag{3-35}$$

where the components of traction vector $\boldsymbol{t}$ are referred to a local coordinate system $\{n, s_1, s_2\}$ attached to the interface, with n and s_1, s_2 specifying the normal and tangential directions, respectively. The parameter β represents the ratio of the ultimate shear strength c (i.e. cohesion) to the tensile strength f_t. A conjugate equivalent measure of displacement discontinuity can now be defined as

$$w_{eq} = \sqrt{w_n^2 + \beta^2 w_s^2}; \quad w_s = \left(w_{s1}^2 + w_{s2}^2\right)^{1/2} \tag{3-36}$$

Differentiating the above equation, the rate of work can be expressed in the form

$$\dot{w}_{eq} = \frac{w_n}{w_{eq}}\dot{w}_n + \beta^2 \frac{w_{s1}}{w_{eq}}\dot{w}_{s1} + \beta^2 \frac{w_{s2}}{w_{eq}}\dot{w}_{s2} \ \Rightarrow\ t_{eq}\dot{w}_{eq} = t_n\dot{w}_n + t_{s1}\dot{w}_{s1} + t_{s2}\dot{w}_{s2} \tag{3-37}$$

so that

$$t_n = \hat{K}\, w_n\,; \quad t_{s1} = \beta^2 \hat{K}\, w_{s1}\,; \quad t_{s2} = \beta^2 \hat{K}\, w_{s2}\,; \quad t_{eq} = \hat{K}\, w_{eq} \tag{3-38}$$

The damage process involves a progressive degradation of strength, which can be described by introducing an exponential function

$$t_{eq} = \hat{K}\, w_{eq} = K_0 D\, w_{eq}\,; \quad D = \frac{\alpha_0}{\alpha} \exp\left(-\frac{f_t}{G_f}(\alpha - \alpha_0) \right); \qquad \alpha_0 = \frac{f_t}{K_0} \tag{3-39}$$

In the expression above, K_0 is the elastic stiffness, α_0 denotes the equivalent displacement at which the attenuation of stiffness starts, α is the maximum equivalent displacement attained during the loading history, and G_f is the fracture energy. Thus, the constitutive relation assumes the following form

$$\textit{Elastic range}:\ t_{eq} = K_0\, w_{eq} \ \ (\textit{for}\ w_{eq} \le \alpha_0); \quad \textit{Softening}:\ t_{eq} = \hat{K}\, w_{eq} \ \ (\textit{for}\ w_{eq} = \alpha \ge \alpha_0) \tag{3-40}$$

For an active loading process, the relation between the rate of traction and the velocity discontinuity, can be obtained by differentiating eqs. (3-38). Thus,

$$\dot{t}_n = \hat{K}\, \dot{w}_n + \dot{\hat{K}}\, w_n, \quad \dot{t}_{s1} = \beta^2 \left(\hat{K}\, \dot{w}_{s1} + \dot{\hat{K}}\, w_{s1} \right), \quad \dot{t}_{s2} = \beta^2 \left(\hat{K}\, \dot{w}_{s2} + \dot{\hat{K}}\, w_{s2} \right) \tag{3-41}$$

where

$$\dot{\hat{K}} = \frac{\partial \hat{K}}{\partial \alpha}\, \dot{w}_{eq} = K_0 \frac{\partial D}{\partial \alpha} \left(\frac{w_n}{\alpha}\, \dot{w}_n + \beta^2 \frac{w_{s1}}{\alpha}\, \dot{w}_{s1} + \beta^2 \frac{w_{s2}}{\alpha}\, \dot{w}_{s2} \right) \tag{3-42}$$

The above expression leads, after some algebraic transformations, to the general form of the constitutive law, in which the stiffness operator is defined as

$$\mathbf{K} = \frac{K_0}{\alpha}\frac{\partial D}{\partial \alpha}\begin{bmatrix} \alpha D\left(\frac{\partial D}{\partial \alpha}\right)^{-1} + w_n^2 & \beta^2 w_n w_{s1} & \beta^2 w_n w_{s2} \\ \beta^2 w_n w_{s1} & \beta^2 \alpha D\left(\frac{\partial D}{\partial \alpha}\right)^{-1} + \beta^4 w_{s1}^2 & \beta^4 w_{s1} w_{s2} \\ \beta^2 w_n w_{s2} & \beta^4 w_{s1} w_{s2} & \beta^2 \alpha D\left(\frac{\partial D}{\partial \alpha}\right)^{-1} + \beta^4 w_{s2}^2 \end{bmatrix} \quad (3\text{-}43)$$

Note that this operator needs to be transformed to the global coordinate system, before being implemented in eq.(3-32).

In the *compression* regime, i.e. when the frictional response is dominant, the stiffness operator is derived by invoking the plasticity framework, which incorporates strain-softening. In this case, the elastic response is defined as $\dot{\boldsymbol{t}} = \mathbf{K}^e \dot{\boldsymbol{w}}^e$ where the elastic stiffness, referred again to a local coordinate system attached to the interface, is given by

$$\mathbf{K}^e = \begin{bmatrix} K_0 & 0 & 0 \\ 0 & \beta^2 K_0 & 0 \\ 0 & 0 & \beta^2 K_0 \end{bmatrix} \quad (3\text{-}44)$$

In the elasto-plastic range, the Coulomb criterion together with a linear form of plastic potential function is employed, i.e.

$$F_c = t_s + t_n \tan\phi - c = 0; \quad \psi = t_s + t_n \tan\varphi = const. \quad (3\text{-}45)$$

where ϕ is the angle of internal friction, c is the cohesion and φ is the dilatancy angle. Note that for $t_n = 0$ there is $t_s = c$, which is consistent with representation (3-35). For an active loading process, ϕ is assumed to be constant, while cohesion progressively decreases from an initial value of c_0. The latter representation is similar to that followed in ref.[29]. The softening effects are attributed to the irreversible part of equivalent displacement, i.e.

$$c = c_0 \exp(-\frac{c_0}{G_c}\kappa) \quad ; \quad \dot{\kappa} = \sqrt{\left(\dot{w}_n^p\right)^2 + \bar{\beta}^2\left(\dot{w}_s^p\right)^2} \quad (3\text{-}46)$$

Here, w_n^p is the plastic dilatancy and G_c is the fracture energy in compression regime. Employing the consistency condition $\dot{f} = 0$, i.e.

$$\dot{f} = \frac{\partial f}{\partial \boldsymbol{t}}\dot{\boldsymbol{t}} + \frac{\partial f}{\partial \kappa}\dot{\kappa} = 0\ ;\ \Rightarrow\ \frac{\partial f}{\partial \boldsymbol{t}}\mathbf{K}^e\left(\dot{\boldsymbol{w}} - \dot{\lambda}\frac{\partial \psi}{\partial \boldsymbol{t}}\right) + \frac{\partial f}{\partial \kappa}\dot{\lambda}\left(\left(\frac{\partial \psi}{\partial t_n}\right)^2 + \bar{\beta}^2\left(\frac{\partial \psi}{\partial t_s}\right)^2\right)^{1/2} = 0 \quad (3\text{-}47)$$

and solving eq. (3-47) for $\dot{\lambda}$, we have

$$\dot{\lambda} = \frac{\left(\frac{\partial f}{\partial \boldsymbol{t}}\right)\mathbf{K}^e\,\dot{\boldsymbol{w}}}{\bar{H}_e + \bar{H}_p}\ ;\quad \bar{H}_e = \frac{\partial f}{\partial \boldsymbol{t}}\mathbf{K}^e\frac{\partial \psi}{\partial \boldsymbol{t}};\quad \bar{H}_p = -\left(\frac{\partial f}{\partial \kappa}\right)\left(\tan^2\varphi + \bar{\beta}^2\right)^{1/2} \quad (3\text{-}48)$$

where $\bar{H}_p$ is the plastic modulus. It should be noted that for $\varphi = 0$ and $\bar{\beta} = 1$ there is $\bar{H}_p = \frac{\partial c}{\partial \kappa}$. This case corresponds to $\dot{\kappa} = \dot{w}_s^p$, i.e. the softening effects are attributed to the irreversible part of tangential displacement alone. Following now the standard plasticity procedure, the constitutive law for the fractured zone is obtained, viz.

$$\dot{\boldsymbol{t}} = \mathbf{K}^e\left(\dot{\boldsymbol{w}} - \dot{\boldsymbol{w}}^p\right) = \mathbf{K}^e\left(\dot{\boldsymbol{w}} - \dot{\lambda}\frac{\partial \psi}{\partial \boldsymbol{t}}\right) = \left\{\mathbf{K}^e - \frac{\left(\mathbf{K}^e\frac{\partial \psi}{\partial \boldsymbol{t}}\right)\left(\frac{\partial f}{\partial \boldsymbol{t}}\mathbf{K}^e\right)}{\bar{H}_e + \bar{H}_p}\right\}\dot{\boldsymbol{w}} = \mathbf{K}\,\dot{\boldsymbol{w}} \quad (3\text{-}49)$$

Once more, the stiffness operator $\boldsymbol{K}$ needs to be transformed to the global frame of reference in order to specify the localization tensor $\boldsymbol{S}$ viz. eq.(3-32). It should be noted that $\boldsymbol{K}$, as defined in eq.(3-43) and eq.(3-49), is negative-definite.

Let us note that the exponential softening rules (35) and (42) applicable to tensile and shear modes imply the growth of damage process zone into the elastic material with no propagation of cracked zone, as the interface traction does not vanish for large normal or tangential displacement discontinuity. On the other hand, frequently used in concrete mechanics linear or bi-linear softening rules imply both process zone and cracked zone growth. The definition of process zone is therefore different for these two types of softening rules. In fact, for linear softening rules two

parameters, namely crack and process zone lengths with their evolutions should be used in the analysis of localized damage process.

3.5.3 Comments on the finite element formulation

The description of quasi-static damage propagation in the presence of a chemo-mechanical interaction follows a standard finite element procedure. The latter invokes the statement of virtual work principle

$$\int_{\Omega} \delta\boldsymbol{\varepsilon} : \boldsymbol{\sigma}\ d\Omega = \int_{\Gamma_t} \delta\mathbf{u}\cdot\mathbf{t}\ d\Gamma_t + \int_{\Omega} \delta\mathbf{u}\cdot\mathbf{g}\, d\Omega \tag{3-50}$$

where $\delta\mathbf{u}$ represents the virtual displacement, $\delta\boldsymbol{\varepsilon}$ is the associated virtual strain, $\mathbf{t}$ is the traction along the surface Γ_t (Fig 3-2) and $\mathbf{g}$ denotes the gravitational load. The finite element approximation of eq.(3-50) is based on incorporation of a set of shape functions that relate the kinematic variables to the nodal degrees of freedom. Employing the matrix notation, the standard FEM interpolations take the form

$$\{\delta\mathbf{u}\} = [\mathbf{N}]\left\{\delta\mathbf{u}^{\mathrm{N}}\right\} \rightarrow \{\delta\boldsymbol{\varepsilon}\} = [\mathbf{B}]\left\{\delta\mathbf{u}^{\mathrm{N}}\right\} \tag{3-51}$$

where $[\mathbf{N}]$ is the matrix of element shape functions, $[\mathbf{B}]$ is the operator employing derivatives of these functions and $\left\{\delta\mathbf{u}^{\mathrm{N}}\right\}$ are the virtual nodal displacements. By substituting the approximations (3-51) into eq. (3-50), the matrix form of the FE formulation can be derived, viz.

$$\int_{\Omega} [\mathbf{B}]^{\mathrm{T}}\{\boldsymbol{\sigma}\}\ d\Omega = \{\mathbf{F}\}; \qquad \{\mathbf{F}\} = \int_{\Gamma_t} [\mathbf{N}]^{\mathrm{T}}\{\mathbf{t}\}\ d\Gamma_t + \int_{\Omega} [\mathbf{N}]^{\mathrm{T}}\{\mathbf{g}\}\, d\Omega \tag{3-52}$$

For the chemo-plasticity framework employed in this work, the constitutive relation is defined via a differential form (3-33), which can be expressed in matrix notation as

$$\{\dot{\boldsymbol{\sigma}}\} = [\bar{\mathbb{D}}_{\mathrm{T}}]\{\dot{\boldsymbol{\varepsilon}}\} - [\bar{\mathbf{D}}_{\mathbf{c}}]\dot{\zeta}\ ; \qquad [\bar{\mathbb{D}}_{\mathrm{T}}] = [\bar{\mathbb{D}}_{\mathrm{T}}][\mathbb{L}] \quad \textit{and} \quad [\bar{\mathbf{D}}_{\mathbf{c}}] = [\mathbf{D}_{\mathbf{c}}][\mathbb{L}] \tag{3-53}$$

where

$$[\mathbb{L}]=\left([\mathbf{I}]-\chi\,[\mathbf{n}][\mathbf{S}][\mathbf{n}]^T[\mathbb{D}_{\mathbb{T}}]\right);\quad [\mathbf{S}]=\left([\mathbf{K}]+\chi[\mathbf{n}]^T[\mathbb{D}_{\mathbb{T}}][\mathbf{n}]\right)^{-1} \tag{3-54}$$

and $[\mathbf{n}]$ is a 6×3 operator defined through relation (31), i.e. $\left\{\dot{\mathbf{t}}\right\}=[\mathbf{n}]^T\left\{\dot{\boldsymbol{\sigma}}\right\}$.

Differentiating now eq. (3-52) with respect to time and substituting the constitutive relation (3-33) the following FE approximation is obtained

$$\left(\int_{\Omega}[\mathbf{B}]^{\mathrm{T}}[\bar{\mathbb{D}}_{\mathrm{T}}]\,[\mathbf{B}]\,d\Omega\right)\left\{\dot{\mathbf{u}}^{\mathrm{N}}\right\}=\left\{\dot{\mathbf{F}}\right\}+\left\{\dot{\mathbf{F}}_c\right\};\qquad \left\{\dot{\mathbf{F}}_c\right\}=\int_{\Omega}[\mathbf{B}]^{\mathrm{T}}[\bar{\mathbf{D}}_{\mathbf{c}}]\dot{\zeta}\,d\Omega \tag{3-55}$$

Note that the generalized load vector, which appears on the right-hand side of eq.(3-55), results from the change in external load as well as from the continuing chemical interaction. The latter is an explicit function of time and its evolution is defined via the kinetics law (3-2).

The above set of non-linear equations can be combined for the complete element assemblage and solved using iterative techniques, such as Newton-Raphson scheme. In the numerical analysis, the crack paths is traced in a discrete manner using a local tracking approach, as described in ref.[30]. Within this scheme, the failure/bifurcation criterion is checked in the candidate elements adjacent to the crack tip and, if met, the average direction of propagation is established. In 3D case, in order to avoid numerical difficulties associated with an abrupt change in the crack surface orientation, a crack smoothening algorithm has been implemented [31].

It should be pointed out that in the approach pursued here, the effect of discontinuity is implicitly embedded in the functional form of the tangential operator $\bar{\mathbb{D}}_{\mathrm{T}}$. This stems from the volume averaging scheme, whereby the velocity discontinuity is derived from the macroscopic strain rate by defining the localization tensor, eq.(3-32). The present approach is in contrast to other methodologies for modeling fracture propagation, such as XFEM. In the latter case, the discontinuity is introduced explicitly into the discretized system using an enriched approximation space, i.e. enrichments in shape functions and additional degrees of freedom. While the procedure for tracing the crack path is analogous to that employed here, the XFEM approach requires an enhanced integration scheme with the back triangulation, which impairs its numerical efficiency. A direct comparison of both methodologies is provided in ref.[20], which demonstrates that the

present framework, which employs standard FEM interpolations, gives results that are virtually identical to those obtained using XFEM, while the computational effort is significantly reduced. A detailed discussion on the numerical accuracy of the approach presented here is also provided in ref.[32], where the concept of J-integral was employed to evaluate the energy release rate around the crack tip and its value was compared with those obtained from Extended FEM simulations as well as an analytical solution. Finally, it should be noted that by invoking the characteristic dimension χ, eq.(30), the numerical solution is virtually independent of the mesh size/alignment. This issue was explicitly addressed in both references quoted here, i.e. ref.[20] and [32].

3.6 Numerical analysis

In this section the results of numerical simulations are presented. The analysis is focused on the deterministic assessment of the size effect in a series of three-point bending tests as well as compression tests. In addition, a structural response under continuing ASR is examined. It is demonstrated that, by increasing the size of the structure, a spontaneous failure may occur under a sustained load.

3.6.1 Assessment of size effect in three-point bending of notched/un-notched specimens

The first case examined here is the evaluation of size effect in concrete beams subjected to three-point bending. The geometry of the problem is depicted in Fig 3-3(a). The notched beam has a varying height *D*, the span of 3*D*, while the out-of-plane thickness is fixed at *40mm*. The initial notch has the depth of 0.1*D*. The first set of simulations was carried out for three different heights of *D=80, 160 and 320mm*. The primary objective was to verify the performance of the model by comparing the results with experimental data reported by Le Bellego et al. [33]. Since the failure mode involves a tensile crack propagation, the material was assumed to be elastic-brittle. The key material properties were taken from the original reference; in particular, the following values were assumed

$$E=40{,}000\ MPa,\ \nu=0.2,\ f_t=2.9\ MPa,\ G_f=40\ N/m,\ \beta=1,\ \alpha_o=0.001\ mm$$

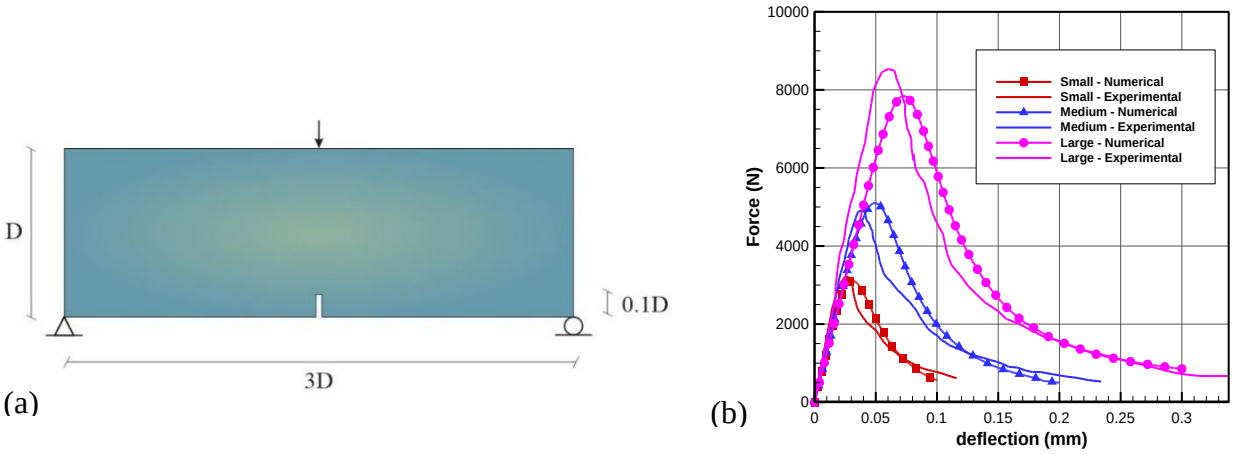

Fig 3-3- Size effect in notched beam; (a) geometry of the beam and (b) load-displacement curves

The load-deflection characteristics are presented in Fig 3-3(b). It is evident that the deformation becomes unstable after reaching the peak, while the ultimate strength is significantly affected by the size of the beam. It is noted that all simulations reported here employed the same finite element discretization, similar to that shown in Fig 3-4 below. Thus, the structural size effect is directly attributed to the size of the referential volume (identified here with the size of the element) that is associated with the domains containing the embedded discontinuity. The latter directly affects the characteristic length χ, which defines the localization operator $\boldsymbol{S}$ in eq.(3-32). The results of the simulations are fairly consistent with the experimental data, as evidenced in Fig 3-3(b).

The next set of simulations pertains to un-notched specimens subjected to the same loading conditions. The geometry of the beam and 3D FEM discretization of the problem are shown in Fig 3-4. This particular example was solved for a set of different values of *D* ranging from *D=20mm* to *D=1600 mm* and the thickness of the beam was taken again as *40 mm*. The details on sample geometries and the predicted values of nominal strength are provided in Table 1. The material properties are the same here as those employed in the previous example and the results are compared with those for the notched beam.

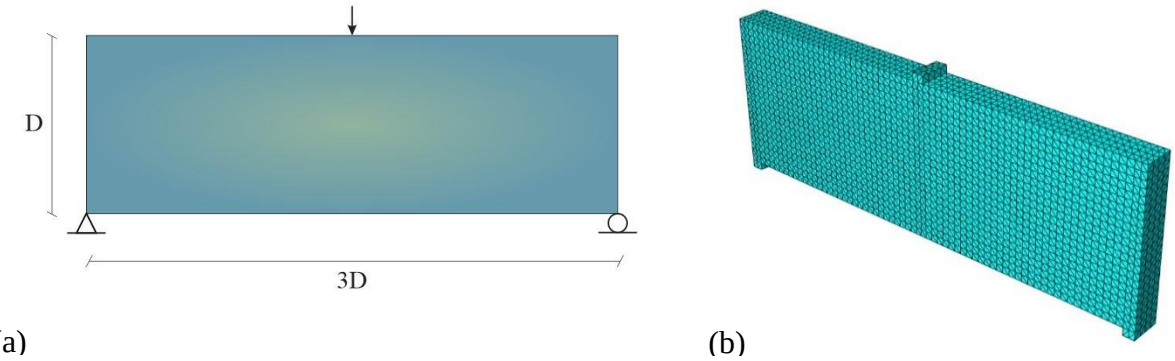

Fig 3-4- Size effect in un-notched beam; (a) geometry of the beam and (b) FE discretization

The failure mode involves, once again, the formation and upward propagation of a single macrocrack. Fig 3-5 shows the fracture mechanism (case #4) superimposed on the distribution of the horizontal stress; here, the attenuation of normal stress around discontinuity is clearly visible. It should be noted that according to theory of elasticity, the nominal stress for a beam of span L under three point bending is defined as $N_s=1.5FL/(D^2 t)$, where F is the magnitude of the applied load. Fig 3-6 shows the variation of nominal stress with the normalized displacement u/D, where u is the maximum deflection, for both notched and un-notched beams. Here, the upper curves, which correspond to the smallest sample (D=20 mm), show a ductile response. At the same time, for larger specimens the response becomes more brittle.

Finally, Fig 3-7 shows the variation of nominal strength, i.e., max N_s, versus the characteristic dimension D (in logarithmic scale). The results, for both un-notched and notched specimens, are supplemented here with the predictions which correspond to elastic -perfectly plastic idealization. For the latter case, the nominal strength is independent of the size of the structure, as the framework does not account for the localized nature of damage. The predicted upper limits on the strength are, in general, higher than those corresponding to small samples (case #1). It should be noted that for very small sizes (i.e. $D \to 0$) the use of a continuum formulation is not appropriate, as the size of the specimen becomes comparable to that of the aggregate. It is evident from Fig 3-7 that the strength in large un-notched samples is converging to the strength of concrete, i.e. $f_t=2.9$ MPa, whereas for the beams with pre-existing notches the nominal strength reduces below this value.

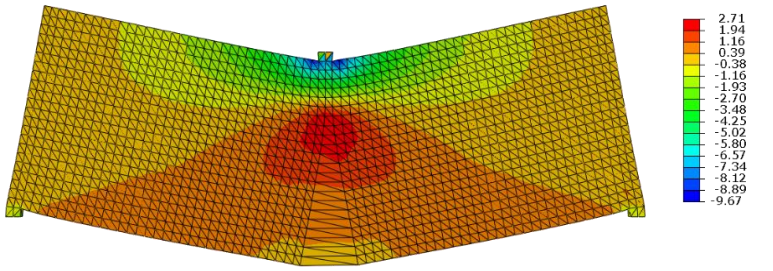

Fig 3-5- Deformed configurations with the superimposed stress distribution (in MPa)

Table 3-1- Dimensions and the result of three point bending test

Sample	*Height*	*Span*	Strength (MPa) un-notched	Strength (MPa) notched
Case 1	*20 mm*	*60 mm*	*6.86*	*5.05*
Case 2	*50 mm*	*150 mm*	*6.13*	*4.39*
Case 3	*100 mm*	*300 mm*	*5.39*	*3.75*
Case 4	*200 mm*	*600 mm*	*4.67*	*2.89*
Case 5	*400 mm*	*1200 mm*	*4.19*	*2.01*
Case 6	*800 mm*	*2400 mm*	*3.82*	*1.29*
Case 7	*1600 mm*	*4800 mm*	*3.55*	-----

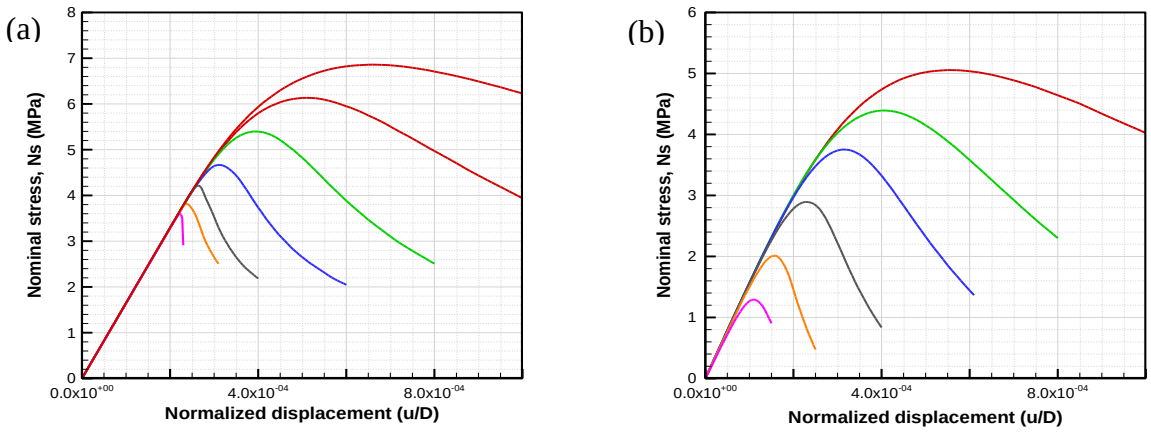

Fig 3-6- Variation of nominal stress with normalized displacement in un-notched (left) and notched (right) beams

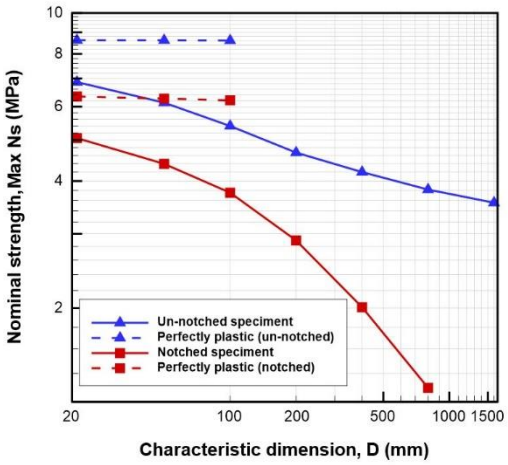

Fig 3-7- Variation of nominal strength with the size of structure for both notched/un-notched beams

3.6.2 Size effect in compression regime

The results reported in this section are focused on the assessment of size effect in concrete samples subjected to axial compression. The experimental data is taken from ref. [9]. The samples are prisms of width D and height 3D while the thickness is *50 mm*. In general, four specimens with the same aspect ratio and *D=50, 100, 200* and *400 mm*, were analyzed and the results are presented in Fig 3-8-11). The key material properties for concrete were taken as

$$E=30{,}000\ MPa,\ \nu=0.2,\ f_c=40\ MPa,\ c_1=1.9,\ c_2=0.6,\ c_3=0.3$$

while for the macrocrack: $c_0=10\,MPa,\ \varphi=0,\ \bar{\beta}=1,\ G_c=1.6\,N/mm$.

Note that the strength parameters c_1, c_2, c_3 as defined above, cf. eq.(3-4), are primarily a function of compressive strength f_c and the details on their specification are provided in ref.[24].

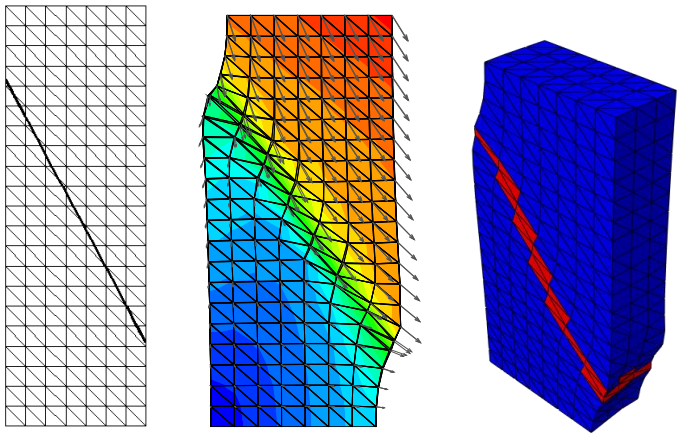

Fig 3-8- (left) propagation of localized damage (center) deformed configuration of the beam (right) cracked elements in 3D

In the simulations, in order to initiate the crack, an imperfection was introduced in the middle of specimen by reducing the compressive strength of concrete by 1%. The analysis was performed using 3D tetrahedral elements. The loading process consisted of applying increments of vertical displacements at the top of the specimen with no constraints on horizontal motion (i.e. frictionless loading platens). The local direction of shear band was assessed by performing the bifurcation analysis.

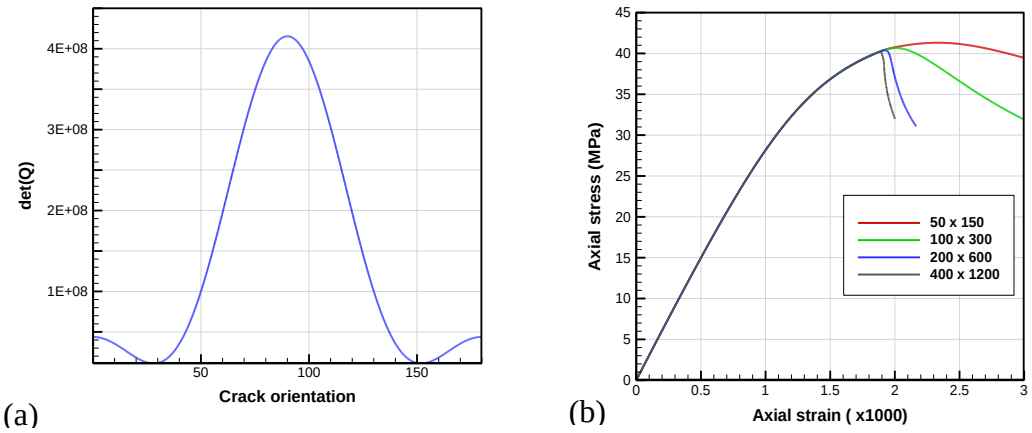

Fig 3-9- (a) typical variation of det(Q) with the crack direction; (b) axial stress-strain curves for all samples

Fig 3-9 (a) shows a typical variation of det(**Q**) with crack orientation; the latter defined as the angle between normal to the critical plane and the horizontal axis at the onset of localization. At the same time, Fig 3-9(b) presents the average axial stress–strain characteristics for different values of the

characteristic size of the structure *D*. The deformed configuration and the fracture pattern are depicted in Fig 3-8.

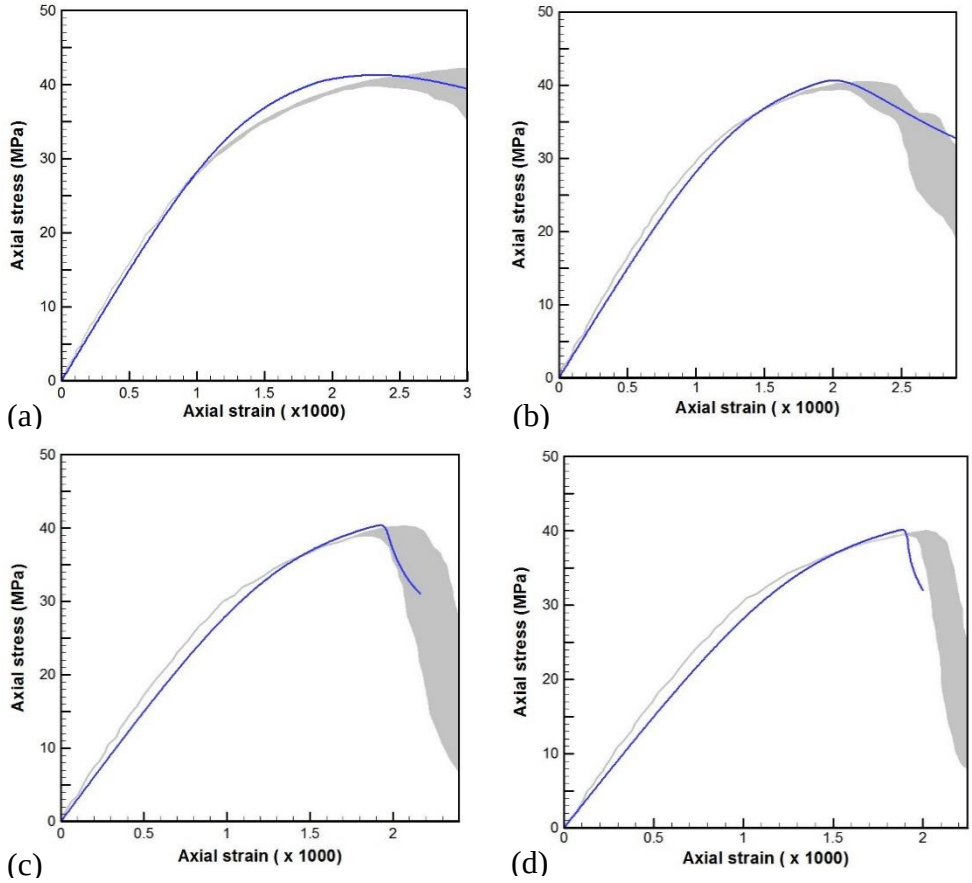

Fig 3-10- Comparison of predicted stress-strain curves versus experimental results; (a) *D=50mm*; (b) *D=100mm*; (c) *D=200mm*; (d) *D=400mm*;

In order to verify the accuracy of the solution, the results have been compared with the experimental data provided by Cusatis and Bazant [9]. The comparison is given in Fig 3-10. Note that for each size, 12 different samples were tested and the experimental scatter is indicated by the shaded area. It is evident that the ultimate strength is not significantly affected by the size of the specimen. At the same time, in small size specimens, the post-peak response shows significant ductility, while for large samples the behavior is more brittle. The variation of axial strength with the characteristic size of the structure *D* (in logarithmic scale) is shown in Fig 3-11(a). The numerical predictions are fairly consistent here with the experimental data, i.e. it is clear that the effect of size of the sample on the ultimate strength is virtually negligible Fig 3-11(b) presents the

variation of normalized post-critical modulus as a function of characteristic dimension *D*. Here, E_{pc} is the secant modulus after the peak load, while E_0 is the initial stiffness. It is evident that the brittleness of the structure is increasing linearly (in logarithmic scale) with an increase in size.

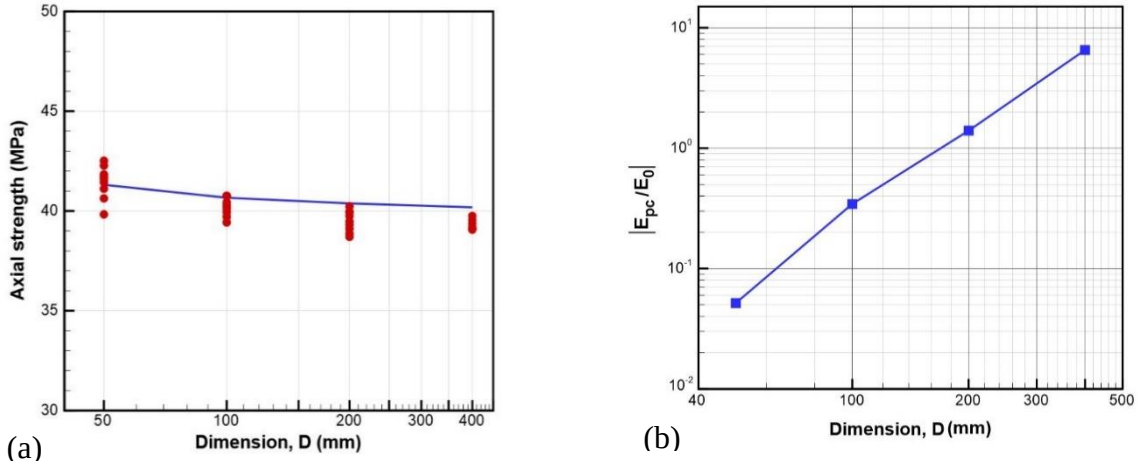

Fig 3-11- Size effect in axially compressed specimens

3.6.3 Size effect due to continuing ASR

The primary focus of the analysis reported here is the assessment of size effect in concrete beams subjected to continuing ASR. As mentioned earlier, the chemical reaction triggers the swelling of the material as well as degradation of its strength and deformation properties. In the study conducted here, five different specimens were considered with the height of *D*, the span of *4D* and the thickness of *0.5D*, as shown in Fig 3-12(a). The simulations were carried out for *D=25mm* (case 1), *D=75mm* (case 2), *D=150mm* (case 3), *D=300mm* (case 4) and *D=600mm* (case 5). The FE discretization employed again the tetrahedral elements, Fig 3-12(b), and the assumed values of material parameters are provided in Table 3-2. The beams were analyzed first under the loading conditions representing three-point bending (displacement-controlled scheme). For this loading stage, the corresponding load-displacement curves are shown in Fig 3-13(a).

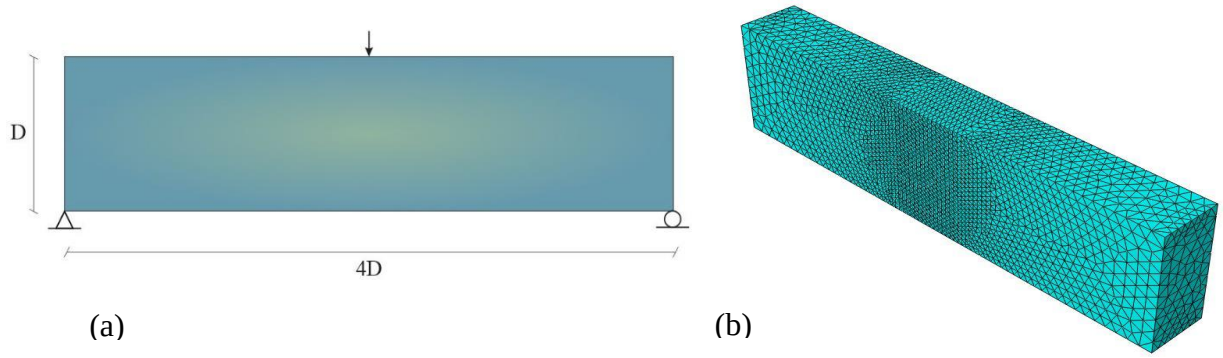

Fig 3-12- (a) Geometry of the beam; (b) Three dimensional FE discretization

The second stage of analysis involved a continuing ASR under a sustained load. In this case, the constitutive relation described in section 3.1 was employed. Two different scenarios were considered here that corresponded to different intensities of the vertical load/deflection. In the first case, the prescribed load intensity was different for each characteristic size of the beam and was equal to 0.97 of the peak load (Fig 3-13 (a)). During the continuing ASR, a progressive degradation of properties occurred that triggered the propagation of damage and a spontaneous loss of stability of the beam. This is illustrated in Fig 3-13(b) which shows the variation of normalized vertical displacement against time. It is evident, once again, that the ductility of the structure increases with a decrease in size. In addition, the time to failure strongly depends on the characteristic size. For the largest beam considered here (case 5) the failure occurs after 20 days of the reaction, while for the smallest size the loss of stability takes place after 130 days.

Table 3-2- Material properties of concrete

Material properties	
Modulus of elasticity	$E=30.5\ GPa$
Poisson ratio	$\nu=0.24$
Fracture energy	$G_f=50\ N/m$
Tensile strength	$f_t=3.6\ MPa$
Strength degradation parameter	$G_3=0.46$
Modulus of elasticity degradation parameter	$G_4=0.5$
Free expansion	$\varepsilon_\infty=4\times10^{-5}$
Chemical expansion coefficient	$\gamma=0.15\ months^{-1}$

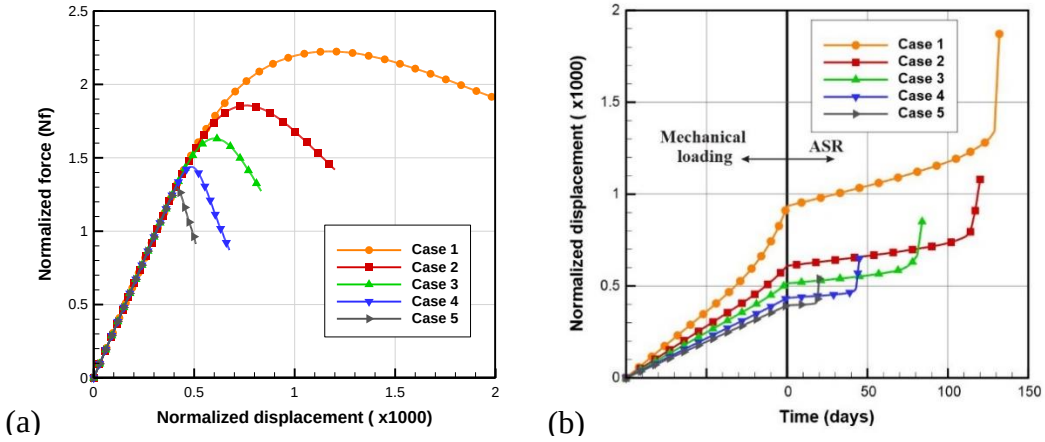

Fig 3-13- First loading scenario; (left) normalized load-displacement curves; (right) normalized displacement vs time

In the second loading scenario, the reaction is said to commence at a constant load intensity of $N_f=N_s/f_t=1.2$, which is below the value of ultimate load for all cases. This corresponds to a fixed value of normalized displacement of 4×10^{-4}, as shown in Fig 3-14. It is evident that, in this case, the smaller specimens will maintain stability over the entire period of the continuing ASR (set here to 900 days). At the same time, for larger samples, a spontaneous loss of stability occurs and the time to failure is affected by the characteristic size of the structure D.

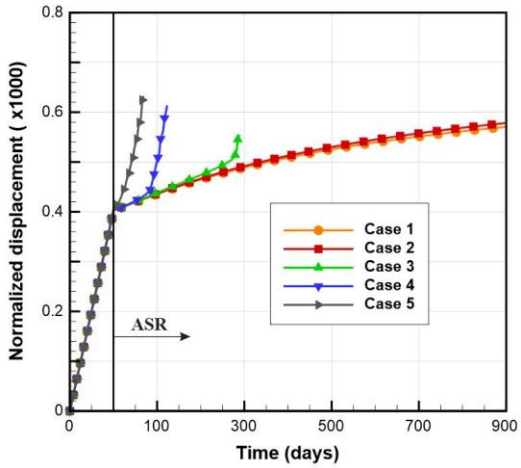

Fig 3-14- Second loading scenario, variation of normalized displacement with time

3.7 Concluding remarks

The objective of this work was to examine the size effect in concrete structures experiencing different fracture modes that included tensile failure, formation of macrocracks in compression regime as well as damage due to chemical interaction. It was clearly demonstrated that the size effect is triggered by the onset and propagation of localized damage; the latter associated with strain-softening, whose rate is controlled by a 'characteristic length' parameter. Although, this has already been recognized in the past, the concept of characteristic length has a certain degree of ambiguity and has not been precisely defined. In different works, it was loosely interpreted as the 'size of material inhomogeneities' or that of 'the fracture process zone'; i.e. no unique quantitative assessment was provided. In this work, the notion of the 'characteristic dimension' is associated with volume averaging in the neighborhood of the interface. The definition of χ in eq.(3-30), i.e. $\chi = \Delta\Gamma_{\mathrm{d}}/\Delta\Omega$, stems from expressing the interfacial response in terms of rate of traction and velocity discontinuity. The value of this parameter depends on the size of referential volume, implying that the tangential stiffness operator is explicitly affected by the size of FE mesh.

Most of the former studies on size effect dealt with quasi-brittle materials subjected to mechanical loading, primarily in tensile regime. Here, more general loading conditions were considered which included the degradation of concrete triggered by continuing alkali-silica reaction (ASR). For each type of loading, the same finite element discretization was used for different size of the structure. Note that, for a fixed finite element mesh, if the size of the structure increases, the 'characteristic length' represented by process zone varies within the elements containing discontinuity, which in turn affects the progress of damage propagation and, thus, the nominal strength of the structure. The first set of simulations dealt with the assessment of size effect in a series of three-point bending tests as well as compression tests. For continuing ASR, it was demonstrated that, by increasing the size of the structure, a spontaneous failure may occur under a sustained load. The evolution of process zone length was not studied in this paper.

It was argued that the existing analytical expressions for defining the size effect in geometrically similar structures are restrictive. They employ several parameters which are semi-empirical and

there is no systematic procedure for their identification. Furthermore, the nominal strength of a structure is affected by its actual geometry, boundary conditions and the strength/deformation properties of the material. All these aspects will significantly impact the strength and thus the size effect.

3.8 References

1. Bazant ZP. *Scaling of structural strength*. Butterworth-Heinemann: 2005.
2. Griffith AA. The phenomena of rupture and flow in solids. *Philosophical Transactions of the Royal Society,* 1921; 163-198.
3. Weibull W. A statistical distribution function of wide applicability. *Journal of Applied Mechanics ASME*, 1951; **18**: 293-297.
4. Shinozuka M. Probabilistic formulation for analytical modeling of concrete structures. *Defense Technical Information Center,* 1971.
5. Bazant ZP, Xi Y. Statistical size effect in quasi-brittle structures: I. Non-local theory. *Journal of Engineering Mechanics,* 1991; **117**: 2623-2640.
6. Bazant ZP, Planas J. *Fracture and size effect in concrete and other quasibrittle materials*. CRC Press: 1997.
7. Bažant ZP. Probability distribution of energetic-statistical size effect in quasibrittle fracture. *Probabilistic Engineering Mechanics,* 2004; **19**: 307-319.
8. Bažant ZP, Vořechovský M, Novák D. Asymptotic prediction of energetic-statistical size effect from deterministic finite-element solutions. *Journal of Engineering Mechanics,* 2007; **133**: 153-162.
9. Cusatis G, Bažant Z, Meschke G, De Borst R, Mang H, Bićanić N. Size effect on compression fracture of concrete with or without v-notches: A numerical mesomechanical study. *Computational modeling of concrete structures, Proc., EURO-C* 2006; 71-83.
10. Bazant ZP, Kim J-K. Size effect in shear failure of longitudinally reinforced beams. *ACI Journal Proceedings,* 1984; **81**: 456-468.
11. Zhang N, Tan K-H. Size effect in rc deep beams: Experimental investigation and STM verification. *Engineering Structures,* 2007; **29**: 3241-3254.
12. Kim T, Olek J. Chemical sequence and kinetics of alkali-silica reaction. Part 2: A thermodynamic model. *Journal of American Ceramic Society*, 2014; **97**: 2204-2212.
13. Bazant ZP, Steffens A. Mathematical model for kinetics of alkali–silica reaction in concrete. *Cement and Concrete Research,* 2000; **30**: 419-428.

14. Larive C. Apports combinés de l'expérimentation et de la modélisation à la compréhension de l'alcali-réaction et de ses effets mécaniques. *Ph.D. Thesis*, Ecole Nationale des Ponts et Chaussees, 1997.

15. Pietruszczak S. On the mechanical behaviour of concrete subjected to alkali-aggregate reaction. *Computers and Structures*, 1996; **58**: 1093-1097.

16. Saouma V, Perotti L. Constitutive model for alkali-aggregate reactions. *ACI Materials Journal*, 2006; **103**: 194-202.

17. Pietruszczak S, Ushaksaraei, Gocevski V. Modeling of the effects of alkali-aggregate reaction in reinforced concrete structures. *Computers and Concrete*, 2013; **12**: 627-650.

18. Pietruszczak S, Mróz, Z. Finite element analysis of deformation of strain softening materials. *International Journal for Numerical Methods in Engineering*, 1981; **17**: 327-334.

19. Pietruszczak S, "On homogeneous and localized deformation in water-infiltrated soils," *International Journal of Damage Mechanics*, 1999; **8**: 233-253.

20. Haghighat E, Pietruszczak S. On modeling of discrete propagation of localized damage in cohesive-frictional materials. *International Journal for Numerical and Analytical Methods in Geomechanics*, 2015; **39**: 1774-1790.

21. Bažant ZP. Size effect in blunt fracture: Concrete, rock, metal. *Journal of Engineering Mechanics*, 1984; **110**: 518-535.

22. Carpinteri A, Chiaia B, Ferro G. Size effects on nominal tensile strength of concrete structures: Multifractality of material ligaments and dimensional transition from order to disorder. *Materials and Structures*, 1995; **28**: 311-317.

23. Huang M, Pietruszczak S. Modelling of thermo-mechanical effects of alkali-aggregate reaction. *Journal of Engineering Mechanics*, 1999; **125**: 476-485.

24. Pietruszczak S, Jiang J, Mirza F. An elastoplastic constitutive model for concrete. *International Journal of Solids and Structures*, 1988; **24**: 705-722.

25. Rice J.R, Rudnicki J.W. A note on some features of the theory of localization of deformation. *International Journal of Solids and Structures*, 1980; **16**: 597-605.

26. Oliver J. Modelling strong discontinuities in solid mechanics via strain softening constitutive equations. Part 1: Fundamentals. *International Journal for Numerical Methods in Engineering*, 1996; **39**: 3575-3600.

27. Nguyen GD, Nguyen CT, Nguyen VP, Bui HH, Shen L. A size dependent constitutive modelling framework for localized failure analysis, Computational Mechanics, 2016; 58: 257- 280.

28. Dumstorff P, Meschke G. Crack propagation criteria in the framework of X-FEM based structural analyses. *International Journal for Numerical and Analytical Methods in Geomechanics*, 2007; **31**: 239-259.

29. Białas M, Mróz Z. Modelling of progressive interface failure under combined normal compression and shear stress. *International Journal of Solids and Structures*, 2005; **42**:4436-4467.

30. Jäger P, Steinmann P, Kuhl E. Modeling three-dimensional crack propagation—A comparison of crack path tracking strategies. *International Journal for Numerical Methods in Engineering*, 2008; **76**: 1328-1352.

31. Gasser TC, Holzapfel GA. 3D crack propagation in unreinforced concrete.: A two-step algorithm for tracking 3D crack paths. *Computer Methods in Applied Mechanics and Engineering*, 2006; **195**: 5198-5219.

32. Haghighat E, Pietruszczak S. On modeling of fractured media using an enhanced embedded discontinuity approach. *Extreme Mechanics Letters*, 2016; **6**: 10-22.

33. Le Bellégo C, Dubé JF, Pijaudier-Cabot G, Gérard B. Calibration of nonlocal damage model from size effect tests. *European Journal of Mechanics-A/Solids*, 2003; **22**: 33-46.

4 Analysis of localized fracture in 3D reinforced concrete structures using volume averaging technique

4.1 Contribution

This article describes a mesoscale approach for modeling of localized damage in reinforced concrete structures. The mathematical formulation of the constitutive equations governing both the homogeneous and localized deformation is provided. In the former case, a mixture theory is employed whereby a set of explicit static/kinematic constraints is imposed to define the response at the macroscale as a function of the volume fraction of constituents. The modeling of localized deformation is conceptually similar to that used in the former two articles. It employs the embedded discontinuity approach incorporating a smoothing algorithm. The constitutive law for the fractured zone is modified to include the presence of reinforcement, the latter considered as beams of a characteristic length embedded in the intact material. An important contribution in this work is the implementation of the proposed methodology in a series of boundary value problems that involve modeling of reinforced concrete structures in the presence of evolving discontinuities. It is shown that the proposed approach, which is much simpler in implementation as compared to XFEM, is quite adequate in capturing the propagation of macrocracks in reinforced concrete domains.

Analysis of localized fracture in 3D reinforced concrete structures using volume averaging technique

S. Moallemi and S. Pietruszczak

Department of Civil Engineering, McMaster University, Hamilton, Ontario, Canada

4.2 Abstract

In this paper, the propagation of localized damage in reinforced concrete structures is investigated in three-dimensional domain. A mesoscale approach is employed whereby the material is perceived as a composite medium comprising two constituents, i.e. concrete matrix and steel reinforcement. The response at the macroscale is obtained via a homogenization procedure that incorporates the volume averaging. After the onset of cracking in concrete, a traction-separation law is introduced for the fractured zone, in which the Timoshenko beam theory is used to assess the stiffness characteristics in the presence of reinforcement. A general 3D scheme for tracing the crack geometry is incorporated, which employs a smoothening algorithm. The mathematical formulation is incorporated in Abaqus user subroutine UMAT to verify the performance of the proposed methodology against the available experimental data. A number of numerical examples are given that examine the crack pattern formation and the associated fracture mechanism in concrete beams at different intensity of reinforcement.

Keywords: Reinforced concrete, 3D crack propagation, volume averaging scheme, crack smoothening algorithm, interface law

4.3 Introduction

Concrete, as a cement based material, has a high compressive strength and a low resistance in tension. In case of a low confinement, the behavior of plain concrete is brittle. In order to endow ductility and improve the structural performance, the steel reinforcement is often added. The latter not only increases the tensile strength, but also reduces the rate of crack opening/sliding due to interaction effects.

The response of a reinforced concrete structure is affected by the mechanical properties of the constituents, position and the volume fraction of reinforcement, the bonding between concrete and the steel bars and dowel action in the post-cracking region [1]. Over the last few decades, a number of experimental tests have been performed on reinforced concrete structures to assess the sensitivity to these factors. For example, Collins and co-workers [2, 3] examined the post-cracking strength of concrete panels, with different volume fractions of reinforcement, under normal and shear loading. Krefeld and Thurston [4] tested more than 200 beams with and without stirrups under concentrated and distributed load to determine the maximum shear resistance. Other series of tests included those by Mphonde and Frantz [5], who investigated the effect of compressive strength of concrete on the maximum shear capacity of beams without transverse stirrups under three-point bending. A more comprehensive review of experimental work is provided in various textbooks dealing with reinforced concrete design/analysis.

The numerical simulations of the mechanical response of reinforced concrete structures have been carried out by many researchers. Various constitutive models, of different degree of complexity, have been employed. An in-depth review of different methodologies can be found, for example, in ref.[6]. One of the earliest efforts of using finite element approach in the context of reinforced concrete was that of Ngo and Scordelis [7]. Their analysis was carried out for a pre-defined crack pattern assuming a linearly elastic response of steel/concrete. Both constituents were represented by 2D triangular elements and the bond slip was accounted for by using spring elements along the bar length. The frameworks that were developed later incorporated simplified phenomenological approaches largely based on a smeared crack methodology [8-10]. In the literature, two types of

smeared crack approaches were introduced; viz. fixed and rotating crack. In the former approach, pursued by Cervenka [11] and Pang [12], the orientation of the crack was assumed to remain fixed, while in the rotating crack approach the direction of discontinuity was updated based on the current stress state [13]. Both these approaches, in particular the latter one, may certainly be questioned in terms of the adequacy of the representation.

A more reliable description can be attained by accounting for the discontinuity in the displacement field triggered by the onset of cracking. In this approach, referred to as the strong discontinuity approach (SDA), the effect of discontinuity is considered based on traction-separation law which governs the response in the fractured zone. Details on this methodology can be found in refs. [14-15]. The SDA framework has been applied by Oliver et al. [16] to 2D analysis of reinforced concrete. In that work, the behaviour of concrete matrix was described using an isotropic damage model with strain-softening, while the reinforcement and the bond-slip interface were modeled by invoking uniaxial tensile and shear characteristics. Given some similarities of this approach to that pursued here, the main differences are highlighted in the last section that provides the final conclusions.

In parallel with this approach, the Extended Finite Element Method (XFEM) was developed whereby the presence of macrocrack has been described by adding additional degrees of freedom to the enriched elements [17,18]. The literature on modeling of fracture propagation within the XFEM framework is quite extensive. A comprehensive overview of the methodology, and its implementation in various areas of solid mechanics, is provided in the recent monograph by Khoei [19]. Examples of applications to cohesive crack growth include the works reported in refs.[20-22], which were all focused on modeling of quasi-brittle materials, such as concrete. In ref.[20], the macrocrack properties were defined in terms of an exponential relation between the total traction and the displacement discontinuity. An enhanced methodology was then presented by Moës and Belytschko [21] whereby the description of damage growth employed an enrichment scheme to avoid the stress singularity at the crack tip. The later work, reported by Asferg et al. [22], dealt with incorporation of additional enrichment functions to allow for the variation in the discontinuous displacement field on both sides of the crack. In recent years, the use of XFEM in modeling of cohesive crack growth has been expanded to multiphase materials. An example here

is a coupled numerical formulation outlined in ref. [23] for describing the hydraulic fracture propagation process in porous media.

The primary focus in this paper is on the modeling of localized damage in reinforced concrete structures. The approach employs a methodology which is computationally simpler than XFEM, but still accounts for a discrete nature of the fracture propagation process. Within this framework, the mechanical properties of reinforced concrete are described using a mesoscale approach that incorporates a volume averaging. Prior to the onset of fracture, some explicit static/kinematic constraints are imposed on the constituents' behavior that enable the specification of the tangential stiffness operator. This approach is a 3D generalization of a similar methodology employed in ref.[24] whereby two orthogonal sets of reinforcements were introduced. After formation of a macrocrack, a simplified form of SDA is employed based on an enhanced representation [25] of an embedded discontinuity approach [26]. Within this approach, the macrocrack subdivides the considered referential volume into intact material and the fractured zone. The interfacial properties are defined by relating the traction rate to velocity discontinuity and an implicit integration scheme is employed to enforce the continuity of traction along the interface. The general mathematical formulation is outlined in section 3, while section 4 describes the strategy for tracing the crack propagation path in 3D. The key contribution in this work is the implementation of the outlined methodology in a number of boundary value problems dealing with damage propagation in reinforced concrete structures. This aspect is addressed in section 5, whereby the predictive abilities of the framework are examined for different boundary conditions and intensities of reinforcement and the results are compared with the experimental evidence.

4.4 Mathematical formulation

In this section a constitutive relation describing the response of concrete with three orthogonal sets of reinforcements is presented. The problem is formulated in two stages involving (*i*) a homogeneous deformation mode prior to cracking of the concrete matrix, and (*ii*) localized deformation associated with formation of macrocracks. For the first stage, a set of explicit static

and kinematic constraints is imposed to define the response at the macroscale, while in the second stage, an embedded discontinuity approach is employed. The details of the formulation are provided below.

(i) Prior to cracking

Consider a representative volume of the material that comprises the concrete matrix and three orthogonal sets of reinforcing bars. Referring the problem to an arbitrary global coordinate system and employing volume averaging analogous to that used in the mixture theory, the overall stress/strain rates can be expressed as

$$\begin{aligned}\dot{\boldsymbol{\sigma}} &= \rho_c \dot{\boldsymbol{\sigma}}_{\mathbf{c}} + \rho_1 \dot{\boldsymbol{\sigma}}_1 + \rho_2 \dot{\boldsymbol{\sigma}}_2 + \rho_3 \dot{\boldsymbol{\sigma}}_3 \\ \dot{\boldsymbol{\varepsilon}} &= \rho_c \dot{\boldsymbol{\varepsilon}}_{\mathbf{c}} + \rho_1 \dot{\boldsymbol{\varepsilon}}_1 + \rho_2 \dot{\boldsymbol{\varepsilon}}_2 + \rho_3 \dot{\boldsymbol{\varepsilon}}_3\end{aligned} \tag{4-1}$$

Here, the subscript *c* refers to concrete matrix, the indexes *1, 2, 3* indicate the respective reinforcement's families and ρ_i denotes the volume fraction of i^{th} constituent in the mixture.

The local strain rate averages can be related to the overall macroscopic measure $\dot{\boldsymbol{\varepsilon}}$ (cf. Hill [27]) viz.

$$\dot{\boldsymbol{\varepsilon}}_{\mathbf{c}} = \mathbf{B}_{\mathbf{c}}\, \dot{\boldsymbol{\varepsilon}} \qquad \dot{\boldsymbol{\varepsilon}}_1 = \mathbf{B}_1\, \dot{\boldsymbol{\varepsilon}} \qquad \dot{\boldsymbol{\varepsilon}}_2 = \mathbf{B}_2\, \dot{\boldsymbol{\varepsilon}} \qquad \dot{\boldsymbol{\varepsilon}}_3 = \mathbf{B}_3\, \dot{\boldsymbol{\varepsilon}} \tag{4-2}$$

where the components of the localization tensors $\mathbf{B}_i$ are function of properties of constituents and their volume fractions. In this work, the operators $\mathbf{B}_i$ are estimated based on a simple approach in which the diameter of the reinforcement is assumed to be negligible as compared to the spacing. The problem is then formulated by imposing some explicit kinematic constraints on the axial deformation of both phases (i.e. reinforcement and concrete), while the interaction in the transverse direction is largely neglected. As a result, the local stress/strain fields remain uniform. The details on the specification of these operators are provided in the Appendix. Incorporating now the representation (4-2) in the averaging scheme (4-1), the macroscopic constitutive relation can be defined as

$$\dot{\bar{\boldsymbol{\sigma}}} = \left[\, \rho_c\, \mathbb{D}_{\mathbb{T}}^{(c)} \cdot \mathbf{B}_{\mathbf{c}} + \rho_1\, \mathbb{D}_{\mathbb{T}}^{(1)} \cdot \mathbf{B}_1 + \rho_2\, \mathbb{D}_{\mathbb{T}}^{(2)} \cdot \mathbf{B}_2 + \rho_3\, \mathbb{D}_{\mathbb{T}}^{(3)} \cdot \mathbf{B}_3 \,\right] : \dot{\bar{\boldsymbol{\varepsilon}}} = \mathbb{D}_{\mathbb{T}} : \dot{\bar{\boldsymbol{\varepsilon}}} \tag{4-3}$$

where $\mathbb{D}_{\mathbb{T}}^{(i)}$ is the stiffness of the i^{th} constituent and $\mathbb{D}_{\mathbb{T}}$ is the tangential operator for the mixture.

The representation (4-3) is general and can incorporate different frameworks for defining the stiffness operator(s). Note again that this is a meso-scale approach whereby the deformation history is traced in all constituents involved. The onset of localization typically takes place in the *concrete matrix*. For problems dealing with compressive stress regime, this is commonly assessed using the bifurcation criterion within the context of non-associated plasticity. However, the analysis presented here deals with problems involving elastic-brittle response that is associated with failure in tensile regime. Therefore, the behaviour of constituents is assumed to be elastic and the onset of localization in concrete is described by Rankine's (i.e. the maximum normal stress) criterion stipulating that the direction of macrocrack is perpendicular to the direction of maximum tensile stress in concrete. After the inception of localized damage, a simplified form of the strong discontinuity approach is employed as outlined in the section below.

(ii) After the onset of discontinuity

The propagation of discontinuous damage is described again by invoking an averaging scheme within a referential volume. The latter consists now of an intact material and the fractured zone intercepted by three orthogonal families of reinforcement, Fig 4-1(a). In this case, the discontinuity divides the considered volume, Ω, into two sub-domains Ω^+ and Ω^- .

(a)

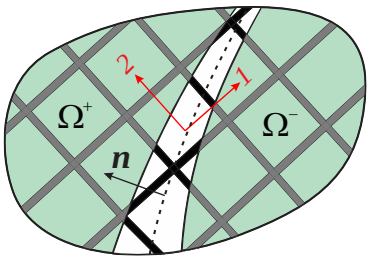

(b)

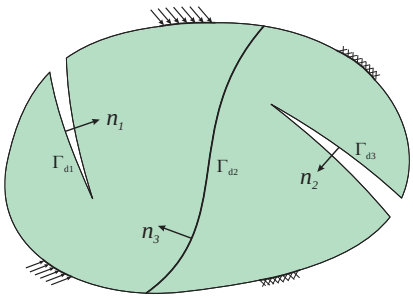

Fig 4-1- (a) Fractured zone within a referential volume; (b) A set of discontinuities within the entire domain subjected to prescribed boundary conditions

In order to define the displacement field, **u**(**x**,t), the following general representation is employed [15]

$$\mathbf{u}(\mathbf{x},t) = \bar{\mathbf{u}}(\mathbf{x},t) + H(\mathbf{x})\hat{\mathbf{u}}(\mathbf{x},t) \tag{4-4}$$

where $\bar{\mathbf{u}}(\mathbf{x},t)$ and $\hat{\mathbf{u}}(\mathbf{x},t)$ are two continuous functions and *H(x)* is the Heaviside step function describing the discontinuity within the domain. The strain tensor can now be obtained by calculating a symmetric part of the displacement gradient [25], i.e.

$$\boldsymbol{\varepsilon} = \nabla^s \mathbf{u}(\mathbf{x},t) = \nabla^s \bar{\mathbf{u}}(\mathbf{x},t) + \nabla^s \hat{\mathbf{u}}(\mathbf{x},t)\, H(\mathbf{x}) + \hat{\mathbf{u}}(\mathbf{x},t) \otimes \nabla^s H(\mathbf{x}) \tag{4-5}$$

By taking the average of this expression over the referential volume Ω, and using the properties of delta Dirac function, viz. $\nabla^s H(x) = \delta_{\Gamma_d}\mathbf{n}$, we have

$$\boldsymbol{\varepsilon} = \frac{1}{\Omega}\left\{ \int_\Omega \nabla^s \bar{\mathbf{u}}(\mathbf{x},t)\, \mathrm{d}\Omega + \int_\Omega \nabla^s \hat{\mathbf{u}}(\mathbf{x},t)\, H(\mathbf{x})\, \mathrm{d}\Omega + \int_{\Gamma_d} \left(\mathbf{w}(\mathbf{x},t) \otimes \mathbf{n}\right)^s \mathrm{d}\Gamma_d \right\} \tag{4-6}$$

where $\mathbf{w}$ is the displacement discontinuity along the crack surface. Differentiating now eq.(4-6) with respect to time, the macroscopic strain rate can be expressed in terms of respective averages as

$$\dot{\boldsymbol{\varepsilon}} = \nabla^s \left(\bar{\mathbf{u}}(\mathbf{x},t) + \vartheta \hat{\mathbf{u}}(\mathbf{x},t) \right) + \chi \left(\dot{\mathbf{w}}(\mathbf{x},t) \otimes \mathbf{n} \right) \tag{4-7}$$

Here, ϑ denotes the volume fraction Ω^+/Ω, while the parameter χ represents a *characteristic length*, which is defined as the ratio of the fractured area to the considered referential volume. The above relation can be interpreted as an additivity postulate in which the deformation at the macroscale is assumed to be the sum of the strain rate $\dot{\bar{\boldsymbol{\varepsilon}}} = \nabla^s \left(\bar{\mathbf{u}}(\mathbf{x},t) + \vartheta \hat{\mathbf{u}}(\mathbf{x},t) \right)$ in the intact material and $\dot{\hat{\boldsymbol{\varepsilon}}} = \chi \left(\dot{\mathbf{w}}(\mathbf{x},t) \otimes \mathbf{n} \right)$ that defines the strain rate due to the discontinuous deformation within the fractured zone. Given this decomposition, the stress rate in the intact material can be expressed as

$$\dot{\boldsymbol{\sigma}} = \mathbb{D}_{\mathbb{T}} : \left[\dot{\boldsymbol{\varepsilon}} - \chi \left(\dot{\mathbf{w}} \otimes \mathbf{n} \right) \right] \tag{4-8}$$

where $\mathbb{D}_{\mathbb{T}}$ is the tangential stiffness operator defined in eq. (4-3). In order to calculate the rate of crack opening, $\dot{\mathbf{w}}$, the continuity condition is employed whereby the traction along the crack surface is said to be the same as that within the fractured zone [28], i.e. $\mathbf{n}\dot{\boldsymbol{\sigma}} = \mathbf{K}\dot{\mathbf{w}}$. By substituting this condition in eq. (4-8), the velocity discontinuity can be defined as

$$\dot{\mathbf{w}} = \left(\mathbf{S} \otimes \mathbf{n}\right) : \mathbb{D}_{\mathrm{T}} : \dot{\boldsymbol{\varepsilon}} \quad \textit{where} \quad \mathbf{S} = \left[\mathbf{K} + \chi \left(\mathbf{n} \cdot \mathbb{D}_{\mathrm{T}} \cdot \mathbf{n}\right)\right]^{-1} \tag{4-9}$$

Here, $\mathbf{K}$ is the stiffness operator whose components depend on the properties of constituents and the geometric arrangement of reinforcement with respect to orientation of the macrocrack. The details on the specification of this operator are provided later in this section. The averaged macroscopic constitutive relation is obtained by combing eqs. (4-8) and (4-9), which leads to

$$\dot{\boldsymbol{\sigma}} = \mathbb{D}_{\mathbb{T}} : \left[\mathbb{I} - \chi \left(\mathbf{n} \otimes \mathbf{S} \otimes \mathbf{n}\right) : \mathbb{D}_{\mathbb{T}}\right] : \dot{\boldsymbol{\varepsilon}} = \bar{\mathbb{D}}_{\mathbb{T}} : \dot{\boldsymbol{\varepsilon}} \tag{4-10}$$

where $\bar{\mathbb{D}}_{\mathbb{T}}$ represents the tangential stiffness of the entire referential volume that contains the discontinuity.

The integration of eq.(4-10) can be carried out using an implicit scheme to calculate the crack opening and to update the stress state for each load increment. Employing the Taylor expansion, the following residuals can be defined [25]

$$\begin{cases} \boldsymbol{\Upsilon}_1 = \dot{\boldsymbol{\sigma}} - \mathbb{D}_{\mathbb{T}} : \left[\dot{\boldsymbol{\varepsilon}} - \chi \left(\dot{\mathbf{w}} \otimes \mathbf{n}\right)\right] = \mathbf{0} \\ \boldsymbol{\Upsilon}_2 = \mathbf{n}\,\dot{\boldsymbol{\sigma}} - \mathbf{K}\,\dot{\mathbf{w}} = \mathbf{0} \end{cases} \Rightarrow \begin{cases} \boldsymbol{\Upsilon}_1^{(k+1)} = \boldsymbol{\Upsilon}_1^{(k)} + \dfrac{\partial \boldsymbol{\Upsilon}_1^{(k)}}{\partial \boldsymbol{\sigma}} : \boldsymbol{\delta\sigma}^{(k)} + \dfrac{\partial \boldsymbol{\Upsilon}_1^{(k)}}{\partial \mathbf{w}} : \delta \mathbf{w}^{(k)} = \mathbf{0} \\ \boldsymbol{\Upsilon}_2^{(k+1)} = \boldsymbol{\Upsilon}_2^{(k)} + \dfrac{\partial \boldsymbol{\Upsilon}_2^{(k)}}{\partial \boldsymbol{\sigma}} : \boldsymbol{\delta\sigma}^{(k)} + \dfrac{\partial \boldsymbol{\Upsilon}_2^{(k)}}{\partial \mathbf{w}} : \delta \mathbf{w}^{(k)} = \mathbf{0} \end{cases} \tag{4-11}$$

where, k denotes the iteration number. Solving above set of equations for $\boldsymbol{\delta\sigma}$ and $\delta\mathbf{w}$, i.e. the correction of stress state and the crack opening, we have

$$\delta \mathbf{w}^{(k)} = \left[\mathbf{K} + \chi \mathbf{n} \cdot \mathbb{D}_{\mathbb{T}} \cdot \mathbf{n}\right]^{-1} \left(\boldsymbol{\Upsilon}_2^{(k)} - \mathbf{n}\,\boldsymbol{\Upsilon}_1^{(k)}\right); \quad \delta \boldsymbol{\sigma}^{(k)} = -\left[\boldsymbol{\Upsilon}_1^{(k)} + \chi \mathbb{D}_{\mathbb{T}} : \left(\mathbf{n} \otimes \delta \mathbf{w}^{(k)}\right)\right] \tag{4-12}$$

and the updated values become

$$\boldsymbol{\Delta\sigma}^{(k+1)} = \boldsymbol{\Delta\sigma}^{(k)} + \delta \boldsymbol{\sigma}^{(k)}; \quad \boldsymbol{\Delta w}^{(k+1)} = \boldsymbol{\Delta w}^{(k)} + \delta \mathbf{w}^{(k)} \tag{4-13}$$

The iterations continue until the residuals defined in (4-11), reach a predefined tolerance.

In order to complete the formulation, the constitutive relation for the fracture zone needs to be specified. The fracture zone is a composite medium in itself comprising the concrete interface reinforced with steel bars embedded in the matrix. The response of concrete within the damaged zone is described here by invoking a strain-softening relation, similar to that used in ref.[20].

Referring the problem to a local coordinate system $\{n, s_1, s_2\}$ *attached to the interface*, the evolution of the normal (*n*) and tangential (*s*) components of the traction vector is defined as

$$t_n = f_t \exp\left(-\frac{f_t}{G_f} w_n\right); \quad t_{s1} = f_s \exp\left(-\alpha w_n\right) w_{s1}; \quad t_{s2} = f_s \exp\left(-\alpha w_n\right) w_{s2} \tag{4-14}$$

Here, f_t is the tensile strength of concrete, G_f is the fracture energy and w_n, w_s denote the crack opening and sliding, respectively. For the shear components, f_s is the initial shear stiffness and α controls the rate of decrease of the shear traction. For an active loading process, both equations in (4-14) can be expressed in an incremental form, i.e.

$$\begin{gathered} \dot{t}_n = -\frac{f_t^2}{G_f} \exp\left(-\frac{f_t}{G_f} w_n\right) \dot{w}_n; \quad \dot{t}_{s1} = -\alpha f_s \exp\left(-\alpha w_n\right) w_{s1} \dot{w}_n + f_s \exp\left(-\alpha w_n\right) \dot{w}_{s1}; \\ \dot{t}_{s2} = -\alpha f_s \exp\left(-\alpha w_n\right) w_{s2} \dot{w}_n + f_s \exp\left(-\alpha w_n\right) \dot{w}_{s2} \end{gathered} \tag{4-15}$$

Given these relations, the stiffness operator for concrete within the fractured zone can be defined as

$$\begin{Bmatrix} \dot{t}_n \\ \dot{t}_{s1} \\ \dot{t}_{s2} \end{Bmatrix} = \underbrace{\begin{bmatrix} \frac{-f_t^2}{G_f} \exp\left(-\frac{f_t}{G_f} w_n\right) & 0 & 0 \\ -\alpha f_s \exp\left(-\alpha w_n\right) w_{s1} & f_s \exp\left(-\alpha w_n\right) & 0 \\ -\alpha f_s \exp\left(-\alpha w_n\right) w_{s2} & 0 & f_s \exp\left(-\alpha w_n\right) \end{bmatrix}}_{\mathbf{K}_c'} \begin{Bmatrix} \dot{w}_n \\ \dot{w}_{s1} \\ \dot{w}_{s2} \end{Bmatrix} \tag{4-16}$$

Specification of the constitutive relation for the damaged zone still requires consideration of strengthening effect of the steel network. In order to incorporate this effect, the reinforcing bars are considered as beams of a characteristic length *l* fixed at both ends within the intact material [24], Fig 4-2. The characteristic length itself is defined by the orientation of the reinforcement relative to the interface and the thickness of the damaged zone.

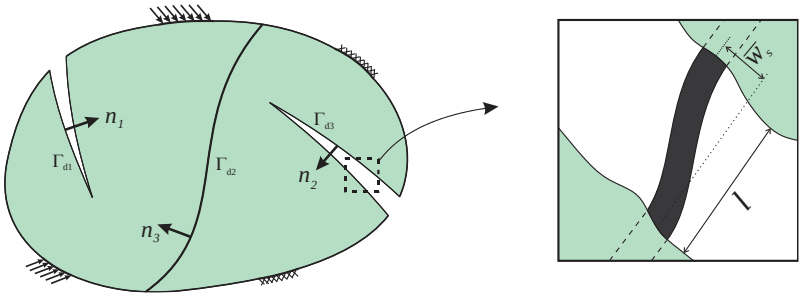

Fig 4-2- Reinforcement within the fractured zone

Referring the problem now to a local coordinate system $\{\bar{n}, \bar{s}_1, \bar{s}_2\}$ *along the reinforcement*, the normal and shear components of the traction vector can be obtained by employing classical Timoshenko beam theory. As shown in ref.[29], for a circular cross section with the diameter *d*, and length *l*, the traction-displacement relation in the elastic range can be expressed in the rate form

$$\dot{\bar{t}}_n = \left(\frac{E_s}{l}\right)\dot{\bar{w}}_n\,; \quad \dot{\bar{t}}_{s1} = \left(\frac{12E_sI}{(1+\xi)Al^3}\right)\dot{\bar{w}}_{s1}\,; \quad \dot{\bar{t}}_{s2} = \left(\frac{12E_sI}{(1+\xi)Al^3}\right)\dot{\bar{w}}_{s2}\,; \quad \xi = \frac{3}{2}(1+\nu_s)\left(\frac{d}{l}\right)^2 \tag{4-17}$$

Here, *A* and *I* denote the area and the moment of inertia of the rebar's cross section and E_s and ν_s are the Young's modulus and Poisson's ratio of steel, respectively. It is noteworthy to mention that in case of $l \gg d$, the tangential stiffness approaches $12E_sI/Al^3$, while for short beams the shear mode is dominant and the stiffness increases to $E_s/2(1+\nu)l$.

The transition from elastic to plastic response is defined based on yield criteria expressed in terms of components of the stress resultant system. In *mode-I* of crack propagation, when the shear force is small compared to normal force, the classical approach outlined by Horne is employed [30]. In this case, the yield criterion is expressed in a quadratic form

$$\frac{6M}{d^3 f_y} + \left(\frac{N}{A f_y}\right)^2 \le 1.0\ ; \quad M = \sqrt{{V_{s1}}^2 + {V_{s2}}^2}\,\frac{l}{2} \tag{4-18}$$

where f_y is the yield stress in axial tension, *M* is the bending moment at fixed ends of the beam, *N* is the axial force and V_{s1}, V_{s2} are the shear forces. The latter can be determined by invoking eq.(4-17), according to which

$$V_{s1} = \frac{12\,E_s I}{(1+\xi)l^3}\,\bar{w}_{s1}\,; \qquad V_{s2} = \frac{12\,E_s I}{(1+\xi)l^3}\,\bar{w}_{s2} \tag{4-19}$$

The yielding associated with mixed mode crack propagation, in which the shear mechanism is dominant, is evaluated independently using a maximum shear force criterion [30]

$$\frac{V}{V_p} \le 1.0\,; \quad V = \sqrt{{V_{s1}}^2 + {V_{s1}}^2} \;\; \textit{and} \;\; V_p = \frac{A\,f_y}{\sqrt{3}} \tag{4-20}$$

If any of the above criteria, viz. inequality (4-18) or (4-20), is met, the yielding of steel is said to commence.

The stiffness operator for the steel network within the fractured zone can be formally defined based on representation (4-17) and may be expressed in a general form

$$\bar{\mathbf{K}}_{\mathbf{i}} = \frac{\bar{E}}{l}\begin{bmatrix} 1 & 0 & 0 \\ 0 & \dfrac{12I}{(1+\xi)Al^2} & 0 \\ 0 & 0 & \dfrac{12I}{(1+\xi)Al^2} \end{bmatrix} \quad \text{and} \quad \bar{E} = \begin{cases} E_s & \text{Elastic} \\ (1-\omega)\,E_s & \text{Damaged state} \end{cases} \tag{4-21}$$

Here, the 'damaged state' refers to the onset of yielding in steel and ω is a damage parameter. Note that $\omega \to 1$ results in a perfectly plastic idealization (i.e., unlimited deformation), while $\omega \ge 1$ yields a negative-definite operator (strain softening). The latter representation has been used in several previous studies to address the debonding effect that is typically associated with this stage of deformation process ([16],[31]).

It should be emphasized that a rigorous description of debonding requires the specification of interfacial properties and their evolution during all stages of the deformation process. Given the difficulties associated with experimental identification of those properties, as well as the complexities associated with the geometry of the interface, this remains a rather intricate task. In

the existing literature, the loss of bonding is commonly described by invoking simplified one-dimensional bond-slip models and/or degrading the properties of constituents in the neighborhood of the interface (cf. [16], [31,32]). The simple approach adopted here, viz. a negative post-critical stiffness modulus, belongs to the latter category.

Finally, given the stiffness matrices for both constituents, viz. eqs.(4-16) and (4-21), the macroscopic stiffness operator for the fractured area can be defined as

$$\mathbf{K} = \rho_c \, \mathbf{T}^{\mathrm{T}} \, \mathbf{K}_{\mathbf{c}}' \, \mathbf{T} + \sum_{i=1,2,3} \rho_i \, \mathbf{R}_i^{\mathrm{T}} \, \bar{\mathbf{K}}_i \, \mathbf{R}_i \tag{4-22}$$

where $\mathbf{T}$ and $\mathbf{R}$ are the respective transformation matrices from the local to global coordinate systems.

4.5 Comments on tracing the crack propagation path

Once a macrocrack forms within an element, its position is defined by specifying the unit normal vector $\boldsymbol{n}$ at point P located on the discontinuity surface, Fig 4-3. In this work, the numerical simulations presented later in section 5 have been carried out by employing tetrahedral elements. For failure in tension, the Rankine's criterion was employed according to which the orientation of the crack is orthogonal to the direction of maximum principal stress. As shown in Fig 4-3, the crack will cut the element forming a triangular or quadrilateral surface. In order to calculate the characteristic length, χ, viz.eq.(4-7), the area of the crack surface and the volume of the element on both sides of discontinuity need to be determined. In the case of a triangular cut, Fig 4-3a, the points of intersection along each edge can be identified and the area of the triangle can be calculated by using the Heron's formula, i.e.

$$A = \sqrt{p(p-a)(p-b)(p-c)} \; ; \quad p = \frac{a+b+c}{2} \tag{4-23}$$

where a, b and c are the respective lengths of each side of the triangle. In the case of a quadrilateral

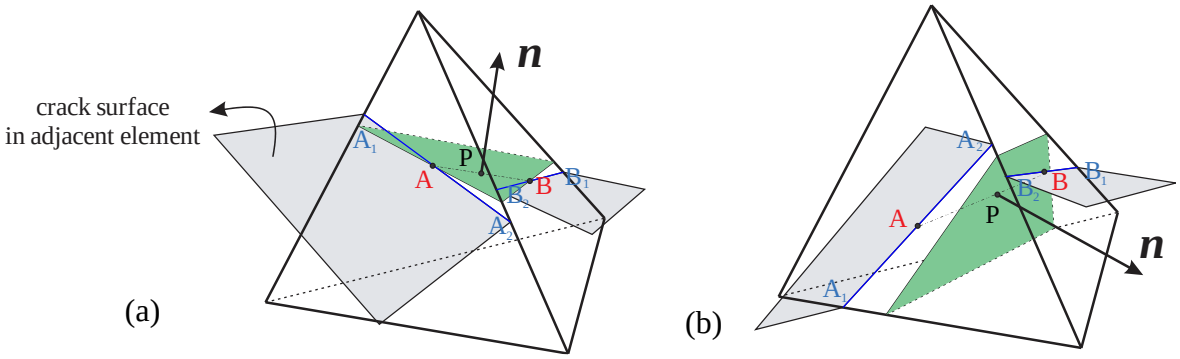

Fig 4-3- Crack surface in 3D element

cut, Fig 4-3b, the surface area can be divided into two triangles, so that eq.(4-23) can be again employed. To calculate the volume on each side of the discontinuity, i.e. Ω^+ and Ω^- , the element may be subdivided into tetrahedral domains, the volumes of which (V_t) are defined by $V_t = 1/3 A_t \; h_t$, where A_t is the area of base and h_t denotes the height of each tetrahedral subdivision. At the onset of cracking within the domain, the point P is assumed to be located at the centroid of the element and the unit normal $\boldsymbol{n}$ is along the direction of maximum principal stress. The same procedure is employed if the element is not intercepted by other cracks in the immediate neighborhood. For the propagating discontinuity, the location of point P is affected by the surrounding crack surfaces. Referring again to Fig 4-3, let two sides of the element be crossed by the crack surfaces passing through points A_1, A_2 and B_1, B_2, respectively. In this case, the coordinates of point P are the averages of the coordinates of the respective midpoints A and B.

It is noted that the assessment of the direction of unit normal $\boldsymbol{n}$, which is based on the direction of the principal stress triad, may not be accurate when the structure is close to failure. This may lead to inconsistencies with the orientation of adjacent crack surfaces (Fig 4-4(a)). In order to remedy this problem, a crack smoothening algorithm is implemented as described below (cf. ref. [33]).

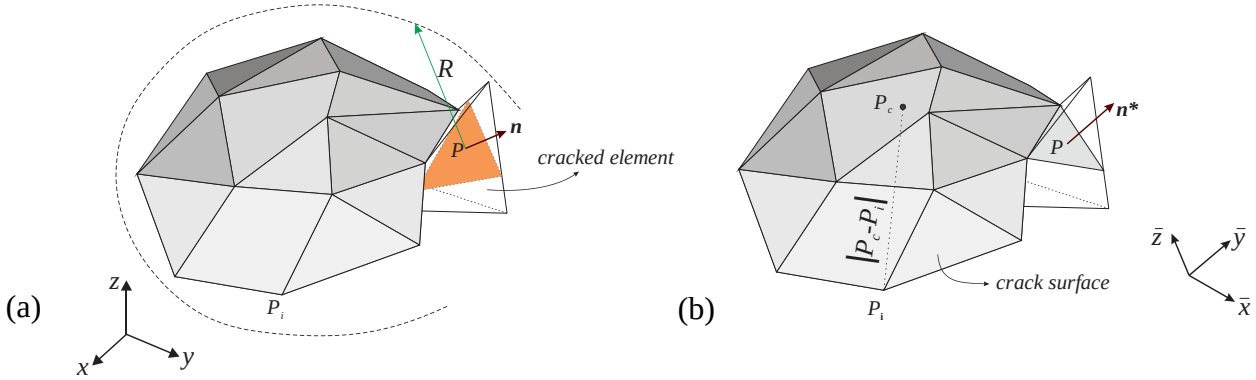

Fig 4-4- (a) Cracked surface within a sphere of radius R; (b) modified normal direction

In the first step of this procedure, a sphere of radius *R*, centered at point *P* is defined, as shown in Fig 4-4(a). The radius R is, in general, a user-selected variable which is typically in the range of 3-4 times of the new cracked element size [33]. The latter is defined as the average length of the edges in element. Denoting now the coordinates of all nodes within the sphere as P_i, Fig 4-4(b), the geometric center of the crack surface can be defined as $P_c = \sum_{i=1,n_s} P_i / n_s$, where n_s represents the number of nodes within the sphere. Thus, given the location of point P_c, a covariance tensor is defined based on the distance of each node from this point, i.e.

$$\mathbf{D} = \sum_{i=1,n^r} \left(P_i - P_c\right) \otimes \left(P_i - P_c\right) \tag{4-24}$$

The eigenvectors of tensor **D** specify the local coordinate system ($\bar{x}, \bar{y}, \bar{z}$) with origin at point P_c. In order to determine the new normal direction at the cracked element, a second order approximation function is employed, viz. $\bar{z} = a_0 + a_1\bar{x} + a_2\bar{y} + a_3\bar{x}^2 + a_4\bar{x}\bar{y} + a_5\bar{y}^2$, where the coefficients a_i represent the solution to the following least square problem [33]

$$\min \Psi = \sum_{i=1,n^r} \left(\bar{z}_i - \bar{z}(\bar{x}_i, \bar{y}_i)\right)^2 \tag{4-25}$$

Given the values of the approximation coefficients, the new crack surface can be defined. The normal direction is then obtained by evaluating the gradient of function $\bar{z}$ at point P_c, i.e. $\boldsymbol{n}^* = \nabla\bar{z}(p_c)$. Note that the direction $\boldsymbol{n}^*$ is associated with the local coordinate system, therefore a

standard transformation is required to define the components with respect to the selected global frame of reference.

4.6 Numerical simulations

In this section, a number of numerical examples are provided to demonstrate the predictive abilities of the outlined approach. The first example deals with crack propagation in a plain concrete beam, whereas the remaining ones involve reinforced concrete structures with different intensities of reinforcement. The results of numerical simulations are compared with the experimental data reported in the literature.

4.6.1 Crack propagation in a notched plain concrete beam

This example involves simulation of a mixed mode of crack propagation in a notched beam and the experimental results come from the work of John and Shah [34]. The geometry of the problem is presented in Fig 4-5. The concrete beam has the span of *203.2 mm*, the height of *76.2 mm* and the depth of *25.4 mm*. The structure is subjected to a vertical load applied in the middle of the span. The experimental tests have been carried out for a number of different loading rates; the results used here correspond to a slow rate that is representative of the static conditions.

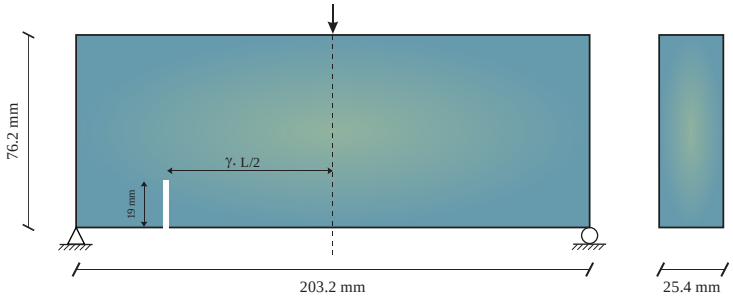

Fig 4-5- Geometry of the beam and the position of notch

The beam has a *19 mm* notch, which is located at an offset of ($\gamma L/2$) from the middle of the span. The numerical simulations were carried out using the following set of concrete properties taken from the original reference, i.e.

$$E_c = 31.37\,GPa, \quad \nu_c = 0.2, \quad f_t = 2.5\,MPa, \quad G_f = 60\ N/m$$

For this specific geometry, the crack propagation pattern is strongly affected by the offset parameter γ, Fig 4-5. For $\gamma < 0.73$ the crack initiates at the notch, while for larger offsets, the onset of fracture occurs in the middle of the span [35]. Here, two sets of simulations have been performed for γ=0.78 and γ=0.72 and the resulting crack trajectories are shown in Fig 4-6.

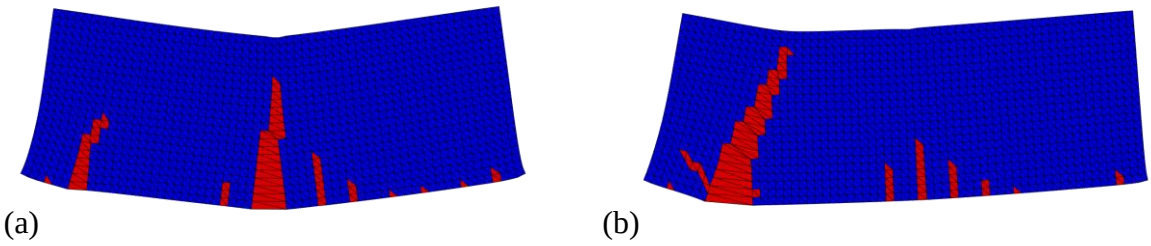

(a) (b)

Fig 4-6- Deformed mesh with cracked elements for (a) γ =0.78 and (b) γ =0.72

Fig 4-6(a) gives the fracture pattern for γ=0.78. Here, at the early stages of loading the cracks form at the notch as well as in the middle of beam. However, as the load increases, the propagation from the notch stops and the dominant crack runs through the middle of the span. For reduced values of the offset parameter γ, Fig 4-6(b), the crack forms at the notch and propagates towards the top of the beam in a direction inclined from the vertical. This is consistent with the experimental results, as evidenced in Fig 4-7.

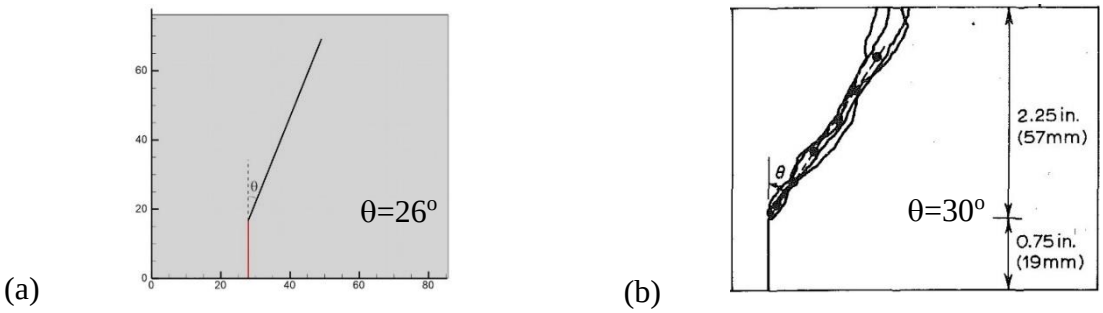

(a) (b)

Fig 4-7- Inclined crack propagation for γ=0.72 (a) numerical simulation, (b) experimental result [34]

Fig 4-8 shows the 2D and 3D representation of the crack pattern for both cases considered, i.e. γ=0.78 and γ=0.72. It should be emphasized that the results presented here are virtually independent of discretization, which stems from incorporation of the characteristic length χ, eq.(4-7).

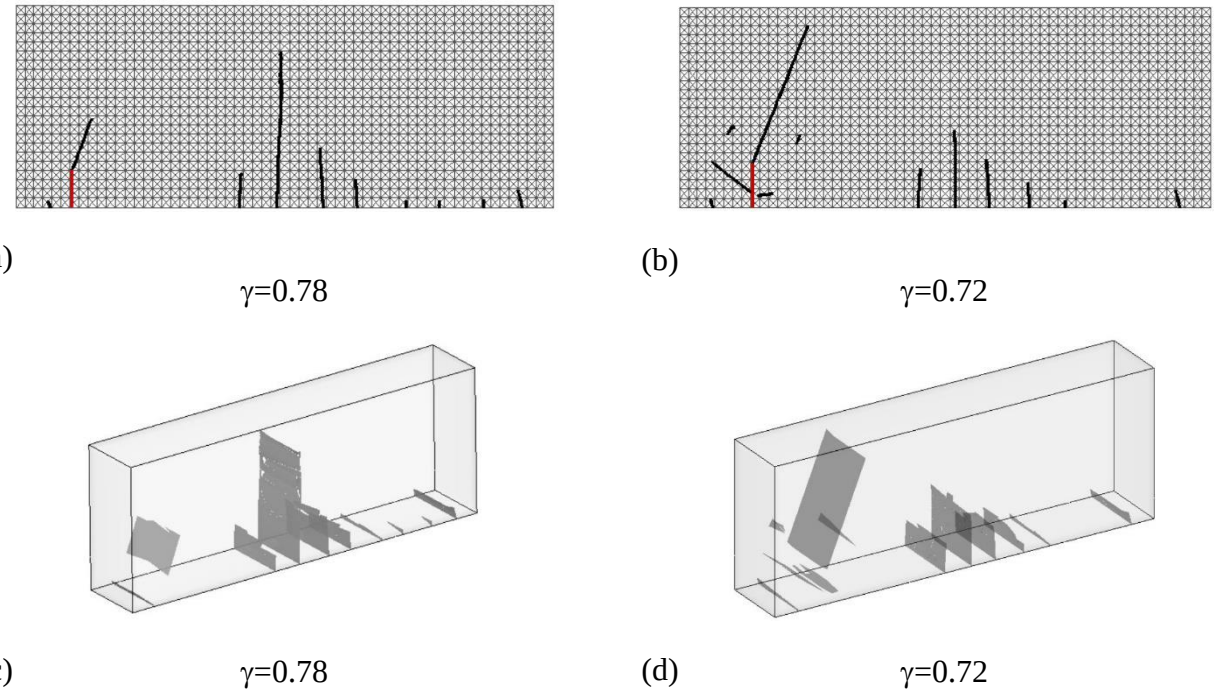

Fig 4-8- Crack trajectories for two different offset values in 2D and 3D

In order to demonstrate the ability of the proposed framework to model the fracture propagation in true 3D conditions, an additional example is provided. The example involves again a three-point bending; however, in this case the notch is inclined with respect to the loading direction. The beam has the span of 240mm, height of 60mm and 20mm depth, while the notch is at the center of the span and penetrates the beam depths at 45o (Fig. 9) . The actual geometry is taken from the work of Dhont et al. [36]; a similar problem, however, has also been addressed in other references (e.g. [37, 38]) using different loading conditions as well as different solution techniques. The latter included a modified virtual crack closure integral method [36], adaptive mesh refinement [37] as well as XFEM [38]. Here, the beam is discretized using approx. 32,000 tetrahedral elements with 63,000 nodes (Fig. 9b).

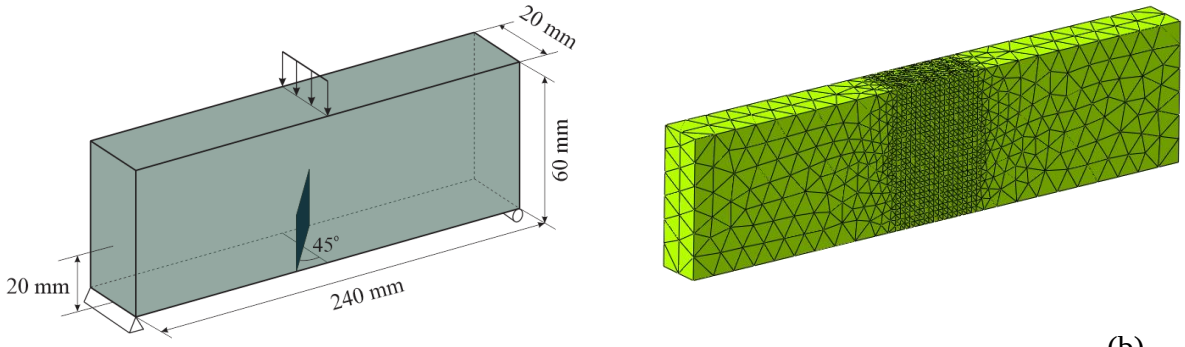

Fig 4-9-(a) Geometry of the notched beam (b) 3D Finite element discretization

The selected material properties are similar to those used in ref.[37], viz. $E=2300\ MPa$, $\nu=0.3$, $f_t=2.5MPa$, $G_f=0.10\ N/mm$ and $\alpha=0\ mm^{-1}$. The load is displacement-controlled and the crack propagation is traced using the smoothening algorithm described in Section 4. As the load increases, the crack propagation is associated with a progressive twist of the crack surface in the direction that is aligned with that of the prescribed displacements. The propagation pattern as well as the deformed configuration, corresponding to different stages of loading, are shown in Fig.10. The results are consistent with those reported in the references cited earlier

.

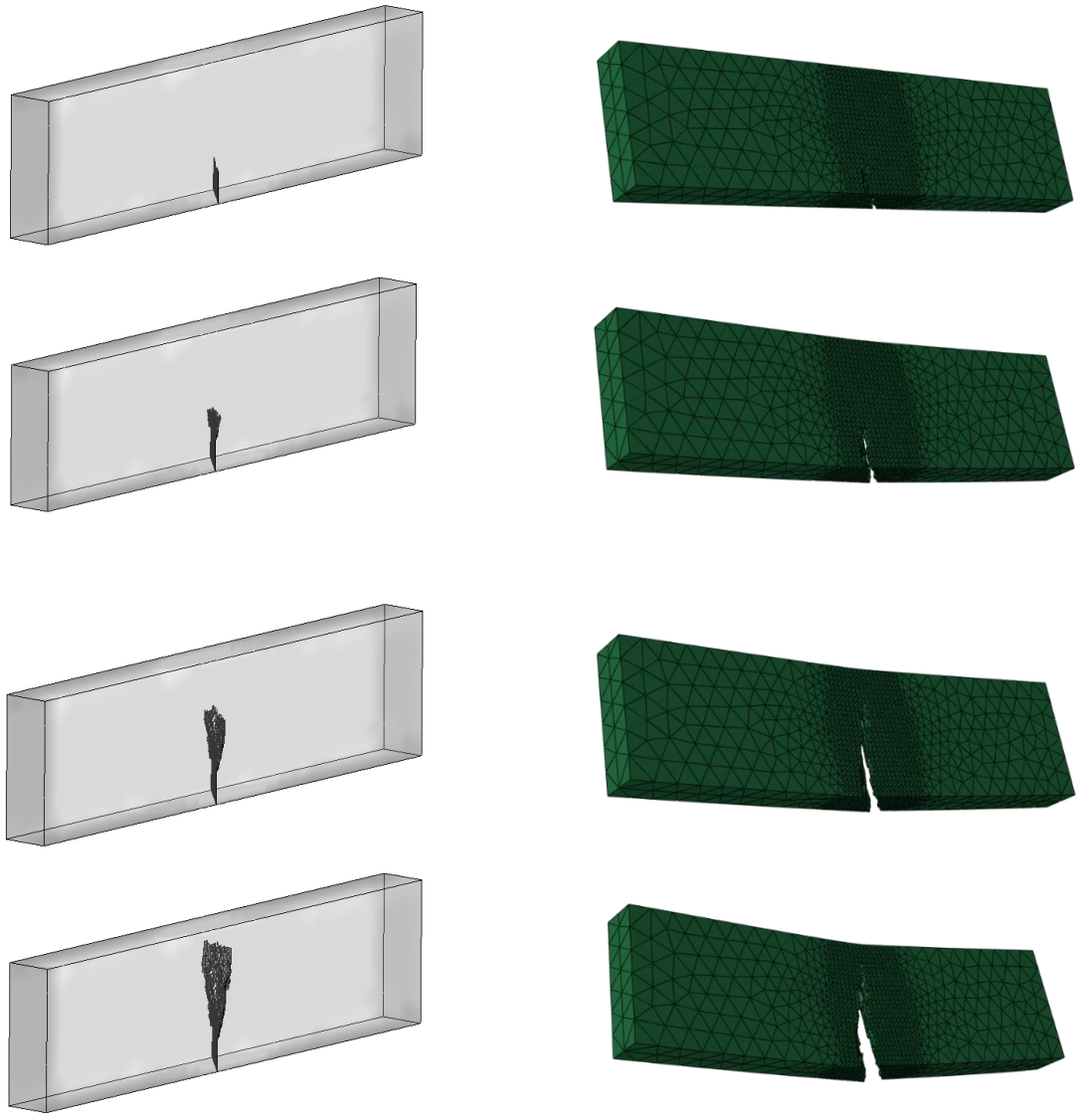

Fig 4-10- Crack path and deformed configuration of the beam at different loading stages

4.6.2 Three-point bending of a high-strength reinforced concrete beam

This example is focused on examining the effect of reinforcement in high strength concrete. The experimental data comes from work of Bosco et.al [39] who investigated the variation of ultimate strength of reinforced concrete beams as a function of volume fractions of steel rebars. In particular, a number of three-point bending tests were conducted on concrete with compressive

strength of *90 MPa* for 5 different sets of longitudinal reinforcement located in the tensile zone of the beam. The details on the steel reinforcement are provided in Table 4-1. All tested beams had a span of *600mm* with *100mm* height and *150mm* depth and the vertical load was applied in the middle of the span. The analysis was carried out using the following material properties for concrete

$$E_c = 34.3GPa, \quad \nu_c = 0.2, \quad f_c = 90\,MPa, \quad G_f = 60\ N/m\ , \quad \alpha = 14\ mm^{-1}$$

The tensile strength for concrete was assessed by employing the empirical formula given in ref.[40], i.e. $f_t \approx 0.54\sqrt{f_c}$, which gives: $f_t = 5.12\,MPa$. For steel rebars, the yield stress was assumed as f_y*=450MPa* while the modulus of elasticity was taken as E_s*=200 GPa*. As mentioned earlier, after the onset of localization the reinforcing bars are idealized as beams of a characteristic length *l*, rigidly embedded in the adjacent intact material. Thus, the length *l* affects the stiffness of the reinforcing network within the damaged region, cf. eqs.(4-17). In this work, the thickness of the fracture zone itself has been directly identified with the crack opening $\bar{w}_n$. This gives, in general, a conservative estimate of the stiffness of reinforcement. Note that the overall stiffness of the damaged zone is also affected by the fracture energy G_f, eq.(4-15), which controls the rate of softening of the damaged concrete.

In view of the symmetry in geometry and the loading conditions, only the half of the beam was analyzed, as shown schematically in Fig 4-11. For the 3D simulations, the structure was discretized using again the tetrahedral elements. The beam was divided into parts in which different properties were assigned, i.e. those of pure concrete and the homogenized properties of composite in the vicinity of the embedded reinforcement. The latter part is shown in red colour in Fig 4-12. Note that the volume fractions of reinforcement, as reported in Table 4-1, were assessed with respect to the selected volume of the composite part, which was taken as *7.75mm* thick and *50mm* wide. The problem was solved as displacement-controlled by incrementally increasing the vertical displacement in the middle of the span.

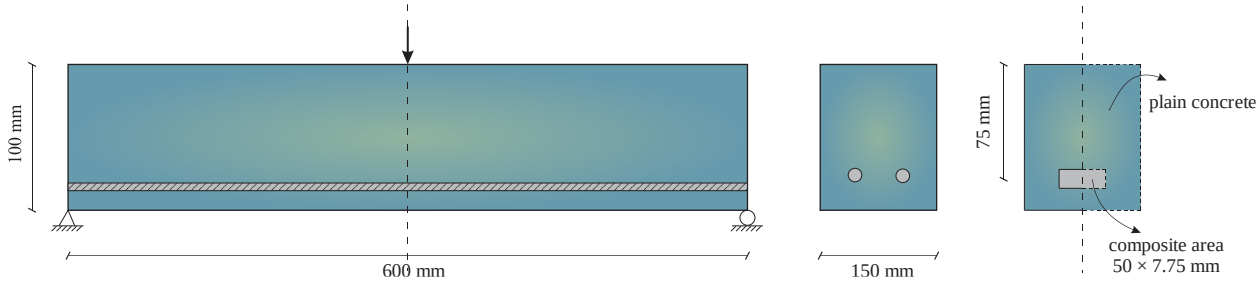

Fig 4-11- Geometry of the beam and the boundary conditions

Table 4-1- Properties of reinforced concrete beam for different cases

	Rebars (mm)	Area (mm^2)	ρ_1
Case1	0	0.0	0.0
Case2	*1ϕ 4*	12.5	0.03
Case3	*2ϕ 5*	39.2	0.11
Case4	*2ϕ 8*	100.5	0.26
Case5	*2ϕ 10*	157.0	0.41

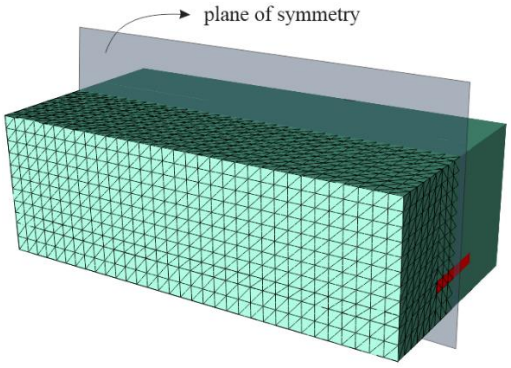

Fig 4-12- 3D discretization with tetrahedral elements

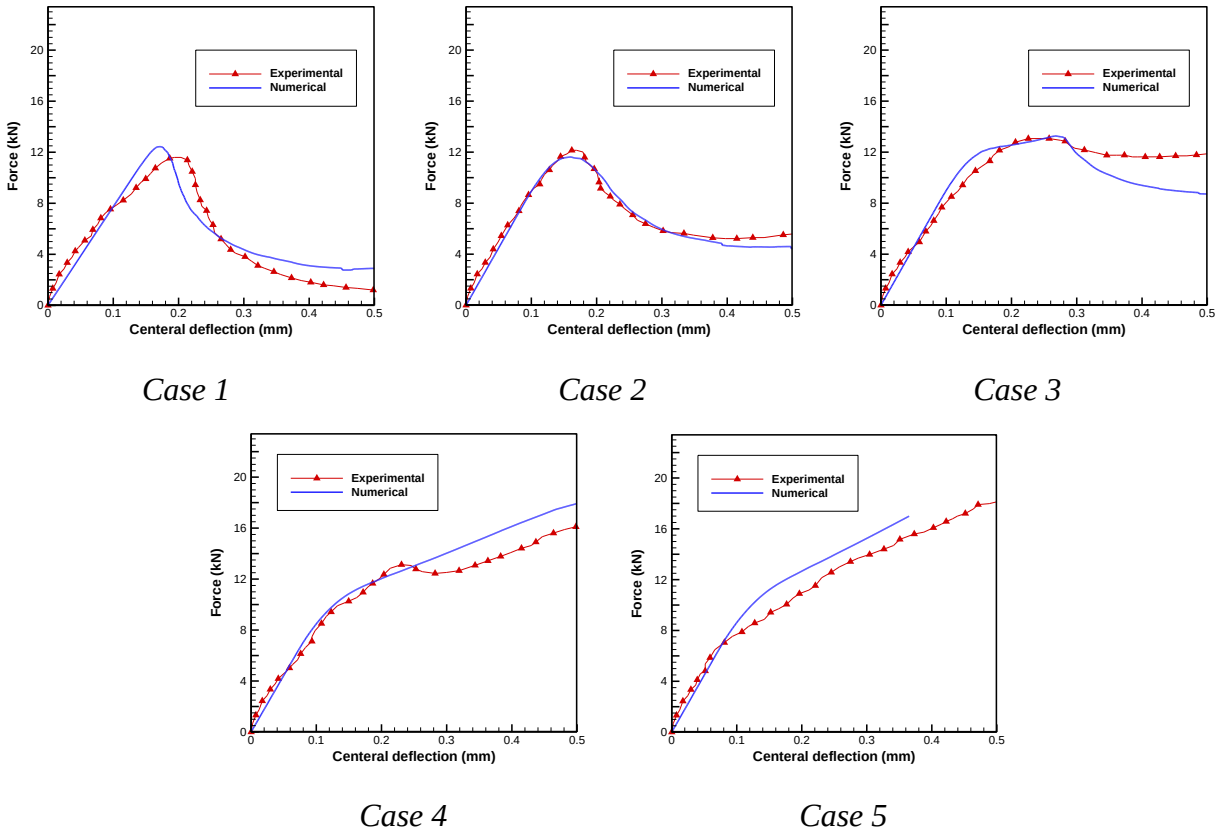

Fig 4-13- The load-displacement curves for different volume fractions of reinforcement

Fig 4-13 shows the load-displacement curves for different volume fractions of reinforcement. The results are compared with the experimental data reported in ref.[39]. Case 1 corresponds to plain concrete and it's associated with an unstable response after reaching the peak. A qualitatively similar characteristic is obtained for a low intensity of reinforcement (Case 2). In Case 3, the yielding of reinforcement in the fractured zone takes place when the load approaches its ultimate value. In the last two cases, after formation of a macrocrack in concrete, the reinforcement is initially in the elastic range which results in an increase of strength and ductility of the beam.

4.6.3 Crack propagation in a heavily reinforced concrete beam

The last set of simulations reported here pertains to the assessment of crack propagation in a four-point bending of a heavily reinforced deep concrete beam. The experimental data is taken from the work of Leonhardt and Walther [41]. The geometry of the problem and the boundary conditions are provided in Fig 4-14. Three different cases were considered corresponding to different lengths and shear spans, *a*, as defined in Table 4-2. For all these cases, the height of the beams was *320mm* and the reinforcement consisted of two longitudinal steel bars#26 that were located in the tensile region at the effective depth of *270 mm*.

Table 4-2- details of beams dimensions

	Beam length	*Shear span (a)*
Case 1	*900 mm*	*270 mm*
Case 2	*1160 mm*	*400 mm*
Case 3	*1440 mm*	*540 mm*

In the numerical simulations, the thickness of the composite zone was assumed to be *20 mm*, and the corresponding volume fraction of reinforcement in this zone was calculated as $\rho_1 = 0.28$. Again, given the symmetry in boundary conditions, only a half of the beam was analyzed and the discretization employed tetrahedral elements. For all cases considered, the following material properties were employed after ref. [41].

$$E_c = 20\,GPa, \quad \nu = 0.2, \quad f_t = 2.2\,MPa, \; E_s = 200\,GPa, \; f_y = 430\,MPa, \; \alpha = 14\,mm^{-1}$$

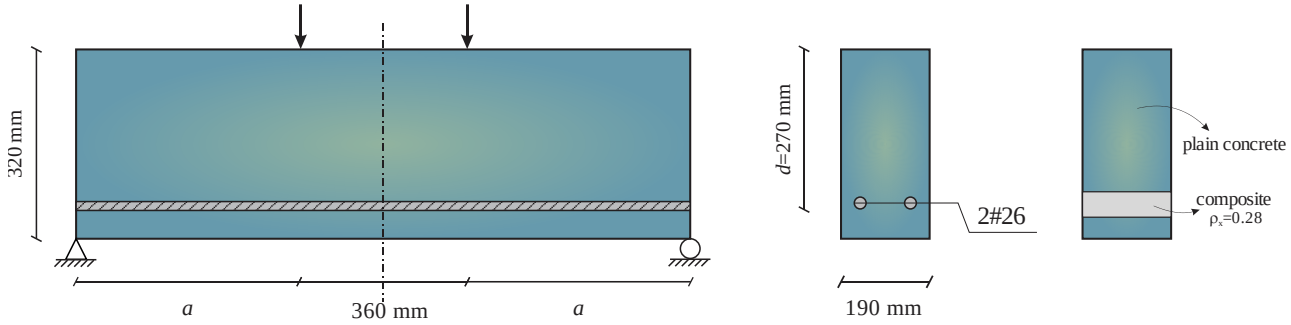

Fig 4-14- Geometry of the deep beam and the position of reinforcement

Based on elementary bending theory, the mid-span of beam is shear free whereas the bending moment in this region is maximum. In contrast, the sides of the beam are subjected to maximum shear while the bending moment is increasing linearly up to its maximum value at the end of the shear span. As the load increases, flexural cracks initiate in the middle of beam; however, their propagation is constrained due to the presence of reinforcement. As the shear stress increases within the shear span, the diagonal cracks start to appear. The evolution of crack pattern within the beam, as a function of increasing load, is depicted in Fig 4-15. The results are consistent with the experimental data of ref. [41].

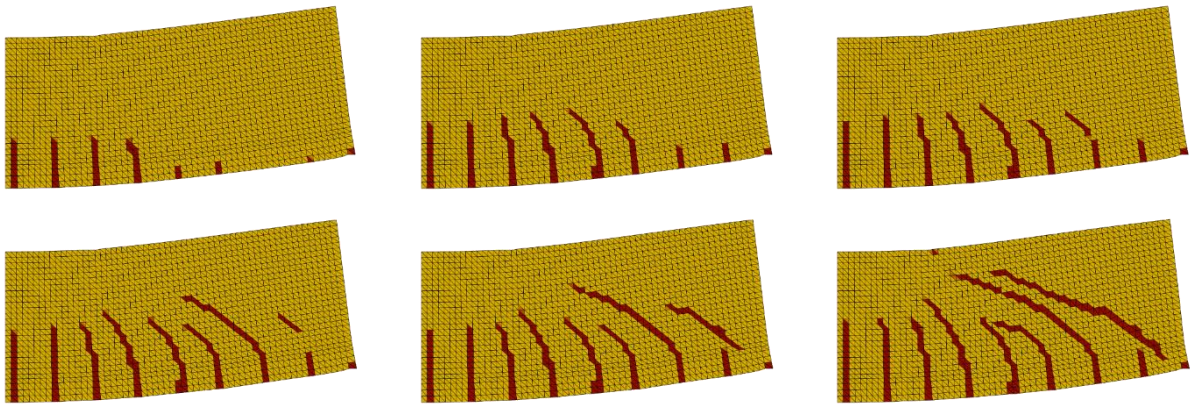

Fig 4-15- Evolution of crack pattern (Case#3)

It is noted that in the experimental tests the shear cracks start to appear close to the ultimate load and propagate very fast, triggering a debonding of the reinforcement along the interface. As suggested by Oliver et.al [16] this effect can be accounted for, in a simplified way, by assuming that the strength of rebars degrades after yielding (strain-softening). A similar approach was implemented here in order to trace the unstable post-peak response in the load-deflection characteristics. Such a characteristic is shown in Fig 4-16a for the geometry associated with case#3. The results correspond to $\omega = 1.02$, eq.(4-21), and are, in general, fairly consistent with the experimental evidence, i.e. the ultimate load is approximately *230 kN* and it is attained at the midspan deflection of *4 mm* (Fig 16.a). It needs to be pointed out though that the experiments were conducted under load-controlled conditions so that the post-peak response could not have been traced.

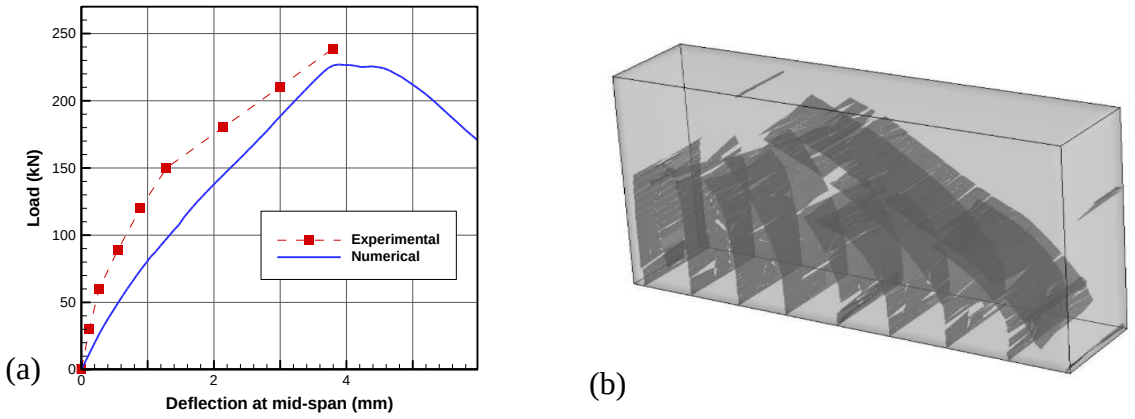

Fig 4-16- (a) Load-displacement curve for case# 3; (b) the corresponding 3D crack pattern (Case 3)

At this point, it may be of interest to examine the influence of both the value of parameter ω as well as the size of composite zone on the numerical solution. For this purpose, a set of parametric studies have been conducted. The analysis employed the values of ω within the range 1.0-1.02, and different thickness of the composite zone d_c. The latter was selected as being equal to 20mm, 30mm, 40mm and 50mm resulting in the corresponding values of the volume fraction of reinforcement of 0.28, 0.19, 0.14 and 0.11, respectively. The numerical results of these parametric studies are presented in Fig.17. It is evident that $\omega = 1.0$ gives a perfectly plastic response at the macroscale upon the yielding of reinforcement. At the same time, $\omega > 1$ (in this case 1.01 or 1.02)

triggers an unstable (softening) response that can be attributed to debonding in the area adjacent to the crack. It is noted that the value of ω has no effect here on the ultimate strength. The results in Fig.17b, which depict the influence of the thickness of the homogenization region, clearly show that the solution is virtually invariant with respect to the latter. In this case, neither the stiffness nor the ultimate load are affected by the value of d_c.

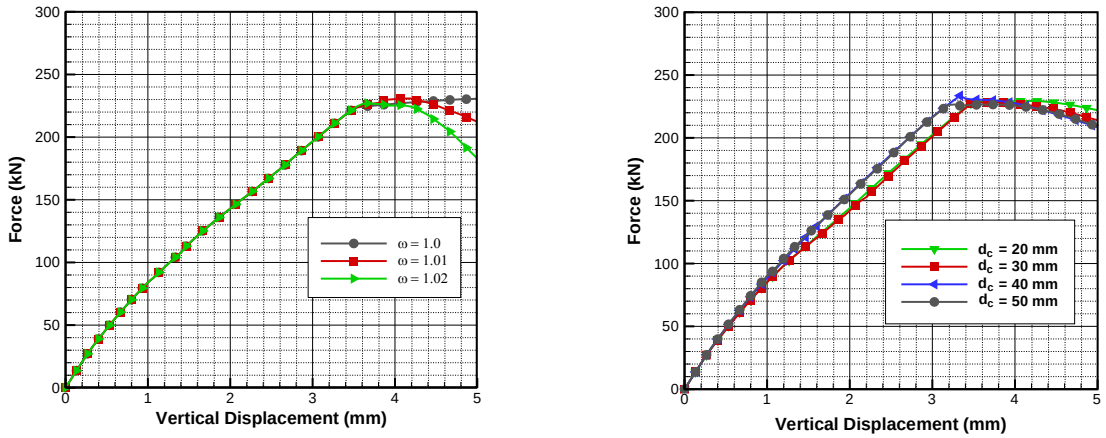

Fig 4-17- Results of parametric studies; influence of (a) the parameter ω, eq.(4-21) and (b) the thickness of the composite zone d_c

Fig 4-18 shows the predicted crack patterns in relation to the experimental results, for all cases considered. It is evident that for low aspect ratios, *a/d*, the shear cracks are dominant. However, as the shear span increases more flexural cracks form. In either case, the propagation of shear cracks controls the conditions at failure in the beam. It is worth mentioning that for all cases the shear cracks propagate from the support towards the point at which the load is applied.

Case 1

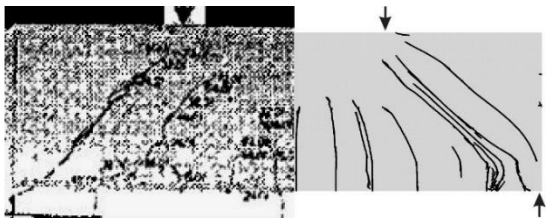

Case 2

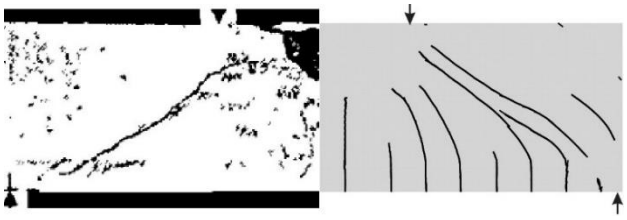

Case 3

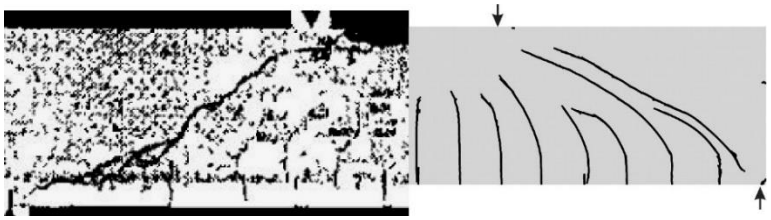

Fig 4-18- Comparison of cracking patter; numerical simulations (right) and experimental results(left)

4.7 Conclusions

In this paper, the volume averaging scheme was employed to simulate the response of reinforced concrete structures. The mathematical framework was presented for two different cases, i.e. homogeneous deformation prior to onset of discontinuity and the localized deformation mode. In the former case, some explicit static/kinematic constraints were imposed on the constituents' behavior that enabled the specification of the tangential stiffness operator. The latter was defined as a function of volume fractions and properties of both constituents.

The major part of this work was focused on the description of propagation of macrocracks in the reinforced concrete domain. A simplified volume averaging methodology was again employed to model the presence of a strong discontinuity. Within this approach, the formation of crack subdivides the considered referential volume into intact material and the fractured zone. The interfacial properties have been defined by relating the rate of traction to velocity discontinuity and an implicit integration scheme was outlined to enforce the continuity of traction along the interface. The strategy for tracing the crack propagation in 3D was also outlined.

It was noted earlier that this approach bears some similarities to the SDA framework employed by Oliver et al. [16]. However, there are several fundamental differences. The primary conceptual difference lies in addressing the issue of the response after the onset of discontinuity. In ref.[16], the strain-softening effects are attributed to the mechanical behaviour of the matrix and the softening modulus is treated as a material property enhanced by a regularization parameter. The latter, however, has no explicit physical definition. The crack path is not traced in a discrete manner but, instead, it's identified from displacement contour lines. In the current approach, the softening is attributed to discontinuous response within the damaged zone which, as mentioned earlier, is defined via the velocity jump vs. the rate of traction relation. At the macroscale, the framework incorporates a 'characteristic length' χ, eq.(7), which has a unique definition (i.e. ratio of the surface area of discontinuity to the referential volume) and the crack path as well as the discontinuity pattern are traced in a discrete way, similar to that employed in XFEM.

Some differences are also evident in the description of homogeneous deformation, prior to localization. In ref. [16], all constituents are assumed to be subjected to the same strain rate throughout all stages of the deformation process. The behaviour of concrete matrix is described using an isotropic damage model, while the reinforcement and the interface are modeled by invoking uniaxial tensile and shear characteristics. In the present approach, *both* kinematic and static constraints are imposed on constituents during the homogeneous deformation stage, and the stress/strain rates are defined via the volume averaging.

The main contribution in this work was the implementation of the proposed methodology in a series of boundary value problems that involved modeling of reinforced concrete structures in the presence of evolving discontinuities. The predictive abilities of the framework were examined for different boundary conditions and intensities of reinforcement and the results were compared with the experimental evidence. It was shown that the outlined methodology is quite adequate in capturing the propagation of macrocracks in reinforced concrete domains. It should also be pointed out that the approach pursued here is much simpler in implementation as compared to XFEM. This issue was explicitly addressed in ref.[20-23], quoted earlier in the text. It was demonstrated there that the present framework gives results that are nearly identical to those obtained using Extended FEM, while the computational effort is significantly reduced. The latter stems from the fact that in

XFEM the discontinuity is introduced explicitly into the discretized system by employing enrichments in shape functions and additional degrees of freedom. These enhancements significantly impair the numerical efficiency as compared to the present methodology which uses standard FEM interpolations.

4.8 Appendix

In this appendix, a set of explicit kinematic and static constraints is provided, which is required to establish the components of the operators **B** defined in eq.(4-2). It is noted that an analytical expression for these matrices was derived in ref.[24] for the case of two orthogonal sets of steel bars embedded in concrete. Here, these constraints are modified in order to extend this framework to include a set of three families of reinforcement. Referring the problem to the local coordinate system along the respective families of rebars, Fig 4-19, and assuming a perfect bonding between the constituents, the following kinematic constrains imposed on axial strain need to be satisfied

$$\dot{\bar{\varepsilon}}_{11}^{(c)} = \dot{\bar{\varepsilon}}_{11}^{(1)}; \quad \dot{\bar{\varepsilon}}_{22}^{(c)} = \dot{\bar{\varepsilon}}_{22}^{(2)}; \quad \dot{\bar{\varepsilon}}_{33}^{(c)} = \dot{\bar{\varepsilon}}_{33}^{(3)} \tag{4-26}$$

The static constraints stem from the requirements of equilibrium and take the form

$$\begin{gathered} \dot{\bar{\sigma}}_{ij}^{(c)} = \dot{\bar{\sigma}}_{ij}^{(1)} = \dot{\bar{\sigma}}_{ij}^{(2)} = \dot{\bar{\sigma}}_{ij}^{(3)}; \quad \textit{for } i,j = 1,2,3 \quad i \neq j \\ \dot{\bar{\sigma}}_{11}^{(c)} = \dot{\bar{\sigma}}_{11}^{(2)} = \dot{\bar{\sigma}}_{11}^{(3)}; \quad \dot{\bar{\sigma}}_{22}^{(c)} = \dot{\bar{\sigma}}_{22}^{(1)} = \dot{\bar{\sigma}}_{22}^{(3)}; \quad \dot{\bar{\sigma}}_{33}^{(c)} = \dot{\bar{\sigma}}_{33}^{(1)} = \dot{\bar{\sigma}}_{33}^{(2)} \end{gathered} \tag{4-27}$$

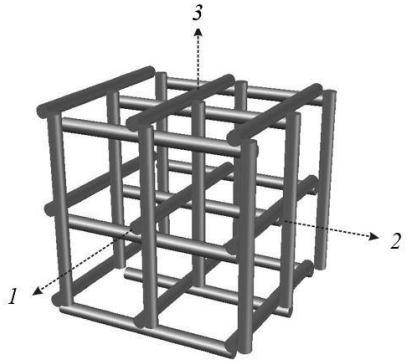

Fig 4-19- Reinforcement in 3D in the local coordinate system

Following now the methodology outlined in ref.[24], i.e. incorporating constraints (4-26) and (4-27) in the averaging scheme (4-1), the strain rates in constituents can be obtained, viz. eq.(4-2),

thereby identifying the individual components of operators $\mathbf{B_i}$. The analytical form of these expressions is too complex to be presented here. In practical terms, given the properties of each constituent, the components of $\mathbf{B_i}$ can be assessed numerically and stored at the beginning of analysis to save the computational cost.

4.9 References

1. Coronelli D, Mulas MG. Modeling of shear behavior in reinforced concrete beams. *ACI Structural Journal* 2006; **103**: 372.
2. Vecchio F , Collins M. The response of reinforced concrete to in-plane shear and normal stresses. *Pub. No. 82-03, University of Toronto* 1982;
3. Bhide SB, Collins MP. Influence of axial tension on the shear capacity of reinforced concrete members. *ACI Structural Journal* 1989; **86**: 570-581.
4. Krefeld WJ, Thurston CW. Studies of the shear and diagonal tension strength of simply supported reinforced concrete beams. *Journal Proceedings* 1966; **63**:451-476.
5. Mphonde AG, Frantz GC. Shear tests of high-and low-strength concrete beams without stirrups. *ACI Journal* 1984; **81**: 350-357.
6. Isenberg J. Finite element analysis of reinforced concrete structures II. 1993;
7. Ngo D, Scordelis A. Finite element analysis of reinforced concrete beams. *ACI Journal* 1967; **64**:152-163.
8. Suidan M, Schnobrich WC. Finite element analysis of reinforced concrete. *Journal of the Structural Division* 1973; **99**: 2109-2122.
9. Stevens N, Uzumeri S, Will G. Constitutive model for reinforced concrete finite element analysis. *Structural Journal* 1991; **88**: 49-59.
10. Feenstra PH, De Borst R. Constitutive model for reinforced concrete. *Journal of Engineering Mechanics* 1995; **121**: 587-595.
11. Cervenka V. Constitutive model for cracked reinforced concrete. *Journal Proceedings* 1 985; **82**:877-882.
12. Pang X-B, Hsu TT. Fixed angle softened truss model for reinforced concrete. *ACI Structural Journal* 1996; **93**: 197-207.

13. Pang X-BD, Hsu TT. Behavior of reinforced concrete membrane elements in shear. *ACI Structural Journal* 1995; **92**: 665-679.

14. Oliver J. Modelling strong discontinuities in solid mechanics via strain softening constitutive equations. Part 1: Fundamentals. *International Journal for Numerical Methods in Engineering* 1996; **39**: 3575-3600.

15. Simo JC, Oliver J, Armero F. An analysis of strong discontinuities induced by strain-softening in rate-independent inelastic solids. *Computational Mechanics* 1993; **12**: 277-296.

16. Oliver J, Linero DL, Huespe AE, Manzoli OL. Two-dimensional modeling of material failure in reinforced concrete by means of a continuum strong discontinuity approach. *Computer Methods in Applied Mechanics and Engineering* 2008; **197**: 332-348.

17. Belytschko T, Black T. Elastic crack growth in finite elements with minimal remeshing. *Int. J. Numer. Meth. Eng* 1999; **45**: 601-620.

18. Dolbow J, Belytschko T. A finite element method for crack growth without remeshing. *Int. J. Numer. Meth. Eng* 1999; **46**: 131-150.

19. Khoei AR. *Extended finite element method: theory and applications*. John Wiley & Sons: 2014.

20. Wells GN, Sluys LJ. A new method for modelling cohesive cracks using finite elements. *International Journal for Numerical Methods in Engineering* 2001; **50**: 2667-2682.

21. Moës N, Belytschko T. Extended finite element method for cohesive crack growth. *Engineering Fracture Mechanics* 2002; **69**: 813-833.

22. Asferg J.L, Poulsen P.N, Nielsen L.O, A consistent partly cracked XFEM element for cohesive crack growth. *Int. J. Numer. Meth. Eng* 2007; **72**: 464-485.

23. Mohammadnejad T, Khoei A.R, An extended finite element method for hydrulic fracture propagation in deformable porous media with the cohesive crack model. *Finite Elements in Analysis and Design* 2013; **73**: 77-95.

24. Pietruszczak S, Winnicki A. Constitutive model for concrete with embedded sets of reinforcement. *Journal of Engineering Mechanics-Asce* 2003; **129**: 725-738.

25. Haghighat E, Pietruszczak S. On modeling of discrete propagation of localized damage in cohesive-frictional materials. *International Journal for Numerical and Analytical Methods in Geomechanics* 2015; **39** : 1774-1790.

26. Pietruszczak S, Mroz Z. Finite-element analysis of deformation of strain-softening materials. *International Journal for Numerical Methods in Engineering* 1981; **17**: 327-334.

27. Hill R. Elastic properties of reinforced solids: Some theoretical principles. *Journal of the Mechanics and Physics of Solids* 1963; **11**: 357-372.

28. Pietruszczak S. On homogeneous and localized deformation in water-infiltrated soils. *International Journal of Damage Mechanics* 1999; **8**: 233-253.

29. Przemieniecki JS. *Theory of matrix structural analysis*. Courier Corporation: 1985

30. Horne MR. *Plastic theory of structures: In si/metric units*. Elsevier: 2014

31. Caggiano A, Etse G, Martinelli E. Zero-thickness interface model formulation for failure behavior of fiber-reinforced cementitious composites. *Computers & Structures* 2012; **98**: 23-32.

32. Cavaco E.S, Casas J.R, Neves L.C, Huespe A.E, Robustness of corroded reinforced concrete structures – a structural performance approach. *Structural and infrastructure Engineering* 2013; **9**: 42-58.

33. Gasser TC, Holzapfel GA. 3d crack propagation in unreinforced concrete.: A two-step algorithm for tracking 3d crack paths. *Computer Methods in Applied Mechanics and Engineering* 2006; **195**: 5198-5219.

34. John R, Shah SP. Mixed-mode fracture of concrete subjected to impact loading. *Journal of structural engineering* 1990; **116**: 585-602.

35. Song JH, Areias P, Belytschko T. A method for dynamic crack and shear band propagation with phantom nodes. *International Journal for Numerical Methods in Engineering* 2006; **67**: 868-893.

36. Dhondt G, Chergui A, Buchholz F.G, Computational fracture analysis of different speciements regarding 3D and mode coupling effects. *Engineering Fracture Mechanics* 2001; **68**: 383-401

37. Moslemi H, Khoei A.R, 3D adaptive finite element modeling of non-planar curved crack growth using the weighted superconvergent path recovery method. *Engineering Fracture Mechanics* 2009; **76**: 1703-1728.

38. Gravouil A, Moes N, Belytschko T, Non-planar 3D crack growth by the extended finite element and level sets-Part II: level set update. *International Journal for Numerical Methods in Engineering* 2002; **53**: 2569-2586.

39. Bosco C, Carpinteri A, Debernardi PG. Minimum reinforcement in high-strength concrete. *Journal of structural engineering* 1990; **116**: 427-437.

40. Carrasquillo RL, Nilson AH, Slate FO. Properties of high strength concrete subject to short-term loads. *Journal Proceedings* 1981; **78**:171-178.

41. Leonhardt F, Walther R. The stuttgart shear tests. *Cement & Concrete Association Library* 1961; 49-54.

5 Numerical analysis of damage propagation in large scale structures affected by ASR

This chapter provides an illustration of application of the methodology described earlier, viz. the chemo-plasticity framework coupled with embedded discontinuity approach, to the numerical analysis of a large scale structure. The scope of the work involved a series of enhancements in the mathematical framework itself and its implementation in the FE code (COSMOS and Abaqus) to simulate the behavior of a hydraulic power plant structure over its life span. In view of a high computational cost of the analysis, the crack propagation was monitored in a 'smeared' sense (i.e. smoothing algorithm was not employed); instead, the parallel computing algorithm was implemented to increase the speed of simulations. This work has been performed in cooperation with Hydro-Quebec and was focused on examining the damage distribution in the water intake structure, located along Saint-Maurice river in Quebec, over the period of 100 years of continuing ASR. The contribution of Dr. Gocevski and Mr. Yildiz from Hydro-Quebec, in terms of discretization of the structure and specification of material properties, is gratefully acknowledged. In what follows a brief review of the simulations and the key numerical results are provided.

5.1 Introduction

Over the last few decades, a significant amount of research has been devoted to physicochemical aspects of ASR in concrete and its influence on the behavior of existing structures [1,2]. In parallel with these investigations, a number of experimental studies have been carried out examining the kinetics of the reaction and the associated degradation of material properties. The research on the development of constitutive models describing the chemo-mechanical interaction started to appear in the mid 1990's. The first continuum approach, involving the framework of chemo-plasticity/elasticity, was presented in ref. [3]. Later, several other concepts were proposed [4-9]

including a micromechanical descriptions of ASR-induced deformation [10-11]. It needs to be pointed out that the more recent developments deal with plain concrete only and are, in general, inadequate in terms of modelling of localized deformation, which is intrinsic in the type of problems considered here. Furthermore, there have only been a few isolated attempts to perform large-scale simulations that involved the actual engineering structures. Most of these attempts [8,12] dealt primarily with the assessment of the influence of concrete expansion on the structural integrity, without accounting for the reaction-dependent evolution of material properties and a rather simplistic description of the onset and propagation of localized damage, particularly in compression regime. On the other hand, the chemo-plasticity framework outlined in ref. [3] has been applied, as early as 1995, to analysis of various Hydro-Quebec structures including the primary and auxiliary structures of Beauharnois powerplant [13, 14] and the results have been verified against the in-situ measurements.

The mathematical formulation employed here follows the approach outlined in chapters 2 and 3. The reinforcement is considered in a discrete manner using embedded 1D elements. In what follows, the description of the geometry of the problem and the main results pertaining to evolution of damage due to continuing ASR are provided.

5.2 Numerical Simulations

The primary objectives of the numerical studies reported below have been (a) to evaluate the present state of damage within the structural components that are affected by ASR and (b) to examine the possibility of prolonging the life span of the structure during which an uninterrupted production can be maintained. For simulating the intake structure, the standard Abaqus software was used to generate the FE model, while the chemo-plasticity framework was implemented via Abaqus VUMAT subroutine. The geometry of the analyzed structure is show in Fig 5-1. It is noted that the entire hydraulic structure consists of two main sections, i.e. the spillway and the power house with six turbines for generating electricity. The length of the structure is approximately 250m with the height of 50m.

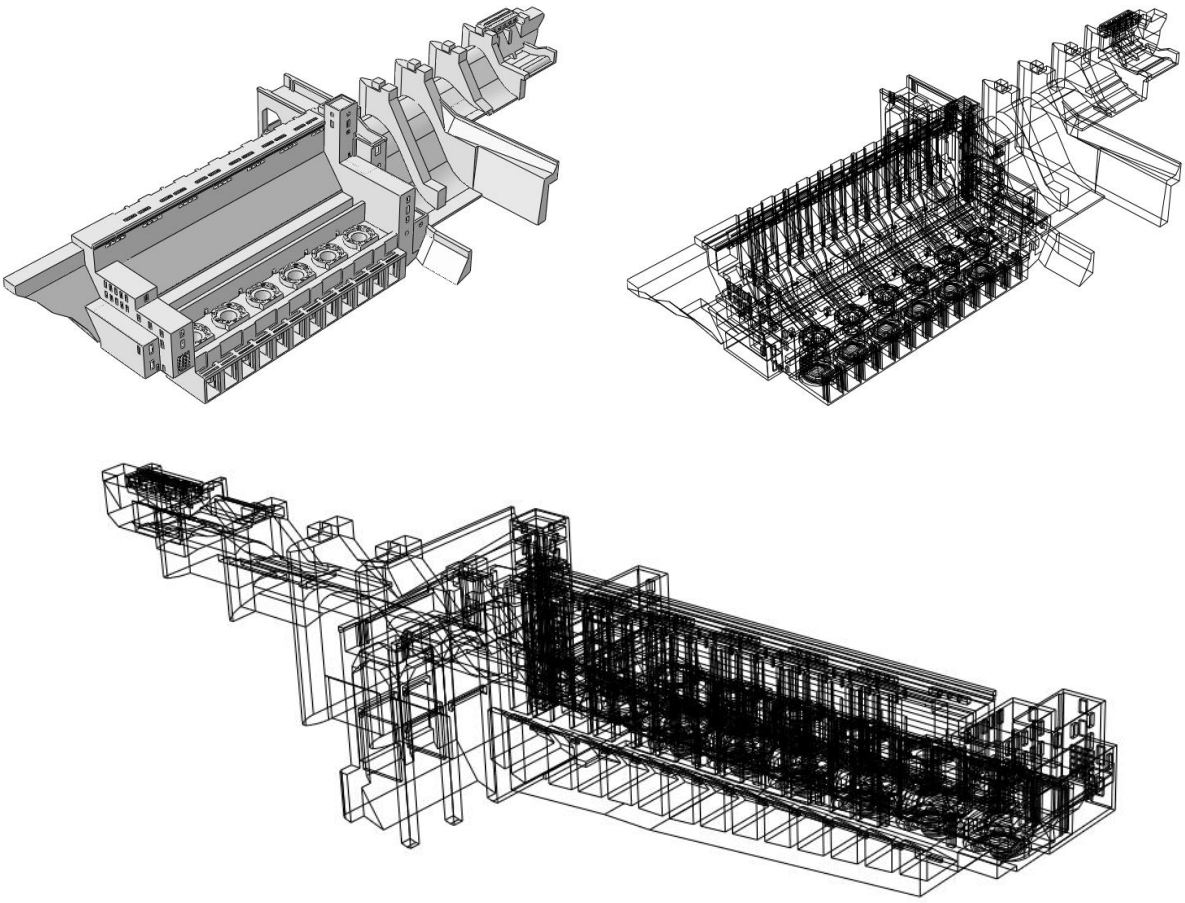

Fig 5-1- Geometry of the analyzed hydroelectric power plant structure in different views

The structure itself is founded on a hard rock that is considered as an elastic medium. The simulations were conducted in two main stages, viz. gravity load followed by continuing ASR, and included the effect of confinement and humidity on the rate of reaction. For discretizing the domain, about 400,000 tetrahedral elements with 740,000 nodes were used and the key material properties are provided in Table 5-1.

In order to increase the numerical efficiency of the simulations, some simplification have been introduced. In particular, the onset of localized deformation in both compression and tension regime was assumed to take place when the value of the strength parameter η (see eq. (3-4)) approached unity (i.e. η=0.99). Moreover, the shear band was assumed to form at the geometric center of the element and its discrete propagation (via. the smoothing algorithm) has not been

traced. Owing to those simplification, parallel processing was employed which significantly increased the speed of analysis.

Table 5-1- Material properties of concrete

Concrete modulus of elasticity	17.0 GPa
Concrete Poison's ratio	0.18
Concrete compressive strength	30 MPa
Concrete tensile strength	2 MPa
Concrete density	2400 kg/m^3
Fracture energy	100 N/m
Chemical expansion rate	60 µm/year

The results presented below focus on the water intake structure within the complex shown in Fig.5.1. The simulations cover the period of 100 years. The reaction is assumed to have started 5 years after the construction of the intake structure. The three-dimensional FE discretization is shown in Fig. 5.2. The same figure shows the position of section A, which is selected here to present the details on the time-history of deformation process. This is one of the critical sections where the turbines are located.

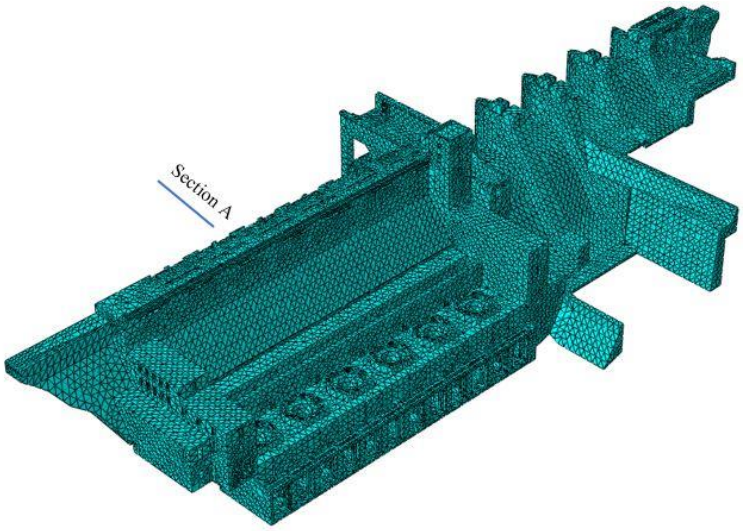

Fig 5-2- Three-dimensional discretization and the position of section A

As mentioned earlier, the simulations were conducted in two main stages, viz. gravity load and continuing ASR, and included the effect of confinement and humidity on the rate of reaction. During the simulations the accumulated plastic distortion was stored within each element to assess the onset of damage. The direction of crack was calculated based on the local stress state, as discussed in Chapter 3. After formation of discontinuity, the cohesive law (viz. eq. (3-41) and eq. (3-49)) was used to describe the behavior within the fractured zone.

The main results of the analysis, including the displacement field and the damage distribution during 100 years of the continuing chemical reaction, are provided in figures below. Note that the simulations employing parallel processing took about 6-hours on a computer with 16 cores.

Fig 5-3 shows the distribution of displacement magnitudes, within the section A, at the end of analysis. To verify the accuracy of the simulations, the obtained results are compared in Fig 5-4 with the in-situ measurements. The latter were recorder at the crest of the structure in both in vertical and horizontal directions. The agreement between the instruments readings and the calculated values is fairly consistent.

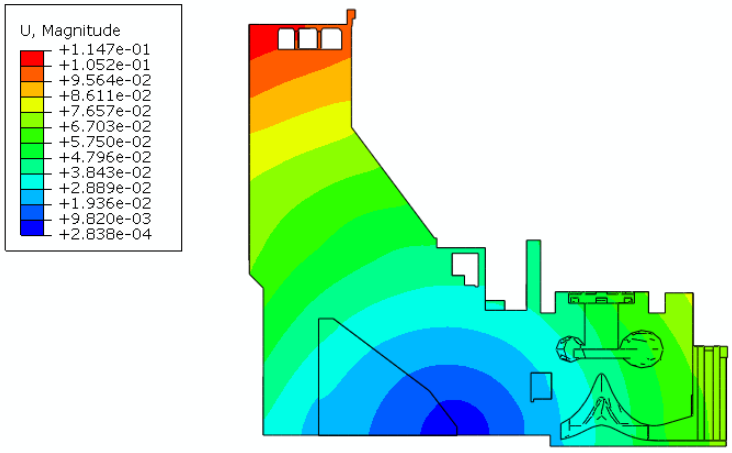

Fig 5-3- Displacement field in section A after 100 years (units in meters)

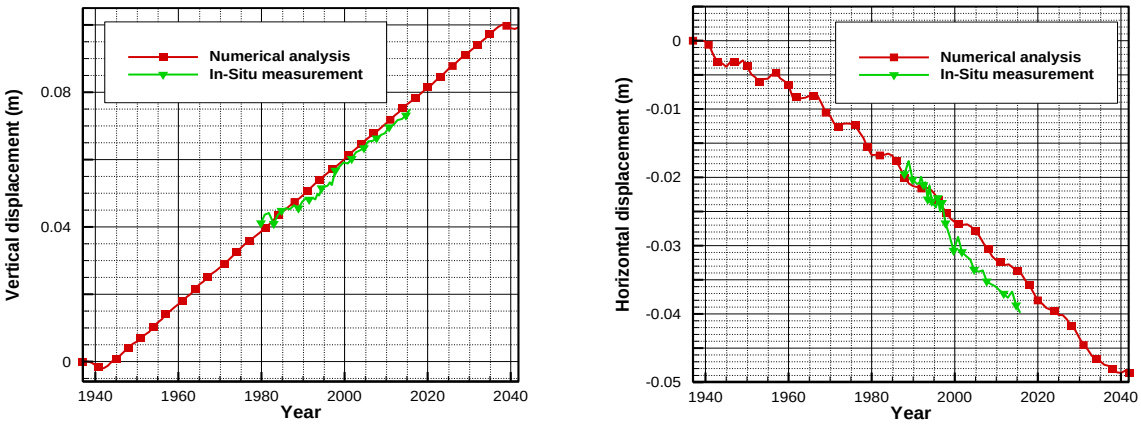

Fig 5-4- Time history of displacement at the crest of the structure (comparison with in-situ measurements)

The damage pattern, at the end of the analysis, is shown in Fig. 5.5. The figure presents the distribution of damage (in two different views) along the surface of the structure. Here, the value of $\eta \to 1$ (i.e., SDV2=1) is indicative of the onset of formation of macrocracks, while the values exceeding one (shades of red color) signify the highest intensity of damage within the domain. In general, the extent and location of damage visible on the surface of the intake structure, is consistent with the in-situ observation.

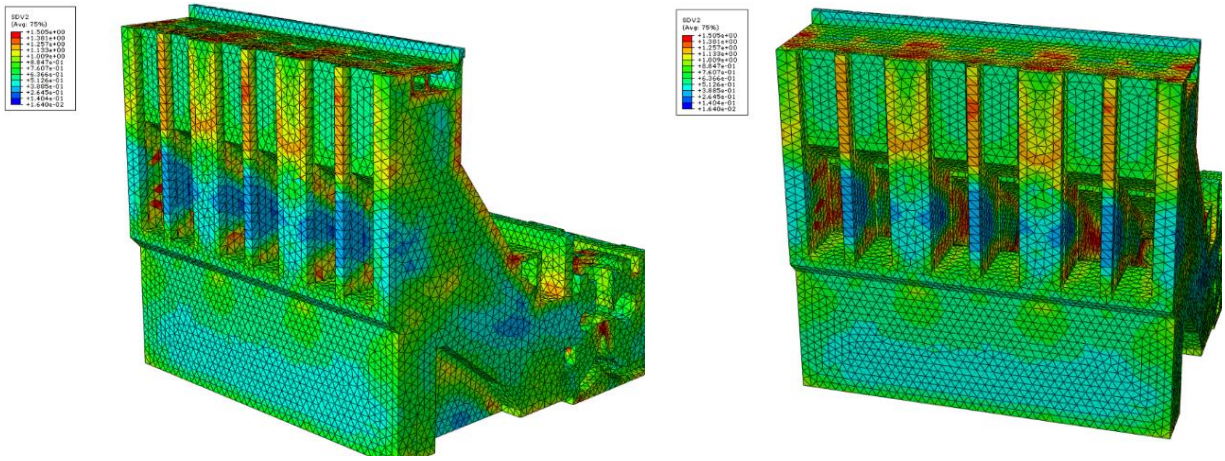

Fig 5-5- Displacement and damage distribution at the end of analysis in different views

Finally, Fig. 5.6 shows the growth of damage within the section A. The results correspond to the time interval from 10 to 100 years. It is evident that the damage is largely confined to the region near the surface, so that the overall stability of the structure is not directly affected. Similar conclusions can, in general, be drawn by analyzing the results for other sections along the length of structure. These results are qualitatively similar and are not shown here for brevity.

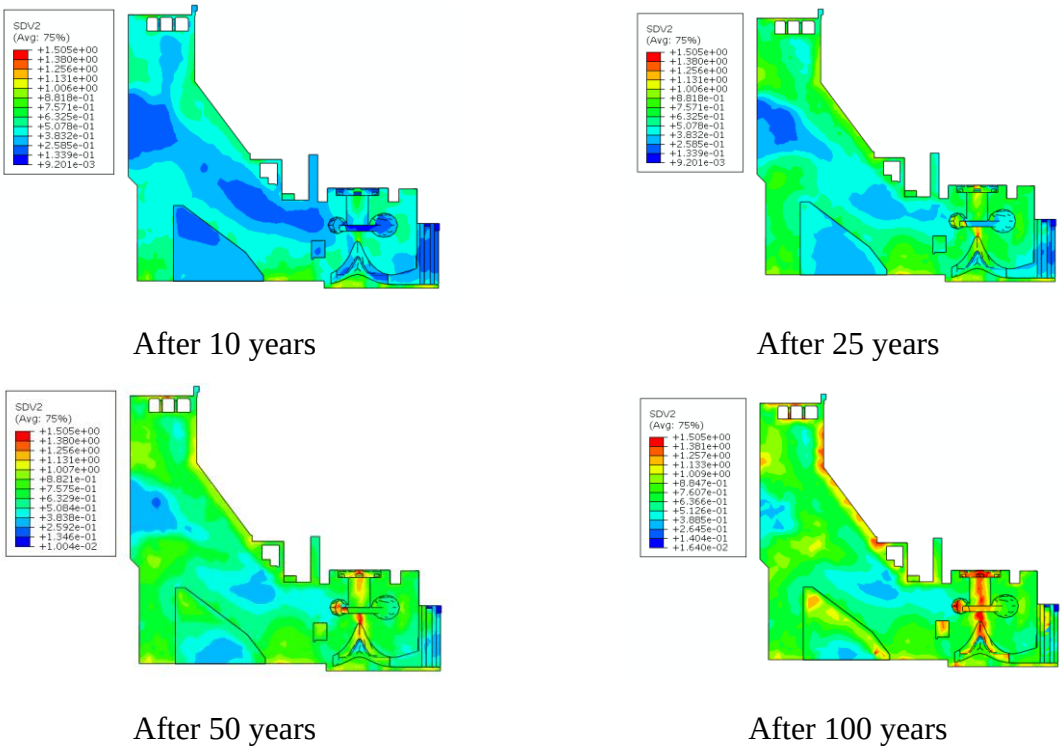

Fig 5-6-Damage distribution in section A at different stages of ASR

The provided results serve primarily as an illustration and demonstrate the ability of the employed methodology to model the ASR-induced damage propagation in large scale hydraulic structures. The main subroutines have been incorporated in available commercial software (i.e. Abaqus and COSMOS), so that they can be used for assessing the damage in other reinforced concrete structures, such as bridges and piers, due to the mechanical and chemical loading. The main

advantages of the volume averaging scheme over other numerical techniques (XFEM and SDA) for modeling damage growth in practical engineering problems, include the enhanced speed of simulations and the simplicity of implementation, both without compromising the accuracy of the solution.

5.3 References

1. Canadian Journal of Civil Engineering, Special issue on alkali-reactivity in Canada, 2000; **27**: 167-388.
2. Broekmans, M., Wigum, B.J, Proceedings of the 13th Intern. Conf. on Alkali-Aggregate Reaction in Concrete, 2008; Trondheim, Norway.
3. Pietruszczak, S. On the mechanical behaviour of concrete subjected to alkali – aggregate reaction, *Comp. & Struct.*, 1996; **58**: 1093–1097.
4. Capra, B., Bournazel, J. P. Modeling of induced mechanical effects of alkali-aggregate reactions, *Cem. Concr*, 1996; **28**: 251–260.
5. Ulm, F.J., Coussy, O., Kefei, L., Larive, C. Thermo-chemo-mechanics of ASR expansion in concrete structures, *J. Engng Mech., ASCE*, 2000; **126**: 233–242.
6. Steffens, A., Kefei, L., and Coussy, O. Aging approach to water effect on alkali-silica reaction degradation of structures, *J. Engng Mech., ASCE*, 2003; **129**: 50–59.
7. Multon, S., Toutlemonde, F. Effect of applied stresses on alkali-silica reaction-induced expansions, *Cem. Concr.Res.* 2006; **36**: 912–920.
8. Saouma, V., Perotti, L. Constitutive model for alkali-aggregate reaction, *ACI Mat. J.*, 2006; **103**: 194–202.
9. Grimal, E., Sellier, A., Le Pape, Y., Bourdarot, E. Creep, shrinkage and anisotropic damage in alkali-aggregate reaction swelling mechanism – Part I: A constitutive model, *ACI Mater. Journ.* 2008; **105**: 227-235.
10. Bažant, Z.P., Steffens, A. Mathematical model for kinetics of alkali-silica reaction in concrete, *Cem. Concr.* 2000; **30**: 419–428.
11. Bažant, Z.P., Zi, G., Meyer, Ch. Fracture mechanics of ASR in concretes with waste glass particles of different sizes, *J. Engng Mech., ASCE*, 2000; **126**: 226–232.

12. Sellier, A., Bourdartt, E., Multon, S., Cyr, M., Grimal, E. Combination of structural monitoring and laboratory tests for assessment of alkali-aggregate reaction swelling: Application to gate structure dam, *ACI Mat. J*., 2009; **106**: 281–290.

13. Gocevski, V. Monitoring, testing and remedial work at Beauharnois power plant, 2nd Intern. Conf. on Alkali-Aggregate Reactions in Hydroelectric Plants and Dams, USCOLD, 1995; Chattanooga, Tennessee.

14. Kladek, I., Pietruszczak, S. Gocevski, V. Modeling of mechanical effects of alkali-silica reaction in Beauharnois powerhouse, 6th Intern. Symposium on Numerical Models in Geomechanics - NUMOG VI, 1995; Davos, Switzerland, pp.639-644.

6 Conclusions

In this section the concluding remarks as well as suggestions for future work are presented. The main contributions of this study have been identified in the introduction to chapters 2-5. Based on a broad range of numerical examples, and the comparison of their results with the available experimental data, it was demonstrated that the enhanced embedded discontinuity scheme is a quite efficient tool in simulating the mechanical response in the presence of strong discontinuities within the domain. For tracing the crack path in a discrete way, the smoothening algorithm was implemented. This algorithm helps to maintain the stability and mesh-independency of volume averaging scheme and can be applied to a wide range of problems. In contrast to other numerical methodologies for modeling propagation of damage, i.e. the strong discontinuity approach and Extended Finite Element method, the proposed framework doesn't require any special enhancements such as additional degrees of freedom, modification of the shape functions and/or sub-triangulation for numerical integration. This not only simplifies the implementation in the context of finite element, but also increases the speed of simulations, which is of significant importance in analysis of large scale structures.

In the second chapter, the chemo-elastic formulation coupled with the volume averaging methodology has been presented. The effects of alkali-silica-reaction were examined by considering volumetric expansion as well as a progressive degradation of strength and deformation characteristics as a function of time. A return mapping algorithm has been developed which improved the stability of the solution and enabled modeling the time-dependent process with larger time steps as compared to explicit framework. An enhanced form of traction-separation law (based on total equivalent displacement) was employed for the fractured zone. The mixed mode crack propagation in a concrete panel was investigated, and the crack trajectory together with the corresponding load-displacement response were compared with the experimental results. In addition, the predictive abilities of the chemo-mechanical framework have been examined by simulating a reinforced concrete beam subjected to continuing ASR.

In Chapter 3, a chemo-plasticity framework was discussed as an extension of the formulation used in the Chapter 2. In this framework, the total stress rate was resolved into two parts, one related to the imposed instantaneous strain increment and the other one associated with the time-dependent chemical interaction process. An implicit integration scheme was again developed and employed in the numerical simulations. The behavior of intact material was modelled using a non-associated plasticity framework with deviatoric hardening and a cohesive law for the fractured zone was developed for both tensile and compressive regimes. In the tensile zone, the crack was assumed to form in the direction normal to the maximum principal stress, while in the compression regime the bifurcation analysis was employed to determine the onset of localized damage.

In terms of implementation of this framework, the main focus was on investigation of the size effect phenomenon. In the first example, a progressive damage in a three-point bending test was examined for a number of different sizes in relation to both a notched and un-notched beam. The results clearly showed the importance of incorporating the notion of a properly defined *characteristic length* in order to quantify the size effect. The second example involved the assessment of the size effect in a specimen subjected to axial compression. It was demonstrated that the ultimate load was not sensitive to the characteristic size of the structure. At the same time, however, the brittleness in the post-peak response was significantly affected by the structural dimensions.

The most significant contribution in this chapter was the investigation of size effect due to chemical reaction (ASR). To examine this, a concrete beam subjected to chemical reaction under two different loading conditions was considered. In the first case, a variable high intensity load (close to ultimate load for each specific geometry) was imposed and then maintained constant, while a progressive chemical interaction continued. In this case, the time to failure was strongly affected by the size of the beam, i.e. the failure took place first in the largest structure. In the second loading scenario, the reaction was activated at a constant load intensity (corresponding to a fixed value of normalized displacement), which was below the value of ultimate load for all sizes considered. In this case, the smaller specimens remained stable over the entire period of the continuing ASR. At the same time, for larger samples, a spontaneous loss of stability occurred.

Overall, the presented results clearly show that the size effect can be adequately simulated by employing the advocated approach. This is in contrast to the commonly used approximate analytical expressions which incorporate a number of empirical parameters that cannot be easily calibrated for new structures.

In Chapter 4, the embedded discontinuity technique was employed in the context of a mesoscale approach for modeling of reinforced concrete structures. In this case, the representative elementary volume incorporated concrete with three orthogonal families of reinforcement. Independent sets of static and kinematic constrains were imposed in order to relate the local stress/strain rates in each constituent to the corresponding macroscopic rate. Prior to onset of crack formation, a perfect bounding was assumed between reinforcement and concrete and the mixture theory was employed to define the overall response of the composite. Since the focus in this work was on the crack growth in tensile regime, the concrete was considered as elastic prior to onset of fracture, while the reinforcement was idealized as an elastic perfectly plastic Von-Misses material. After the formation of discontinuity, the considered referential volume was subdivided into a fractured zone and the intact material. A continuity of traction along the discontinuity was imposed using an implicit scheme and the Timoshenko beam theory was employed to assess the stiffness of the reinforcement within the fractured area.

The above framework was implemented to solve a number of boundary value problems. In the first example, the crack smoothening algorithm was employed to address a 3D problem involving a non-planar crack propagation in a notched concrete beam. The evolution of twisting of the crack surface was compared with other numerical methodologies, i.e. XFEM and adaptive re-meshing, and gave very similar results. In the follow up examples, the fracture propagation in reinforced concrete structures was investigated. The first analysis examined the crack growth in reinforced concrete beam for different volume fractions of reinforcement. For an under-reinforced structure, the yielding of steel commenced prior to failure of concrete, however by increasing the volume fraction of rebars, the failure process was initiated by the onset of macrocracking in concrete. For all cases, the load-displacement curves were compared with the relevant experimental data. The next set of simulations dealt with the response of reinforced beam under a four-point bending. The

failure mechanism involved formation of shear and flexural cracks and the results were compared with experiments for three different values of the shear span. It was clearly shown that the results are independent of the size of the selected composite zone as the latter affects directly the volume fraction of reinforcement.

The final chapter of this thesis discussed the implementation of the proposed framework in the analysis of a large scale structure. In particular, the long-term behavior of a reinforced concrete dam subjected to ongoing ASR was examined. The simulations demonstrated the advantage of this methodology over the alternative approaches, i.e. XFEM and SDA. The latter require significantly more computational effort and have never, in fact, been applied to the analysis of an actual large engineering structure.

6.1 Future Work

The current research can be enhanced in several aspects. Concerning the alkali-silica reaction, in the next step, a more rigorous formulation can be used for describing the kinetics of the process. As the expansion due to ASR can be affected by the stress field, it is likely that this will trigger an anisotropic response that could be explicitly incorporated into the volumetric term associated with swelling. In addition, the considerations of humidity and temperature, and their interaction with structure through the boundary conditions, could be described in a more accurate form.

Regarding the assessment of size effect resulting from ASR, it appears that the consideration of statistical aspects, which might be of significance, could also be examined. The latter are typically associated with the randomness of material properties, such as compressive/tensile strength, as well as that of maximum expansion and/or the rate of degradation.

The formulation of the embedded discontinuity approach employed here, was limited to the case when the considered referential volume was intercepted by a single discontinuity. This approach can be enhanced by considering existence of multiple cracks/faults within the averaging domain. Such a framework would be relevant to, for example, analysis of jointed rock masses.

Another aspect that could be further addressed in relation to this research is an adequate modeling of the debonding process that occurs between concrete and the reinforcement. This would entail additional experimental tests examining this phenomenon under different loading scenarios. In terms of formulation of the problem, the simplest approach appears to be that associated with imposing an evolution law on the characteristic length of the rebars within the fractured zone as a function of continuing deformation.

Finally, it is noted that the volume averaging technique can also be modified to capture weak discontinuities, which is relevant in the context of modeling of porous media that undergo a thermo-hydro-mechanical interaction. Such a modification would be relevant to the first two terms, i.e thermo-hydraulic interaction, while the crack growth in solid phase would still be described by the framework proposed in this research.